Department of Civil Engineering
Graduate School of Urban Innovation
Yokohama National University

Proposals to Improve XBeach Model and Statistical Analysis for Spatial Distributions of Undertow

「戻り流れの空間分布に関する**XBeach**モデルの改良提案と統計解析」

A dissertation
by
Kullachart BORRIBUNNANGKUN

Supervised by
Professor Takayuki SUZUKI

August 2022

Abstract

Current patterns in a nearshore zone are classified into alongshore and cross-shore currents. Undertow is a significant offshore-ward current that is induced by a shoreward water mass flux under wave breaking and Eulerian drift under non-wave-breaking conditions. It significantly plays a key role in the offshore sediment transport and also affects swimming safety. To increase the understanding of the undertow, field observations were conducted during two periods under different topography conditions on an alongshore uniform beach on the Hasaki coast in Japan. The first period spanned 21 days from May 13 to June 2 in 2016, and the second period spanned 13 days from May 9 to May 22, 2017. A horizontal acoustic Doppler current profiler was used to measure the cross-shore currents, that is, undertow, and the water levels in the surf zone. The observed data were statistically analyzed to investigate the characteristics of the spatial and wave-energetic distributions of the undertow exceedance probability. The results reveal that when the wave energy flux level was high, the undertow increased, as did its exceedance probability. By contrast, the exceedance probability of the undertow during a low wave energy level decreased with greater water depths, and its lowest value was in the trough region. Applying a Weibull distribution to the exceedance probability, the curves developed a statistical model of the undertow, and it was considered that the combination of normalized values of the wave energy flux, relative surf zone locations, and normalized water depths, which was defined as the efficiency of the undertow, was able to estimate two Weibull parameters: scale and shape. A comparison of the statistical model against the measurement demonstrates that the model accurately predicted the exceedance probability of an undertow with a small error.

Despite the statistical analysis of undertow in this research, the undertow simulations have been rarely discussed in nearshore morphodynamic modeling, especially, the effect of the changes in water depth on the undertow current has been overlooked. A two-dimensional XBeach model is one of numerical models that still faces difficulty in reproducing undertow, and this yields an error in the bathymetry profile update. Thus, the observed undertow data were more efficiently used to test with the undertow results from XBeach model. Since the XBeach model contains many adjustable coefficients, the observed undertow data were separated into high-and low-energy-wave conditions by using the average value of wave energy in the whole observation period as a criterion. The model coefficients relating to wave motion and surface roller were calibrated to obtain the best prediction of undertows.

Calibration of model coefficients yielded good results for waves, though low accuracy for the simulated undertow under both high- or low-wave energy conditions. Here, the individual contributions of Stokes drift and wave forcing (generated by radiation stress) term were respectively modified by including a water depth coefficient. This adjustment caused the undertow's water depth to be considered from under the wave trough level. For both high- and low-energy wave conditions, the temporal undertow comparisons show a small improvement in the whole period and the accuracy correlates with tidal elevation. When the comparisons of undertow spatial distribution were considered at the different water levels, the undertow results were significantly improved especially at low tide, with an increase in accuracy from bad to fair.

Yet, the underestimation of undertow remains not only under low-wave energy conditions, but also during the high-wave energy conditions, specially at the locations of wave breaking. To increase the undertow velocity, the modification of wave roller energy was conducted by including an equation to calculate roller coefficient based on wave height, wave number and water depth, yielding the decrease in roller energy dissipation. As a result, the strong undertow in the wave breaking zone was simulated, with a peak close to the peak of observed undertow. This scheme improved the undertow prediction from bad to good quality; however, no changes for modeling undertow under low waves.

Acknowledgments

First, I would like to express my sincere gratitude to my academic supervisor, Prof. Takayuki SUZUKI for giving me the great opportunity to be his selected student under Monbukagakusho scholarship. Throughout five years from my master's study until the doctoral program, I have been greatly encouraged and supported by him for both academic research and daily life. He is good supervisor with a good personality whom students always appreciate.

Besides my supervisor, I would gratefully acknowledge my co-supervisors: Prof. Yoshiyuki NAKAMURA, Assoc. Prof. Hiroto HIGA, and specially Dr. Martin MÄLL, for all insightful comments and encouragement, particularly during the weekly seminar of our laboratory. Their several comments and questions motivated me to widen this research from various perspectives. I am also grateful for the good comments and suggestions from the committee members: Prof. Hiroshi KATSUCHI, Prof. Kimitoshi HAYANO and Assoc. Prof. Chikako FUJIYAMA, including Prof. Daniel Cox (OSU). Furthermore, Assoc. Prof. Thamnoon Rasmeemasmuang (BUU) is an indispensable lecturer whom I highly thank for his recommendation to continue the higher education in YNU, and Ms. Akiko Nakao is also kindly acknowledged for her several supports to dealing with my documents.

This research was funded through JSPS grant-in-aid no. 26709034. As the research includes the field observations, I would like to thank all of the staff members at Hasaki Oceanographical Research Station (HORS), Japan, for kindly helping with the observations, including the graduate students, Mr. Kiichi TAJIMA and Mr. Rei MIYAZAKI, who conducted the field observations and shared the datasets. Also, I thank the Kashima Port and Airport Construction Office for their permission to use the offshore wave datasets.

Moreover, I extend our appreciation to the XBeach team, especially Dr. Robert McCall and their supports for providing XBeach course and releasing the model in the public domain.

My sincere thanks also go to the members of Estuarine and Coastal Engineering Laboratory, especially Mr. Salika Thilakarathne who are much appreciated for their assistance when I faced the difficult situations during this doctoral program. Unforgettably, I would like to extend my eternal appreciation to my parents, Ms. Sharmily Bhowmik, and other friends for their moral support and encouragement which served as my inspiration in completion of my degree.

Last but not the least, I would like to highly acknowledge the Ministry of education, culture, sports, science and technology for providing for the financial support, that is, Monbukagakusho (MEXT) scholarships from master's to doctoral degrees (October 2017 - September 2022).

Contents

Abstract ii

Acknowledgements iv

List of Figures xv

List of Tables xvii

Notation xviii

1 Introduction 1
- 1.1 Background 1
- 1.2 Objectives 5
- 1.3 Significance of the study 6
- 1.4 Overview of contribution 8

2 Review of Related Literature 9
- 2.1 Wave-generated nearshore current: undertow 10
- 2.2 Numerical models of undertow 11
  - 2.2.1 Wave transformation model 12
  - 2.2.2 Surface roller model 14
  - 2.2.3 Modeling mean undertow velocity 15
- 2.3 Exceedance probability 17
- 2.4 Weibull distribution 18

3 Methodology 19
- 3.1 Location of study site 20
- 3.2 Field observations 21
  - 3.2.1 The 2016 field observations (HC16) 22

3.2.2 The 2017 field observations (HC17) 22
3.2.3 Data acquisition and data filtering 23
3.2.4 Correlation between observed longshore current and wave direction 26
3.3 Analysis of undertow exceedance probability 27

4 Field Datasets **29**
4.1 Data description for the field observation in May 2016 (HC16) . . . 29
4.1.1 Bathymetry profile of HC16 29
4.1.2 Wave condition of HC16 30
4.1.3 Variability of cross-shore current in HC16 31
4.2 Data description of the field observation in May 2017 (HC17) 33
4.2.1 Bathymetry profile of HC17 33
4.2.2 Wave condition of HC17 33
4.2.3 Variability of cross-shore current in HC17 35

5 Statistical Analysis of Undertow **37**
5.1 Statistical distributions of undertow current data 37
5.1.1 Sorting the cross-shore component of wave energy flux 37
5.1.2 Wave-energetic and spatial distributions of undertow data . . 40
5.2 Exceedance probability analysis for undertow 43
5.2.1 Undertow exceedance probability of HC16 44
5.2.2 Undertow exceedance probability of HC17 47
5.3 Results of exceedance probability analysis 49
5.3.1 Effect of wave energy flux 49
5.3.2 Effect of cross-shore location and water depth 50
5.4 Modeling for undertow exceedance probability 52
5.5 Tidal range effect on undertow exceedance probability 59
5.6 Discussion Points 66
5.6.1 Applications of the statistical model in practices 67
5.6.2 Tidal range effect on undertow in different cases 73

6 XBeach (Kingsday Release) **77**
6.1 Introduction 78
6.2 Methodology 79
6.2.1 Model description 80
6.2.2 Undertow prediction 82

6.3 Results of undertow simulations 83
6.3.1 Model set-up and tuning parameters 83
6.3.2 Time shift 86
6.3.3 Theoretically improving the simulated undertow 92
6.4 Discussion 95

7 XBeach (X Release) 97

7.1 Updated functions in XBeach model 98
7.2 Undertow modeling in XBeachX 99
7.2.1 Model set-up 99
7.2.2 Tuning model coefficients 100
7.3 Modification of undertow prediction I: water depth 100
7.4 Undertow simulation under LWE conditions 102
7.4.1 Field datasets during LWE 102
7.4.2 Wave comparisons under LWE 104
7.4.3 Temporal undertow comparisons under LWE 105
7.4.4 Spatial distributions of undertow under LWE 106
7.5 Summary of undertow results under HWE conditions 109
7.6 Modification of undertow prediction II: wave roller 111
7.6.1 Effects of wave roller on undertow 112
7.6.2 Spatial distributions of undertow under HWE 113
7.6.3 Recheck of the spatial distributions of undertow under LWE . 117

8 Concluding Remarks 120

8.1 Summary of the study 120
8.2 Limitations and recommendations 122

Bibliography 133

Appendix 134

List of publications 142

List of Figures

1.1 Intensity of undertow current depends on the alternation between the effects of wave energy flux and water depth. Wave energy flux strengthens undertow currents during HWE conditions, while the undertow is dominated by the change in water level during LWE conditions. 3
1.2 Undertow plays a key role on cross-shore sediment processes in the nearshore region. The vertical distributions (referred from [67] [89]) present the uniform (weak) and parabolic (strong) structures of undertow currents at the nearshore-planar seabed and sandbar crest regions, respectively. 6

2.1 Nearshore currents (Woods Hole Oceanographic Institution, USA [77]). 9
2.2 Eulerian net flow velocity resulting form compensating a steady flow based on continuity consideration. 10
2.3 Vertical distribution of undertow occurred in the surf zone. 11
2.4 Assumed distribution of the time-average cross-shore current velocity. 15

3.1 Flow chart of research methodology for statistical analysis. 19
3.2 Location of the Hasaki Oceanographical Research Station (HORS) and bathymetric map of the study site (Japan Oceanographic Data Center). 20
3.3 A 427-m-long pier located at HORS, Japan. 21
3.4 Barred beach profile of the field observation in May, 2016 (HC16). . 22
3.5 Unbarred beach profile of the field observation in May, 2017 (HC17). 23
3.6 (a) An observation array complemented by three instruments: a wave gauge, a current meter and H-ADCP. (b) Emplacement of the observation array in HC16. 24

3.7 Example of data filtering of the (top) cross-shore current, (middle) wave height, and (bottom) water level during 00:40–05:00 AM on May 17, 2016. The black dots and open circles indicate raw and average data. The gray horizontal lines indicate the time of the averaging. The red rectangle represents the 20-min observed wave height at NOWPHAS. 25
3.8 (a) An observation array complemented by three instruments: a wave gauge, a current meter and H-ADCP. (b) Emplacement of the observation array in HC17. 25
3.9 Correlation between the observed longshore current and adjusted wave direction for (a) HC16 and (b) HC17. 26
3.10 Exceedance probability of observed and Weibull distributions applicable to normalized undertow at the location $x = 126$ m of HC16. . 28

4.1 Beach profile of HC16 with average and standard deviation. 30
4.2 Time-series data indicating wave condition in HC16: (a) wave height, (b) wave period, and (c) wave direction. 31
4.3 The observed time-series datasets of HC16: (a) cross-shore currents, (b) wave energy flux (blue) with a cross-shore component (black), and (c) the water level. 32
4.4 Beach profile of HC17 with average and standard deviation. 34
4.5 Time-series data indicating wave condition in HC17: (a) wave height, (b) wave period, and (c) wave direction. 34
4.6 The observed time-series datasets of HC17: (a) cross-shore currents, (b) wave energy flux (blue) with a cross-shore component (black), and (c) the water level. 35

5.1 Overview of seabed profiles of HC16 and HC17. 38
5.2 Histograms of the cross-shore component of the wave energy flux and range of each wave energy level from the highest A to the lowest D for (a) HC16 and (b) HC17. 38
5.3 Wave-energetic and spatial distributions of histograms of undertow datasets for HC16. 42
5.4 Wave-energetic and spatial distributions of histograms of undertow datasets for HC17. 43

5.5 Exceedance probability of observed and Weibull distributions applicable to normalized undertow for HC16: (a) location of $x = 116$ m for each wave energy level and (b) wave energy level of C for each considered location. 45

5.6 Wave-energetic distribution of the exceedance probability of observed and Weibull distributions applicable to normalized undertow for locations of: (a) $x = 96$ m, (b) $x = 116$ m, (c) $x = 126$ m, (d) $x = 161$ m and (e) $x = 191$ m in HC16. 45

5.7 Spatial distribution of the exceedance probability of observed and Weibull distributions applicable to normalized undertow for energy levels of: (a) E_{fu} = A, (b) E_{fu} = B, (c) E_{fu} = C, and (d) E_{fu} = D in HC16. 46

5.8 Energetic distributions of the observed undertow P_E, and Weibull distributions applicable to normalized undertow for HC17 at the locations of: (a) $x = 116$ m, (b) $x = 126$ m, (c) $x = 161$ m, (d) $x = 191$ m and (e) $x = 221$ m. 48

5.9 Spatial distribution of the observed undertow P_E, and Weibull distributions applicable to normalized undertow for HC17 at the energy levels of: (a) E_{fu} = A, (b) E_{fu} = B, (c) E_{fu} = C, and (d) E_{fu} = D. 48

5.10 Wave-energetic distributions of the undertow P_E of observed and Weibull distributions applicable to normalized undertow at the location of $x = 126$ m for (a) HC16 and (b) HC17. The black rectangle, gray circle, blue triangle, and gray rectangle differentiate the undertow datasets at wave energy levels of A, B, C, and D, respectively. The solid and open symbols represent the observed undertow P_E for HC16 and HC17, respectively. The vertical dashed, rigid, and dotted lines refer to the criteria of normalized undertow at $u_E/\overline{u}$ = 0.5, 1.0, and 3.0, respectively. 50

5.11 Spatial distributions of the undertow P_E of observed and Weibull distributions applicable to normalized undertow at the energy level of C for (a) HC16 and (b) HC17. The solid and open symbols represent the observed undertow P_E for HC16 and HC17, respectively. The blue triangle indicates the undertow datasets at wave energy levels of C at the location of $x = 126$ m (the same as in Figs. 5.3 and 5.4). The red upside-down triangle represents the undertow P_E, which increases at $x = 191$ m (bar region). The rigid line refers to the criterion of the normalized undertow at $u_E/\overline{u} = 1.0$. 51

5.12 Correlation between n_e and two Weibull parameters (scale a and shape b). The scale parameter a obtained at wave energy levels of A, B, C, and D were differentiated by the black rectangle, gray circle, blue triangle, and gray rectangle, respectively. The shape parameter b was indicated by the rhombus. The HC16 and HC17 datasets were distinguished by using the solid and open symbols, respectively. The rigid and dashed lines represent the fit functions for parameters a and b, respectively. 53

5.13 Comparison of wave-energetic distribution between the observed and modeled undertow P_E at location $x = 96$ m. 54

5.14 Spatial distributions of undertow P_E under the criterion of $u_E/\overline{u} = 0.10$ for (a) HC16 and (b) HC17. Panels (i)–(iv) show the results from energy levels A–D, respectively. The observed, Weibull, and best-fit model P_E were represented by a black rectangle, gray circle, and half-red filled triangle, respectively. Panel (v) illustrates the average seabed profile. 56

5.15 Best-fit modeled versus observed P_E (half-filled red triangle), and modeled Weibull versus observed P_E (gray circle) considering $u_E/\overline{u}$ = 1.0 for HC16 and HC17. 58

5.16 Observed exceedance probability applicable to normalized undertow distinguished by water level (field observation in May, 2016). 60

5.17 Spatial distributions of undertow exceedance probability on $u_E/\overline{u}$ for full, high-tide, and low-tide data of each wave energy flux level. (field observation in May, 2016). 61

5.18 Observed exceedance probability applicable to normalized undertow distinguished by water level (field observation in May, 2017). 63

5.19 Spatial distributions of undertow exceedance probability on $u_E/\overline{u} =$ 1.0 and 1.5 for full, high-tide, and low-tide data of each wave energy flux level. (field observation in May, 2017). 65
5.20 Filip Hjulström diagram [51] 68
5.21 Spatial distributions of undertow exceedance probability on $u_E/\overline{u} =$ 0.67, 1.0 and 2.0 for full, high-tide, and low-tide data of each wave energy flux level (field observation in May, 2016). 70
5.22 Spatial distributions of undertow exceedance probability on $u_E/\overline{u} =$ 0.52, 1.0 and 2.0 for full, high-tide, and low-tide data of each wave energy flux level (field observation in May, 2017). 72
5.23 Spatial distributions of undertow exceedance probability on $u_E/\overline{u} \geq 1$ for full, high-tide, and low-tide data of each wave energy flux level (field observation in May, 2016). 74
5.24 Spatial distributions of undertow exceedance probability on $u_E/\overline{u} \geq 1$ for full, high-tide, and low-tide data of each wave energy flux level (field observation in May, 2016). 75

6.1 Chart of methodology for modeling undertow using XBeach. 79
6.2 Chart of numerical processes for simulating undertow in XBeach model. 80
6.3 (a) skill and (b) slope values of tuning *hmin* for high-energy wave condition. 84
6.4 (a) skill and (b) slope values of tuning *Beta* for both of high- and low-energy wave conditions. 85
6.5 Time-series of (1) undertow velocity, (2) Stokes drift and (3) water depth at the location of $x = 96$ m: (a) rfb = 0 (b) rfb = 1. 86
6.6 Time-series of (1) undertow velocity, (2) Stokes drift and (3) water depth at the location of $x = 96$ m for the low-energy wave case (May 24 - June 2, 2016). 87
6.7 Changes of comparison of the observed and modeled undertow for the locations of $x = 96$, 116 and 161 m due to time-shif from 0 to 3 hours. 88
6.8 Time-series of modeled undertow after time shift for 3 hours in the case of low-energy wave. 89
6.9 (a) skill and (b) slope values of the comparisons relating to time-shift for low-energy wave conditions. 89
6.10 (a) RMAE and (b) RMSE of the comparisons relating to time shift for low-energy wave conditions. 90
6.11 Effect of water level on undertow velocity. 91

6.12 Time-series of (1) undertow velocity, (2) Stokes drift (3) water depth and (4) wave energy flux at the location of $x = 96$ m for the entire period. 91
6.13 Variation of RMAE due to the coefficient λ from 0.3 to 2 for the locations of $x = 96$, 116 and 126 m. 93
6.14 Comparison of the peaks between the observed and modeled undertow at the location of $x = 96$ m. 94
6.15 Spatial distributions of (a) RMAE and (b) RMSE at the locations of $x = 96$, 116 and 126 m for the modeled undertow in the different cases of initial (black), after a time shift of 3 hours (blue) and after multiplying with $\lambda = 0.60$ (red). 94

7.1 Schematic of Lagrangian velocity and Stokes drift associated with the generation of undertow. 101
7.2 Seabed profile change during the LWE conditions. 102
7.3 Observed time-series data during LWE of HC16: (a) significant wave height and wave period, (b) wave direction, (c) water level, and (d) cross-shore currents. 103
7.4 Time-series data of the observed (black), XBeach DF (gray), MF-1 (blue), and MF-2 (red) modeled wave heights at $x =$ (a) 303, (b) 145, and (c) 40 m. 104
7.5 Time-series data of undertow during May 28–31, 2016, at five locations of $x =$ (a) 191, (b) 161, (c) 126, (d) 116, and (e) 96 m, and (f) water level for the observed (black), XBeach DF (gray), MF-1 (blue), and MF-2 (red). 105
7.6 Spatial distributions of undertow on May 29 at (a) high tide, (b) close to MWL, and (c) low tide of 0.85, 0.50, and 0.16 m, D.L., respectively. 107
7.7 Observed vs. DF, MF-1 and MF-2 modeled undertow current velocities and regression lines response under LWE (a) with and (b) without shore-ward velocity value. 107
7.8 Time averaged values on three tidal cycle (Fig. 7.5, (1)-(3)) during May 28–30, 2016: (a) RMAE of XBeach DF (gray), MF-1 (blue), and MF-2 (red) simulated undertow results, and (b) observed water level. 108
7.9 Spatial RMAE values of undertow simulation at low tide on each day during May 28-30. 109
7.10 Observed vs. modeled XBeach DF (black), MF-1 (blue), and MF-2 (red) undertow velocities response HWE for data group A. 110

7.11 Seabed profile change during the HWE conditions and the wave-breaking zone (pink mark). 111
7.12 The shoreward flux is decreased due to wave roller and the rest flux induces undertow beneath the wave trough. 112
7.13 Observed time-series data during HWE from May 13 to 17 of HC16: (a) cross-shore currents, (b) wave energy flux, and (c) water level. . 114
7.14 Spatial distributions of undertow of group A data on May 16 at 6^{th} hour: (a) 01:40 AM, (b) 02:00 AM and (c) 02:20 AM, and at 7^{th} hour: (d) 10:20 AM and (e) 11:20 AM. 116
7.15 Observed vs. modeled XBeach DF, MF-1, MF-2, and MF-3 undertow velocities response HWE for data group A. 118
7.16 Spatial RMAE values of undertow simulation for data group A under HWE. 118
7.17 Spatial distributions of undertow on May 13 at (a) 12:40 PM and (b) 1:40 PM. 119

8.1 Correlation between n_e and scale and shape parameters, when the logarithm function was used for a. 138
8.2 Spatial distributions of undertow exceedance probability on u_E = -0.10 m/s ($u_E/\overline{u} = 1.0$) for the observation in 2016, when the logarithm function was used for a. 139
8.3 Correlation between n_e and scale and shape parameters, when the allometric function was used for a. 139
8.4 Spatial distributions of undertow exceedance probability on u_E = -0.10 m/s ($u_E/\overline{u} = 1.0$) for the observation in 2016, when the allometric function was used for a. 140

List of Tables

3.1 Description of the field observations. 21

5.1 Average wave conditions under each wave energy level for HC16. . . 39

5.2 Average wave conditions under each wave energy level for HC17. . . 39

5.3 Number of undertow data and its percentage relative to the total number in each wave energy level for and the six locations considered for HC16. 40

5.4 Number of undertow data and its percentage relative to the total number in each wave energy level for and the six locations considered for HC17. 41

5.5 Percentage of undertow probability exceeding u_E = -0.10 m/s ($u_E/\overline{u}$ = 1.0) for HC16. 57

5.6 Percentage of undertow probability exceeding u_E = -0.13 m/s ($u_E/\overline{u}$ = 1.0) for HC17. 58

5.7 Number of 2016 undertow datasets by separating into full-tide, high tide and low-tide durations. 60

5.8 Percentage of the measured exceedance probability at u_E = -0.10 m/s ($u_E/\overline{u}$ = 1.0) considering tide durations for the observation in 2016. 62

5.9 Number of 2017 undertow datasets by separating into full-tide, high tide and low-tide durations. 63

5.10 Percentage of the measured exceedance probability at u_E = 0.13 m/s and 0.20 m/s ($u_E/\overline{u}$ = 1.0 and 1.5) considering tide durations for the observation in 2017. 66

5.11 Summary of the velocity and normalized values of undertow in each case. 69

5.12 Percentage of undertow probability exceeding the differently extreme currents of u_E = -0.067, -0.10 and -0.20 m/s ($u_E/\overline{u}$ = 0.67, 1.0 and 2.0) for the observation in 2016. 71
5.13 Percentage of undertow probability exceeding the differently extreme currents of u_E = -0.067, -0.13 and -0.20 m/s ($u_E/\overline{u}$ = 0.52, 1.0 and 2.0) for the observation in 2017. 73

6.1 Parameter settings. 84
6.2 Summary of time difference of the peak velocities between the observed and modeled undertow in low-energy wave case. 87
6.3 Summary of RMAE and RMSE for the cases of modeled undertow after time shift and using $\lambda = 0.60$. 94
6.4 Percentage decrease in RMAE for the cases of modeled undertow after time shift and using $\lambda = 0.60$. 95
6.5 Percentage decrease in RMSE for the cases of modeled undertow after time shift and using $\lambda = 0.60$. 95
6.6 Average of water depth and wave height for the considered locations of x = 96, 116 and 126 m. 96

7.1 Updating of XBeach model. 98
7.2 Default settings for the XBeach Kingsday and X release versions. . . 99
7.3 Summary of undertow comparisons response under HWE conditions for MF-2 simulation. 110

8.1 Summary of the improvements of undertow prediction in XBeach model. 122
8.2 Average, standard deviation, maximum and minimum of the undertow velocity at each considered location for both 2016 and 2017 datasets. 134
8.3 Efficiency of undertow n_e for 2016 datasets. 135
8.4 Efficiency of undertow n_e for 2017 datasets. 135
8.5 Values of Weibull parameters a, b and n_e for 2016 datasets. 136
8.6 Values of Weibull parameters a, b and n_e for 2016 datasets after generalizing. 136
8.7 Values of Weibull parameters a, b and n_e for 2017 datasets. 137
8.8 Values of Weibull parameters a, b and n_e for 2017 datasets after generalizing. 137
8.9 Values of RMAE and RMSE owing to time shift. 141

Notation

A	orbital amplitude of fluid just above the boundary layer,
A_r	surface roller area,
a	scale parameter (Weibull distribution),
B	beach slope,
b	shape parameter (Weibull distribution),
C	wave celerity,
C_A	surface roller coefficient,
C_B	wave transform coefficient,
C_{br}	wave transform coefficient,
C_G	group velocity,
C_o	dissipation coefficient,
C_r	roller speed ($\approx$ C),
D_b	dissipation due to wave breaking,
D_r	dissipation due to surface roller,
h	total water depth,
h_B	water depth at the offshore sandbar crest,
h_b	water depth at wave breaking point,
h_T	water depth under wave trough level,
E	water energy flux (XBeach),
E_f	water energy flux,

F	wave-induced stress,
f	water level coefficient (Eq. 2.30),
f	Coriolis coefficient (XBeach),
g	gravitational acceleration,
H	wave height,
H_b	wave height at wave breaking point,
H_o	offshore wave height,
H_{rms}	root mean square of wave height,
H_s	significant wave height,
HWL	highest water level,
K	decay coefficient,
k	wave number, $2\pi/L$,
L_o	offshore wave length,
LWL	Lowest water level,
M	period-averaged mass flux,
MWL	mean water level,
m	constant,
N_0	number of undertow datasets,
n	C_G/C,
n_e	efficiency of undertow,
P	probability of undertow,
P_E	exceedance probability of undertow,
Q_b	fraction of breaking wave (XBeach),
Q_{E-net}	Eulerian net flow,
Q_r	Volume flux due to surface roller,
Q_w	Volume flux due to wave motion,
R	radiation stress due to surface roller,
r	index of skewness or non-linearity,
S	angular-frequency spectrum density (Eq. 2.7),
S	radiation stress due to wave breaking (Eq. 2.11-2.13),
T	wave period,
T_o	offshore wave period,
T_rep	representative of wave period,
T_s	significant wave period,
t	time,

U	wind speed,
U_r	Ursell number,
u	cross-shore current velocity,
u_E	undertow current velocity (Eulerian),
u_L	generalized Lagrangian velocity in x-axis (XBeach),
u_{rms}	root mean square of undertow velocity,
u_S	Stokes drift,
$\overline{u}$	average of undertow velocity in the whole observation period,
v	alongshore current velocity,
v_L	generalized Lagrangian velocity in y-axis (XBeach),
W_L	water level,
W_{L-rms}	root mean square of water level,
W_SD	standard deviation of water level,
w	settling velocity,
X_B	cross-shore distance measured from shoreline to a bar crest),
x	horizontal coordinate in the wave direction (Eq. 2.7),
x_L	cross-shore distance measured from shoreline to a considered location,
y	horizontal coordinate perpendicular to the x-direction,
z	considering depth measured from the seabed,
α	i-th rank of $u_E/\overline{u}$ from larger to smaller value,
α	dissipation coefficient (XBeach),
β	$u_E/\overline{u}$,
β_s	slope of the breaking wave front (XBeach),
γ	breaker index (XBeach),
γ_2	breaker index (XBeach),
δ	roller dissipation coefficient,
Γ	coefficient for stable wave height,
κ	free parameter,
λ	water depth coefficient,
ζ	water surface elevation,
ζ_{rms}	root mean square of water surface elevation,
η_up	wave set-up,
θ	angle counter clockwise from x-axis,
θ_s	significant wave direction,
θ_o	offshore wave direction,

ν	kinetic viscosity,
ρ	sea water density,
ρ'	sediment density,
τ_b	bed shear stress (XBeach),
τ_r	roller shear stress (XBeach),
τ_s	wind shear stress (XBeach),
ϕ	wave form parameter,
φ	fitting parameter,
ω	radian frequency, $2\pi/T$,
$\langle ... \rangle$	averaging procedure.

Chapter 1

Introduction

1.1 Background

In the surf zone, the pattern of wave-induced currents is classified into alongshore and cross-shore currents. Undertow and rip currents are seaward mean flows considered as the two main drivers of sediment transport in the coastal engineering field, which dominate both suspended and bedload transport rates and play a key role behind sandbar formation and beach erosion [16]. Both current patterns are fundamentally generated by an imbalance of the mass transport caused by the wave setup and radiation stress after wave breaking [2][72][97][98]; however, rip currents are also dominated by the longshore radiation stress gradients owing to the laterally irregular sandbar formation [110].

Since the severity of rip currents makes them dangerous to beach visitors, causing thousands of drowning deaths on beaches worldwide, such currents have received significant attention over the last three decades [14][97]. However, rip currents are narrow flows occurring in limited areas under high- to moderate-energy wave conditions [2], whereas undertows are more easily generated even under low-energy waves [11], and the cumulative effects of undertow can finally lead to bathymetry change over a wide area [36][80][83][94]. Furthermore, the existing science dogma regarding the common conception of undertow holds that undertow is underneath the return flow and is able to push people seaward faster than they could swim toward land [19]. Hence, to properly manage coastal areas and institute public hazard precautions to enhance swimming safety [13][48][108], undertow prediction is needed.

Undertow was first discovered as a return flow from the wave breaking point [9]. A qualitative explanation of the undertow existing in the circulation of nearshore currents was later given by Dyhr-Nielson and Sorensen [50]. However, the observation of the current velocity requires high-tech instruments, sensitive handling, and extensive costs, many existing investigations have been carried out based on laboratory datasets, and this limits the performance of the undertow models.

According to the well-known model for estimating mean undertow proposed by Svendsen and Hansen [98], undertow is governed by three dominant parameters: mass fluxes from wave breaking and a surface roller, and the water depth under the wave trough level. Each of these individual contributions has been theoretically improved for better estimating undertow velocity. For instance, the calculation of the surface roller was modified based on an elimination of the energy dissipation during a wave mass flux transfer [61][68]. In the surface roller calculation, when the area of surface roller decreased in comparison to Okayasu's formulation [44], as a result, the undertow velocity increased in the nearshore region, which gave a better agreement with the laboratory data.

Although undertow models have been developed by considering different aspects, different assumptions exist for each model. To elucidate which model was optimal for undertow prediction, Rattanapitikon and Shibayama (2000) [76] conducted verifications for those individually proposed undertow models against both small- and large-scale experiments. The findings revealed that Rattanapitikon's proposed undertow model that derived from the ratio of shear stress to eddy viscosity coefficient achieved the highest accuracy. However, this undertow model might be inappropriate in practice, as the error increases as the scale of the experiment is enlarged and reaches approximately 20% and 40% for small- and large-scale experiments, respectively. For instance, an occurrence of a strong undertow at the sandbar crest region was still underestimated against the large-scale SUPERTANK laboratory at Oregon State University, USA [40], and the field observations at the central research institute of electric power industry [37].

Not only the contributions of wave transformation and surface roller evolution, but the low accuracy of the undertow prediction can be caused by an inappropriate calculation of the water depth under the wave trough level, which is governed by the wave shape, and changes in water depth. The water depth effect on the undertow was demonstrated through some experiments, in which the undertow spatial distribution reveals a stronger undertow velocity in a bar region and a weaker undertow velocity in a trough region [65][66]. Especially, under low-energy-wave conditions, the undertow is sensitive to changes in water depth owing to tidal elevation and it was strengthened in low tide durations (Fig. 1.1) [12]. For this reason, the calculation of the water depth under the wave trough needs to be appropriately considered.

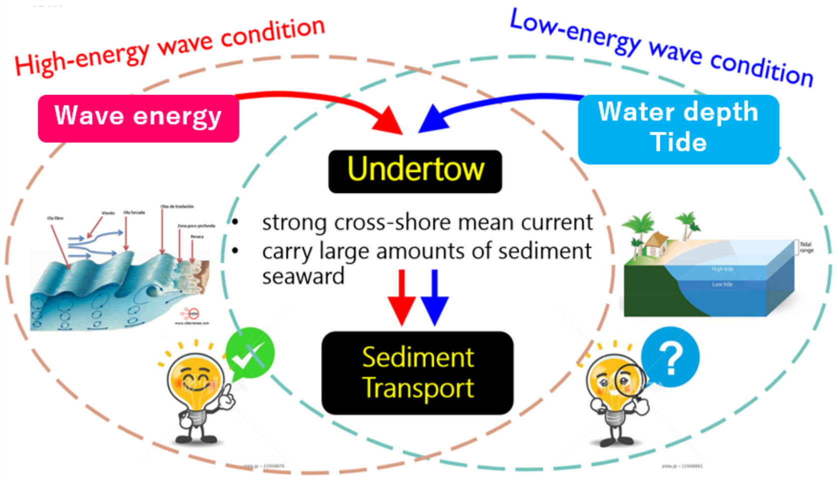

Figure 1.1: Intensity of undertow current depends on the alternation between the effects of wave energy flux and water depth. Wave energy flux strengthens undertow currents during HWE conditions, while the undertow is dominated by the change in water level during LWE conditions.

In the previous study, the wave trough level could be estimated by half of the root-mean-square value of the individual wave height. This might be accurate only for symmetric offshore waves and is insufficient for nearshore asymmetric waves [24][99]. To modify the calculation of water depth under wave trough level for estimating undertow, several significant investigations related to wave asymmetry have been conducted. For example, Drake and Calantoni (2001) [21] distinguished the effects of wave skewness and asymmetry by applying the Stokes higher-order theory. The quantities of local waves were incorporated into the prediction of the stream flow velocity near the bed by Elfrink, Hanes, and Ruessink (2006) [23]. Description of individual wave shapes characteristics was expensively clarified by Abreu et al. (2010) [3], including an improved analytic formulation of the free-stream velocity. In addition, Ruessink, Ramaekers, and van Rijn (2012) [85] modified Abreu's formulation by applying the Ursell number for random waves. Moreover, the undertow model was then improved by Nam et al. [63] for random wave conditions and tested against large-scale laboratory data conducted by Roelvink and Reiners [84]. The undertow prediction resulted in a good agreement with the measurements but the undertow was overestimated at a great water depth.

Although those investigations improved the undertow predictions, only datasets at some specific periods were selected for analysis, and much effort has been taken for increasing the performance of undertow modeling to obtain the best results. As a results, undertow characteristics changing throughout different wave conditions in the whole observation period have been less discussed. For that reason, this study aims to increase the understanding of undertow characteristics by focusing on its statistical distribution.

In this study, what undertow observations were conducted at the Hasaki coast, Japan, during barred and planar beach states. The variations of undertow behavior from high- to low-energy wave conditions were investigated using the statistical exceedance probability (hereafter P_E) scheme. Furthermore, the alternation between the effects of wave energy flux and water depth on the undertow P_E was elucidated for each wave level. The Weibull distribution was then applied to the observed undertows P_E, and this led to the development of a new undertow model. The proposed model was developed by generalizing two Weibull parameters using a combination of three main factors that intensify the undertow velocity, that is, the wave energy flux, seaward location, and water depth. This type of model can be used to assess the critical undertow velocity at different levels of wave energy, which is useful for planning beach nourishment and designing beach-accessing safety zone.

Since the observed undertow data were difficult to be measured at the farther offshore locations during the high-wave-energy (hereafter HWE) conditions, the performance of our statistical undertow model seems limited at the low-wave-energy (hereafter LWE) conditions. To increase the performance of this model in further works, a numerical modeling is the most possible method to retrieve the undertow data.

For numerical simulations, a quasi-3D undertow model [1] and an applied for the nearshore region of the fully 3D Princeton Ocean Model (POM) were developed [66]. The comparison of these two models against laboratory data indicated that both models can well predict the undertow distribution on breaking region; however, at the offshore region, quasi-3D undertow cannot well predict while POM can reproduce with a small underestimation [30].

Recently, XBeach model is wildly used in predicting storm impacts on natural coasts, yet in regard to morphodynamic predictions, the undertow simulations have been rarely discussed and verified by only experimental data. For examples, Roelvink et al. [80] examined XBeach model against laboratory and prototype scale experiments of breaching of the Zwin sand dike, as presented by Visser [106]. The comparisons between the measured and simulated flow velocities of the breach width in time were conducted. The result reveals that the simulated flow velocity was stronger than the measured flow. In surf zones, Jamal et al. [35] figured out that the onshore- and offshore-ward velocity profile envelopes expressed by using the Lagrangian formulation in XBeach were lower than that of the threshold velocity obtained from the Eulerian formulation for coarse sediment. Especially, this underestimation of undertow causes a smaller change of seabed profile than it should be.

Therefore, this study aims to improve the XBeach's undertow prediction. The capability of the model to reproduce undertow current was evaluated using the same field observation datasets at the Hasaki coast. Since the undertow datasets were measured under the different HWE and LWE conditions, which XBeach model cannot adjust the most skillful coefficients for each period by itself, the undertow simulation was separated into two durations. The model coefficients were calibrated to obtain the best prediction of undertow response under HWE and LWE conditions. However, the undertow simulation needs a modification for increasing performance. A new coefficient of water depth is suggested, and the modification of the wave-roller dissipation coefficient proposed by Rafati et al. [75] is also conducted. Both the temporal and spatial undertow results were analysed and discussed.

1.2 Objectives

A number of undertow models exist in the coastal engineering field, but those are accompanied by some assumption due to the model development based on laboratory experimental data. When these models are applied in practice, a low accuracy of undertow result against the field observation is obtained, which can cause an error to enlarge for the morphological total evolution. The undertow models have been improved from time to time and tested with the larger scale experiments. However, the field undertow observation is difficult to conduct, and the improvements of undertow model has, thus, been mostly limited to the out-of-date datasets from laboratory experiments. This research is one of essential investigations where the field observation was conducted to increase the understanding of undertow mechanism. Here, the undertow characteristics are demonstrated through statistical analysis.

Moreover, the field undertow datasets were used to assess the capability of undertow prediction in the XBeach model, and the most skillful coefficients were calibrated to obtain the best value for each condition of LWE and HWE. Since the simulated results reveal an inaccuracy against the observations, the XBeach-source code was modified to increase the accuracy of undertow prediction. The objectives of this research are listed as follows:

(1) To investigate the characteristics of undertow probabilistic distribution on the different seabed profiles.

(2) To develop a statistical model of undertow.

(3) To assess the performance of XBeach model to reproduce the undertow current velocity.

(4) To improve the undertow prediction in XBeach model.

1.3 Significance of the study

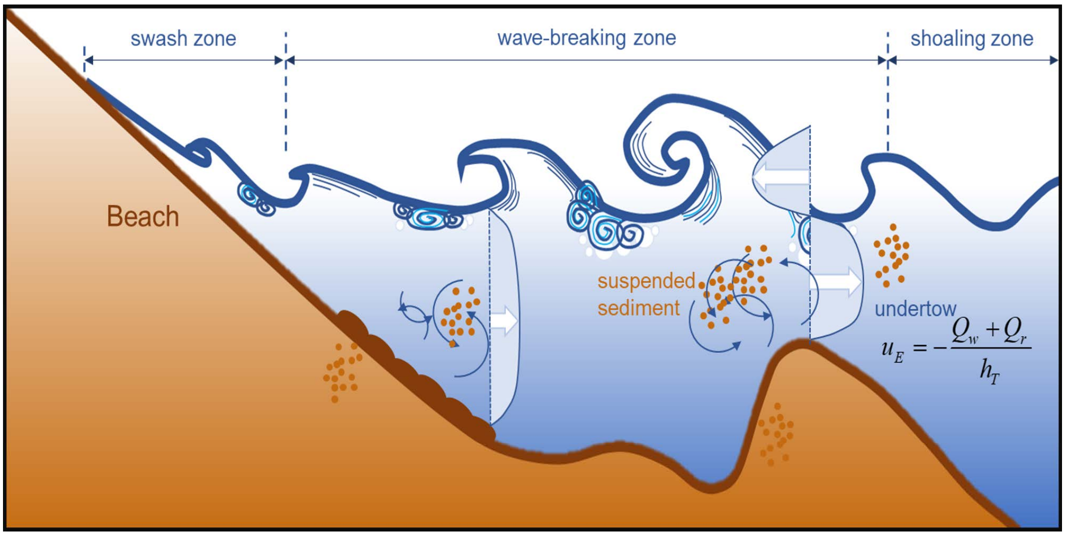

Figure 1.2: Undertow plays a key role on cross-shore sediment processes in the nearshore region. The vertical distributions (referred from [67] [89]) present the uniform (weak) and parabolic (strong) structures of undertow currents at the nearshore-planar seabed and sandbar crest regions, respectively.

In coastal zones, natural environmental changes and human activities cause the coastal dynamic action to lose balance in the coastal process. During waves are attacking the beaches, sediment is being suspended, and the sediment transport rate is expressed by the product of material concentrations and instantaneous velocity: longshore and cross-shore currents (undertow).

Figure 1.2 presents cross-shore sediment processes in the nearshore region. When waves propagate parallel to the shore with a small wave angle, the undertow induced by the onshore mass flux can carry large amount of sediment seaward. Therefore, the erosion process is mainly governed by the transport capacity of the undertow. Since the cumulative effect of undertow results in sandbar immigration, and the undertow characteristics are also varied by the seabed changes, the interaction between undertow and sandbar behavior is necessary to be investigated for developing a predictive capacity for nearshore flows and sediment transport in any mophodynamic models.

Undertow is not only one of important mechanisms in coastal zones behind beach formation and beach erosion, but it is also dangerous to swimmers and coastal structures. In order to suitably design an extreme undertow to safe swimming and organize beaches, the management of coastal lands and ecosystems, and the precautions of swimming need to be highly concerned the effects of undertow.

First, in order to obtain a statistical model of undertow, the author analyzed the observed undertow by using P_E method. The undertow probabilistic distribution was well-fitted by the Weibull distribution for developing the statistical model. The model contains an efficiency of undertow combining the normalized wave energy flux, relative surf zone location, and normalized water depth. Since these three hydraulic parameters are generally observed in the field, the intensity of undertow current could be predicted as a form of P_E score. This probabilistic approach can be used for planning beach management and shoreface nourishment, i.e., sand filling to prevent beach erosion, and designing beach-accessing safety zone. Some examples of utilizing the proposed model will properly be explained in Section 5.6.

Second, the improvement of undertow prediction in XBeach model will be discussed. XBeach model is generally used to simulate the impact of storm events for the nearshore and coast [55], and can well predict the morphodynamics of dissipative sandy beach [69, 91]. However, our field observations shows that undertow was periodically strengthened by tides during LWE conditions, where XBeach model reproduces the underestimated undertow current velocity. To gain a better result of undertow prediction, the author proposed a coefficient of water depth for the modification of XBeach-source code. Continuously, the equation of wave-roller coefficient proposed by Rafati [75] is tested. Once the XBeach model can well predict undertow velocity, the higher accuracy of seabed updating is expected, and the modeled undertow could be efficiently used to modify the statistical model of undertow. The explanation regarding this numerical model will extensively given from Chapter 6.

1.4 Overview of contribution

This research focuses on two main parts as given below, and the detailed contributions will be given at the beginning of each chapter.

(i) In Chapter 5, the investigation of the characteristics of undertow distribution by using P_E is given. The wave energy flux, cross-shore location and water depth are three main parameters that affects the undertow distribution, and the combination of them is defined as the efficiency of undertow (n_e). The statistical model is developed from the correlation between the n_e and Weibull parameters. The comparison between the observed and modeled P_E of undertow is demonstrated to ensure the capability of the model for predicting the undertow P_E. Moreover, in Section 5.5, the spatial distribution of undertow P_E is separated into high-tide and low-tide durations to elucidate the effect of tidal range on undertow.

(ii) From Chapter 6, the verification of undertow prediction in XBeach model for both versions Kingsday and X is provided. The comparisons between the modeled undertow velocity and the observed data are conducted to evaluate the performance of XBeach model. Because of low-accuracy prediction for undertow current, a coefficient of water depth and wave-roller equation are suggested for improving XBeach model. The modification of XBeach-source code is operated on Ubuntu platform. The verification of modeled undertow after modifications against the observed data is discussed using temporal and spatial undertow current velocities.

Chapter 2

Review of Related Literature

In this research, the objectives of conducting field observations are three-fold. First, to gain a better understanding of the characteristics of spatial distributions of undertow velocity observed under the differences of wave conditions. The physical mechanisms of the wave-induced current are elucidated in Section 2.1, and the existing theoretical and numerical models related to undertow calculation are included in Section 2.2. Second, to develop a statistical model of undertow exceedance probability (P_E) by applying a Weibull distribution. Third, to distinguish the effect of tidal range on the spatial distributions of undertow by utilizing the observed exceedance probability of undertow. The exceedance probability and Weibull distribution which performed in the analysis method will be respectively explained in Section 2.3 and 2.4.

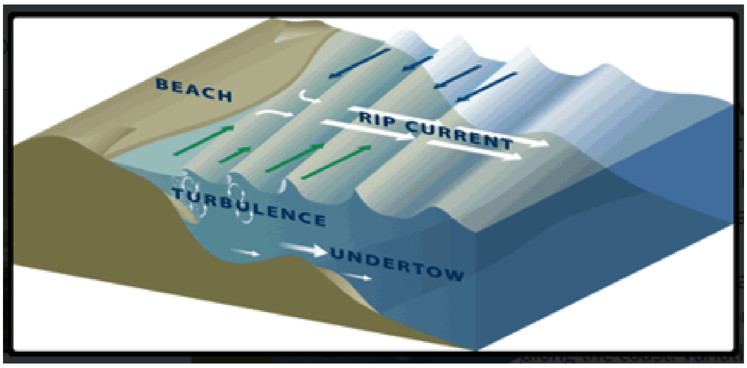

Figure 2.1: Nearshore currents (Woods Hole Oceanographic Institution, USA [77]).

2.1 Wave-generated nearshore current: undertow

In the previous time, an incidence wave had been though as a purely oscillatory motion, but the field measurements observed the velocity field under wave propagation. Although the magnitude of velocity was small in the offshore site, the cumulative effect behind beach erosion or acceleration was significant. Especially, nearshore currents induced by wave driving force should be more considered, because the force from the imbalance of the radiation stress and the opposing uniform pressure gradient can lead to the generation of currents, that move sediment particle in alongshore and cross-shore directions.

In a calm situation, incoming waves are regular in the offshore zone and shoreward propagate with a net flow above wave trough, or called Eulerian drift (Eq. 2.1). This Eulerian net flow is normally compensated by a return flow under wave trough, which was assumed as the mean uniform steady velocity and its magnitude equaled to the depth-averaged Eulerian net flow under wave trough level (Eq. 2.2), see Fig. 2.2.

$$Q_{E-net} = \frac{gH^2}{8C}, \tag{2.1}$$

$$\langle u_{stokes} \rangle = \frac{gH^2}{8Ch_T}. \tag{2.2}$$

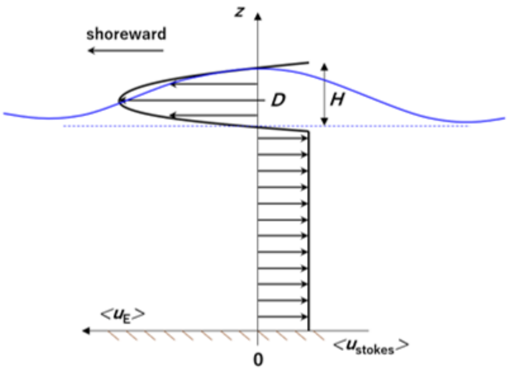

Figure 2.2: Eulerian net flow velocity resulting form compensating a steady flow based on continuity consideration.

However, the velocity field is not actually inviscid distribution due to the effect of bed roughness as most of existing measurements have found a shoreward net velocity near the bed under non-wave-breaking condition. The Eulerian mean velocity for the case of laminar flow and constant eddy viscosity can be calculated by Longuet-Higgins solution [49] given as

$$\langle u_E \rangle = \frac{(A\omega)^2}{4C}[3 + e^{-\xi}(-4\cos\xi + 2\sin\xi + e^{-\xi} - 2\xi\sin\xi + 2\xi\cos\xi)], \tag{2.3}$$

where $\xi = z/\sqrt{2\nu/\omega}$.

In regard to the surf zone, because the gravity force related to wave set-up drives the velocity and there is no shoreward boundary drift, the seaward mean velocity is observed to be stronger than the offshore zone or so-called undertow. The undertow occurs when waves are breaking and the wave-volume flux owing to wave motion and surface roller creates the non-uniform radiation stress gradient that is imbalance to the uniform pressure gradient form the wave set-up over the depth. Fig. 2.3 shows the vertical distribution of undertow in the surf zone.

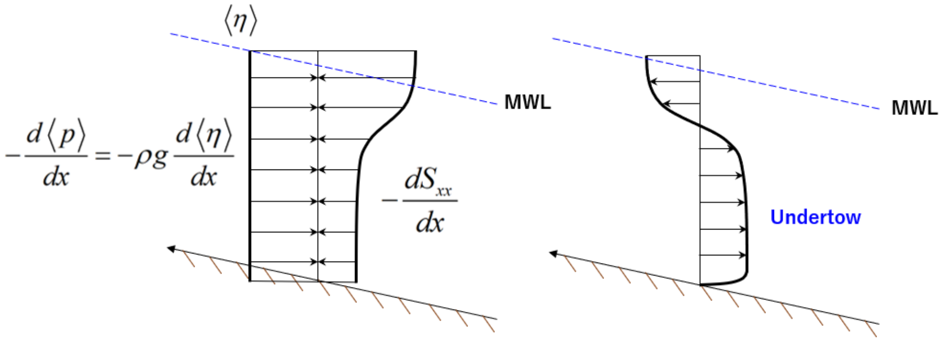

Figure 2.3: Vertical distribution of undertow occurred in the surf zone.

2.2 Numerical models of undertow

Undertow model was first developed to simply calculate the mean value of undertow velocity. After that, the model was expected to use as a part of the prediction of sediment transport rate, therefore, it was then improved for calculating the vertical distribution of undertow by assembling the effect of eddy viscosity and also validated by comparing with the experimental results. Because the undertow velocity is dominated by the mass flux due to wave motion and surface roller [97], the models of wave transformation and surface roller are integrated in the undertow calculation. The individual contributions of wave transformation and surface roller evolution to the undertow velocity, including the improvements of undertow model, will be properly described before moving to the explanation of analysis in Chapter 3.

2.2.1 Wave transformation model

Kuriyama developed a wave transformation model that can solve the shoaling, breaking and reforming of individual waves [41]. Specially, Kuriyama modified the criteria on wave breaking by combining a dimensionless coefficient C_{br} into the solution of Seyama and Kimura [87], in order to adjust the solution based on the measurement data to be used for the field data. The equation of breaking criteria became

$$\frac{H_b}{h_b} = C_{br}\left[0.16\frac{L_o}{h_b}\left[1-\exp\left(-0.8\pi\frac{h_b}{L_o}(1+15\tan^{4/3}B)\right)\right]-0.96\tan B+0.2\right], \tag{2.4}$$

and a periodic bore model proposed by Thornton and Guza is used to estimate wave energy dissipation due to wave motion [101], which can be expressed as,

$$\frac{\partial E_f C_G}{\partial x} = \frac{1}{4}\frac{\rho g(C_o H)^3}{hT}, \tag{2.5}$$

where C_o is a dimensionless coefficient indicating the amount of the dissipation term. The formula of C_o was introduced by Kuriyama and Ozaki [41] as,

$$C_o = C_B\left[1.6-0.12\ln\left(\frac{H_o}{L_o}\right)+0.28\ln(\tan B)\right]. \tag{2.6}$$

The given-minimal error for predicting undertow velocity, which is caused by the error from predicting wave height, is when C_{br} and C_B range from 0.7 to 1.2 and from 0.7 to 1.1, respectively [44].

Although the wave transformation model gave a good agreement with the observed wave data, the deficiency showed that the modeled undertow was underestimated mean velocities [44]. A cause of this error is that the wave transformation model was derived from the assumption of symmetric waves, which inaccurately calculated asymmetric waves in shallow water [22].

Later, a random wave transformation model was developed by Mase on the basis of the energy balance with the considerations of wave diffraction and dissipation effects due to wave breaking [52]. Afterward, Nam modified the model with an improved description of the energy dissipation due to wave roller [62]. The model was expressed as,

$$\begin{aligned}\frac{\partial(C_xS)}{\partial x}+\frac{\partial(C_yS)}{\partial y}+\frac{\partial(C_\theta S)}{\partial\theta} &= \frac{\kappa}{2\omega}\left[(CC_G\cos^2\theta S_y)_y-\frac{1}{2}CC_G\cos^2\theta S_y\right]\\ &\quad -\frac{K}{d}C_GS\left[1-\left(\frac{\Gamma h}{H_s}\right)^2\right],\end{aligned} \tag{2.7}$$

where the dimensionless coefficients of stable wave height (Γ) and decay (K) are expressed by the function of bottom slope [28] as,

$$\Gamma = 0.45, K = \frac{3}{8}(0.3 - 19.2B) \quad \text{for } B < 0, \tag{2.8}$$

$$\Gamma = 0.45 + 1.5B, K = \frac{3}{8}(0.3 - 0.5B) \quad \text{for } 0 \leq B \leq 0.6. \tag{2.9}$$

Dally et al. suggested the calculation of wave energy dissipation due to wave breaking (D_b) by the following equation [17],

$$D_b = \frac{\rho g K C_G}{8d}\left[H_{rms}^2 - (\Gamma h)^2\right], \tag{2.10}$$

the radiation stress due to wave motion can be determined as,

$$S_{xx} = \frac{E_f}{2}\left[2n\left(1 + \cos^2\langle\theta\rangle\right) - 1\right], \tag{2.11}$$

$$S_{yy} = \frac{E_f}{2}\left[2n\left(1 + \sin^2\langle\theta\rangle\right) - 1\right], \tag{2.12}$$

$$S_{xy} = \frac{E_f}{2} n \sin 2\langle\theta\rangle. \tag{2.13}$$

For calculating the volume flux due to the wave motion (Q_w), it was assumed to be proportional to the root-mean-square of water surface elevation of an individual waves (ζ_{rms}) as the below equation developed by Svendsen [97],

$$Q_w = -\frac{C}{h}\zeta_{rms}^2, \tag{2.14}$$

the ζ_{rms} value is a function of significant wave height that derived from the nonlinear wave theory using experimental results given by Goda [27]. The obtained relations are written as,

$$\zeta_{rms} = \frac{H}{2\sqrt{2}} \quad \text{for } \Pi < 0.15, \tag{2.15}$$

$$\zeta_{rms} = \frac{H}{1.668\log\Pi + 4.204} \quad \text{for } 0.15 \leq \Pi < 3, \tag{2.16}$$

$$\zeta_{rms} = \frac{H}{5} \quad \text{for } \Pi \geq 0.15, \tag{2.17}$$

where Π indicates non-linearity of an individual wave as given,

$$\Pi = \frac{H_s}{L}\coth^3\left(\frac{2\pi h}{L}\right). \tag{2.18}$$

2.2.2 Surface roller model

After developing of the calculation of wave dissipation by Dally, Nam et al. [62] improved the model for mass transport due to the wave roller effect as,

$$\frac{\partial}{\partial x}\left(\frac{1}{2}MC_r^2\cos^2\langle\theta\rangle\right)+\frac{\partial}{\partial y}\left(\frac{1}{2}MC_r^2\sin^2\langle\theta\rangle\right) = D_r - D_b, \tag{2.19}$$

where D_r is the dissipation due to roller effect with an equation given below,

$$D_r = \delta g M, \tag{2.20}$$

the radiation stress due to roller can be expressed by,

$$R_{xx} = MC_r\cos^2\langle\theta\rangle, \tag{2.21}$$

$$R_{yy} = MC_r\sin^2\langle\theta\rangle, \tag{2.22}$$

$$R_{xy} = MC_r\sin 2\langle\theta\rangle. \tag{2.23}$$

Regarding the volume flux due to the surface roller (Q_r), the calculation can be expressed as Eq. 2.24. The cross-section area of the roller (A_r) had been significantly considered with the first assumption that it was proportional to the square of wave height [68, 97] as Eq. 2.25,

$$Q_r = -\frac{A_r C}{2L}, \tag{2.24}$$

$$A_{r1} = C_A H^2. \tag{2.25}$$

In addition, Nadaoka et al. found that the shoreward cross-shore velocity was fast at wave crest and became slower to wave trough level as being the triangle distribution dut to eddy viscosity [61]. Suddenly, it was rapidly changed to flow in seaward direction with the magnitude of velocity equaled to wave celerity (C). Fig 2.4 presents the assumed distribution of the time-average cross-shore current velocity. However, when a wave is propagating and the energy of wave motion is transferring to generate surface roller, this energy of the roller should be less than the initial energy. The roller area under the consideration of without wave dissipation by Kuriyama [44] was then determined not to exceed A_{r2} with the equation given as,

$$\frac{\partial(E_f C_G)}{\partial x}+\frac{\partial(MC)}{\partial x} = 0, \tag{2.26}$$

then,

$$A_{r2} = \frac{8ML}{\rho C^2}, \tag{2.27}$$

from these two calculated roller areas, the smaller value was chosen for Eq. 2.24.

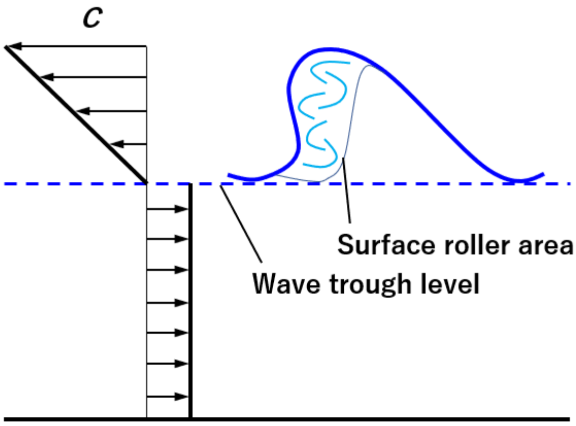

Figure 2.4: Assumed distribution of the time-average cross-shore current velocity.

2.2.3 Modeling mean undertow velocity

A basic model for time and depth-averaged undertow velocity was obtained by Svendsen [97], who suggested that undertow is induced by both of volume flux due to wave motion and surface roller as computed from Eq. 2.14 and Eq. 2.24, respectively. Undertow characteristic is limited in the surf zone and varies on water depth from seabed to wave trough level (h_T). The three important variables of wave volume flux due to wave motion and surface roller, and water depth were accounted for the equation of mean undertow velocity as (Fig 1.2),

$$\langle u_E \rangle = -\frac{Q_w + Q_r}{h_T}. \tag{2.28}$$

All of the parameters in Eq. 2.28 above can be calculated by any proposed contributions which were developed by the different assumptions. With respect to the volume flux, Rattanapitikon and Shibayama had re-analyzed the existing undertow models, and validated against the number of 379 undertow profiles of six different data sets in both small and large-scale laboratories, in order to develop the most appropriate undertow model that can be used even in a calculator. Although the best recommended solution gave good agreement with observed data and the deficiency was approximately 15% for mean undertow calculation, the bed roughness at bottom boundary layer was not included in the solution, and the larger error was found after comparing undertow profiles in a large-scale experiment [76].

In addition to the wave energy flux, the accuracy of undertow prediction depends on the estimation of the water depth under wave trough level [63] as the previous experiments have observed the stronger undertow velocity on a bar region and the weaker undertow velocity on a trough region. Even in a low-energy wave condition, undertow is still sensitive to water depth. For this reason, the calculation of water depth under wave trough need appropriately considering. Previously, the wave trough level could be estimated by a half of the root-mean-square value of individual wave height. This might be properly for only symmetric waves in the offshore but it is not enough for asymmetric waves in the nearshore [26]. Many significant investigations related to the wave asymmetry was conducted. Drake and Calantoni distinguished the effects of wave skewness and asymmetry by using the Stokes higher-order theory [21]. The quantities of local waves were combined into the prediction of stream flow velocity near the bed by Elfrink et al. [23], and the description for the characteristics of individual wave shape was expensively clarified by Abreu et al. [3], including an improved analytic formulation of free-stream velocity. Ruessink modified the Abreu's formulation by applying the Ursell number for random waves [85]. Recently, Nam et al. [63] followed the study of Ruessink to solve water depth below asymmetric wave trough as determined by the wave theory below,

$$h_T \quad = \quad h + \eta_{up} - W_{L_{rms}}, \tag{2.29}$$

$W_{L_{rms}}$ is assumed as a function similar to the solution of Abreu et al.,

$$W_L(t) \quad = \quad \frac{H_{rms} f}{2} \left(\frac{\sin \omega t + \frac{r \sin \phi}{1+\sqrt{1-r^2}}}{1 - r\cos(\omega t + \phi)} \right), \tag{2.30}$$

where $f = \sqrt{1-r^2}$ and the wave form parameter (ϕ) is a function of the Ursell number as the following equation,

$$\phi \quad = \quad -\frac{\pi}{2} \tanh\left(\varphi_1 / U_r^{\varphi_2}\right), \tag{2.31}$$

the Ursell number (U_r) can be expressed by

$$U_r \quad = \quad \frac{H_{rms} L^2}{(h + \eta_{up})^3}, \tag{2.32}$$

where r is the index of wave skewness, which is also based on the Ursell number given as,

$$r \quad = \quad \frac{2\sqrt{m}}{1+m}, \tag{2.33}$$

$$m \quad = \quad \left(\frac{\sqrt{(1-m^2)}}{3} \right) \left(\varphi_3 + \frac{\varphi_4 - \varphi_3}{1 + \exp \frac{\varphi_5 - \log U_r}{\varphi_6}} \right), \tag{2.34}$$

with the recommended fitting parameter (φ) given by Ruessink ey al. [85] as,

$$\varphi_1 = 0.815 \pm 0.055, \qquad \varphi_2 = 0.672 \pm 0.073, \qquad \varphi_3 = 0,$$
$$\varphi_4 = 0.857 \pm 0.016, \qquad \varphi_5 = -0.471 \pm 0.025, \qquad \varphi_6 = 0.297 \pm 0.021.$$

2.3 Exceedance probability

The exceedance probability is an interesting method to evaluate the possibility of experiencing a serious condition. To continuously explaining, the basic equation for the measured exceedance probability is expressed by Eq.3.4 in Chapter 3 for continuously explaining in the analysis method.

The exceedance probability is used to assess the probability percentage of an uncertain parameter exceeding a certain threshold and it is often interested in offshore engineering to evaluate the various hydrodynamic properties: wind, wave, current, and sea ice [25]. For examples, Pugh [73] utilized the measured current datasets from the Lincolnshire coast in the North sea [74] with tide-surge probability techniques to investigate the exceedance probability of an annual extreme current under a strong seasonal condition. The optimum value of the extreme current was then required to suitably design the offshore structures. Method of applying the joint exceedance probability to the wave height datasets was also considered by Stansell et al. [90]. The discretisation on sea water level to filter wave height resulted in serious underestimation of the probability of extreme wave condition for a low sampling rate of 1 Hz or less. Plus, the exceedance probability of the maximum wave height in 3 hours was 5% underestimated.

Relating to the coastal engineering field, the cross-shore distributions of longshore current velocity at HORS was observed by Kuriyama et al. [43]. The explanation of the extreme longshore current velocities of 0.5 and 1.0 m/s at some considered locations were valued by using exceedance probability. Later, a statistical model applying exceedance probability for pressure gradients was developed by analyzing the measured data from large-scale experiment, as published by Suzuki et al. [96]. After that, Suzuki et al. [95] was similarly conducted a field observation at the natural beach (HORS) in February 16, 2007. The measurements of pressure gradients were performed by using five pressure transducers. Finally, a statistical model of exceedance probability of near-bed pressure gradients was developed.

In addition to the investigations mentioned above, some researchers have also utilized the exceedance probability for investigations into sediment transport trends [39], shoreline erosion [15], and extreme waves forced by wind [57] etc.

2.4 Weibull distribution

There are several empirical and theoretical models which can be applied to fit the exceedance probability. Weibull distribution is one of highly recommended functions for various applications in engineering filed [45, 46, 111], especially for the flood frequency responding to civil engineering [70]. Regarding the analysis of pressure gradients using measured experimental and field data, Suzuki et al. [96, 95] compared the measured exceedance probability of pressure gradients with the modeled results using four methods of Weibull distribution, Rayleigh distribution, formulation of Al-Humoud et al. [5] and Edgeworth-Rayleigh distribution [58]. The measured datasets were well estimated by the Weibull distribution rather than other methods. According to the well-estimated results, the Weibull distribution was generalized to develop a statistical model for simply predicting pressure gradients.

Moreover, the contributions of 12-year simulated data with the WAM model and ECMWF wind forcing to the estimation of design wave characteristics for Kuwaiti territorial waters were operated by Neelamani et al. [64]. The extreme wave conditions were estimated by employing Weibull and Gumbel distributions. For their findings, the Weibull distribution is better fitted to the storms compared with the Gumbel distribution in Kuwaiti territorial waters.

The approach of defining reduced variate for Weibull distribution is provided here. A probability that absolute of any undertow velocity $|u'_E|$ is equal to or less than that of a specified undertow velocity $|u_E|$ is defined as,

$$P = P\left(|u'_E| \leq |u_E|\right). \tag{2.35}$$

The exceedance probability that $|u'_E|$ is greater than a specified undertow velocity $|u_E|$ may also be defined as:

$$P_E = P_E\left(|u'_E| > |u_E|\right) = 1 - P. \tag{2.36}$$

Following the publications of Kamphuis [38] and Scholz [86], the 2-parameter Weibull distribution function is given as,

$$P(x_i) = 1 - \exp\left(-\frac{x_i}{a'}\right)^b, \tag{2.37}$$

where $a = \frac{1}{a'}$ and x_i is defined as a considered parameter or the normalized value of undertow velocity ($u_E/\overline{u} = \beta$) in this research. Then,

$$P(\beta) = 1 - \exp\left(-a\beta\right)^b, \tag{2.38}$$

which results in Eq. 3.5 for the exceedance probability of undertow velocity.

Chapter 3

Methodology

Field observations were conducted at the Hasaki coast, Japan, in May of 2016 and 2017. The nearshore currents, wave and wind conditions, and bathymetry profile were measured. Based on the wave energy flux from high to low levels, the undertow current velocity data were rearranged. Then, the exceedance probability (hereafter P_E) method was applied to illustrate the characteristics the undertow distributions. The undertow distribution was fitted by several functions; however, the Weibull distribution shows the best fitting with the smallest error. Here, the Weibull parameters present a correlation with an undertow coefficient (or an efficiency of undertow), and the generalized equations are given for predicting undertow P_E. The flow chart of statistical analysis scheme is presented in Fig. 3.1.

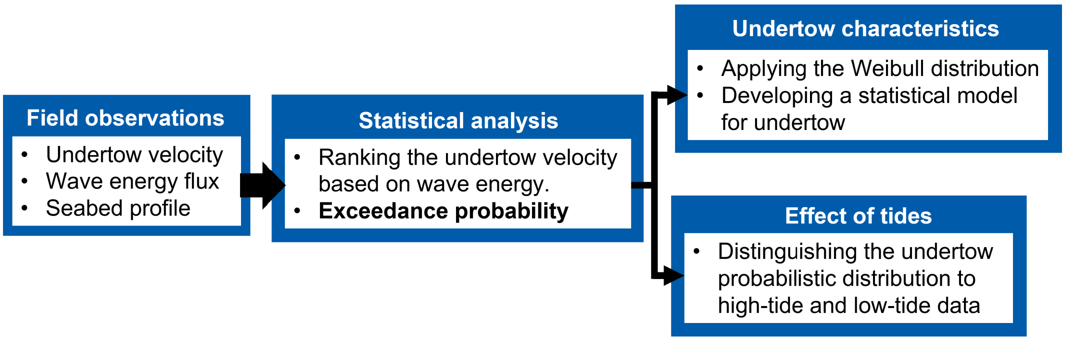

Figure 3.1: Flow chart of research methodology for statistical analysis.

3.1 Location of study site

Field observations were conducted on an alongshore beach, Hasaki coast, where located in the Ibaraki Prefecture of Japan facing the South Pacific Ocean at Hasaki Oceanographical Research Station (HORS), a research facility for various phenomena in the nearshore zone owned by the Port and Harbour Research Institute, Ministry of Transport (Fig. 3.2). The beach is dominated with sea and swell waves, and significantly annual shoreline retreat is significantly being occurred due to tropical cyclones-generated high wave energy [4]. The bathymetry of the alongshore profile is almost uniform [42], with a median sediment diameter of 0.18 mm [32].

HORS has a 427-m-long pier located perpendicular to the shoreline, and the pier is angled 59° clockwise from the north (Fig. 3.3). For this research, the seaward distance parallel to the pier was defined as x being positive, and the alongshore direction perpendicular to the pier was defined as y being respectively positive and negative in southward and northward directions with the reference point (x and $y =$ 0 m) set at the entrance of the pier. Beach profiles were measured at 5-m intervals along the pier by using a 3-kg lead.

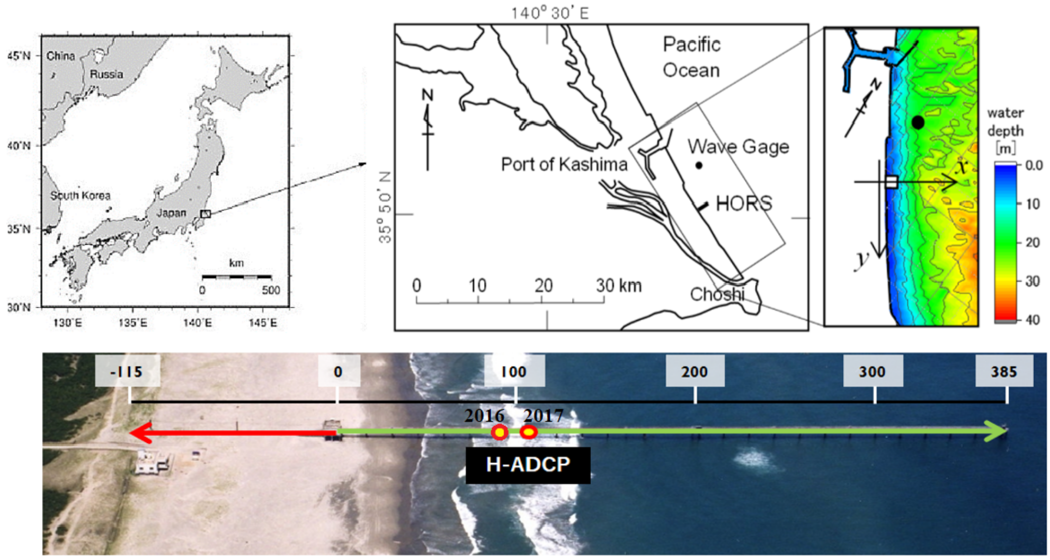

Figure 3.2: Location of the Hasaki Oceanographical Research Station (HORS) and bathymetric map of the study site (Japan Oceanographic Data Center).

Figure 3.3: A 427-m-long pier located at HORS, Japan.

3.2 Field observations

Field observations were conducted during two periods under different topography conditions on an alongshore uniform beach on the Hasaki coast in Japan. The first period spanned 21 days from May 13 to June 2 in 2016 (hereafter HC16), and the second period spanned 13 days from May 9 to May 22 in 2017 (hereafter HC17). Table 3.1 shows the description of the field observation.

Table 3.1: Description of the field observations.

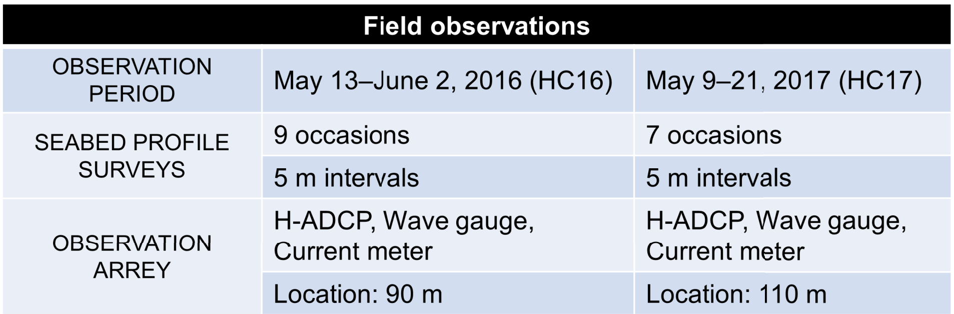

Field observations		
OBSERVATION PERIOD	May 13–June 2, 2016 (HC16)	May 9–21, 2017 (HC17)
SEABED PROFILE SURVEYS	9 occasions	7 occasions
	5 m intervals	5 m intervals
OBSERVATION ARREY	H-ADCP, Wave gauge, Current meter	H-ADCP, Wave gauge, Current meter
	Location: 90 m	Location: 110 m

3.2.1 The 2016 field observations (HC16)

In the first period of HC16, seabed profiles were measured at intervals of 5 m for 9 occasions as presented by Fig. 3.4. The inner and outer sandbars were observed. An observation array for measuring nearshore currents, wave height and water level was installed at the location of $x = 90$ m. The yellow area indicates the beam from H-ADCP. To investigate the undertow characteristics at various water depths along the seaward distance at which the wave was propagating, the undertow velocity observed at the locations of $x = 96$, 116, 126, 161 and 191 m are selected. The pink, yellow, blue, green and red circles indicate the fluorescent tracer sands installed at $x = 70$, 120, 170, 220 and 280 m, respectively. The explanation of data acquisition and data filtering is given in Section 3.2.3.

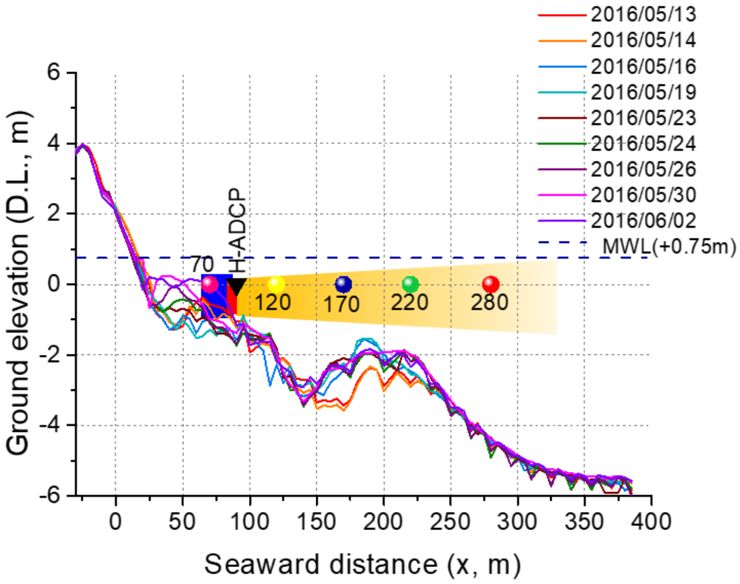

Figure 3.4: Barred beach profile of the field observation in May, 2016 (HC16).

3.2.2 The 2017 field observations (HC17)

In the second period of HC17, seabed profiles were surveyed for 7 occasions during the observation. Fig. 3.5 presents observed seabed profiles that were smooth and had no sandbar. An observation array for measuring nearshore currents, wave height and water level was installed at the location of $x = 110$ m. The datasets of undertow velocity at the locations of $x = 116$, 126, 161, 191 and 221 m are selected for this analysis. The green, yellow and red circles indicate the fluorescent tracer sands installed at $x = 80$, 160 and 240 m, respectively.

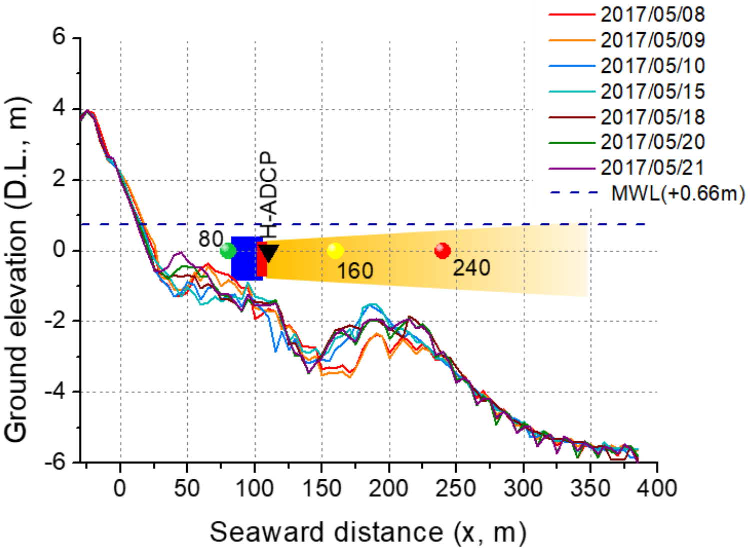

Figure 3.5: Unbarred beach profile of the field observation in May, 2017 (HC17).

3.2.3 Data acquisition and data filtering

At the beginning of HC16, an observation array was installed at the location of x = 90 m at a clockwise angle of 10° from the pier to avoid disturbances from the front piles as shown in Fig. 3.6. The distance from the center of the array (-0.46 m, D.L.) to the seabed was 0.60 m. Three instruments were combined in this array: a wave gauge, a current meter (INFINITY-EM, JFE Advantech Co., Ltd.), and a 600-kHz nominal Horizontal Acoustic Doppler Current Profiler (H-ADCP 600, Teledyne RD Instruments Marine Measurements) with the technical specifications of 180-m longest horizontal profiling range and 2.1° beam width.

The H-ADCP sensor can be functionally set up by users for appropriately measuring hydrodynamic parameters, water quality, and water surface elevation in the various condition. In this observation, the nearshore currents and water level were collected with a 1-min period in every 5 min at 5-m intervals during the observation period with a sampling rate of 1 Hz, and a first bin was 6.0 m far from its position. The outputs were taken by the WinADCP software, and the observed currents were then converted into cross-shore and longshore currents (u, v) with positive directions being shoreward and southward, respectively.

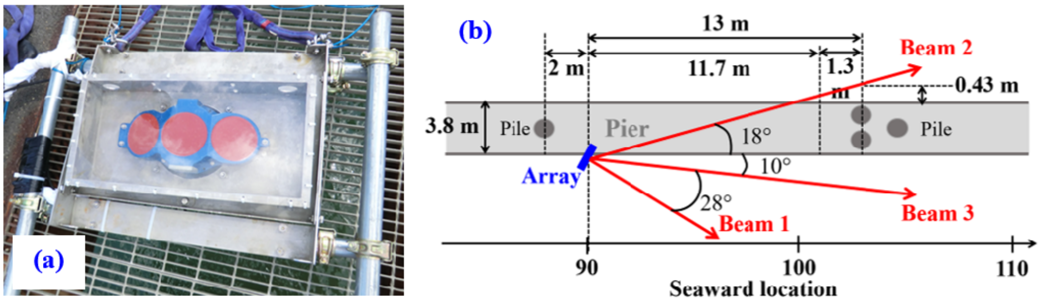

Figure 3.6: (a) An observation array complemented by three instruments: a wave gauge, a current meter and H-ADCP. (b) Emplacement of the observation array in HC16.

The wave datasets were taken from two locations: At the Kashima port, the offshore waves (H_o, T_o) were measured at a water depth of 23.4 m using an Ultra-Sonic Wave gauge (USW) organized by the nationwide ocean wave information network for ports and harbours (NOWPHAS), Japan. At the tip of the pier (x = 380 m), the significant waves (H_s, T_s) were observed using a wave gauge (UH-401, KENEX) at a mean water depth of 6.36 m and averaged every hour by a 20-min data sample. However, the wave directions were observed only at the offshore site (θ_o) and calculated with the Snell's law to estimate the wave direction at the tip of the pier (θ). The wave energy flux per unit length was calculated by the equations are as follows;

$$E_f = \frac{1}{8}\rho g H_s^2 C_G, \tag{3.1}$$

$$C_G = nC, \tag{3.2}$$

$$n = \frac{1}{2}\left(1 + \frac{2kd}{sinh2kd}\right) \tag{3.3}$$

For the wind situation, a propeller-style vane anemometer (N-363, Nippon Electric Instrument) installed at the end of the pier at x = 385 m was used to measure the speed and direction of wind. The dataset were averaged to every 10 min for every hour. An example of hourly averaged data of cross-shore currents, wave height and water level was illustrated in Fig. 3.7. All of datasets were averaged at the first 20 min in each hour to match them with the same sampling rate. The gray horizontal lines refer to the rate of time-averaged data.

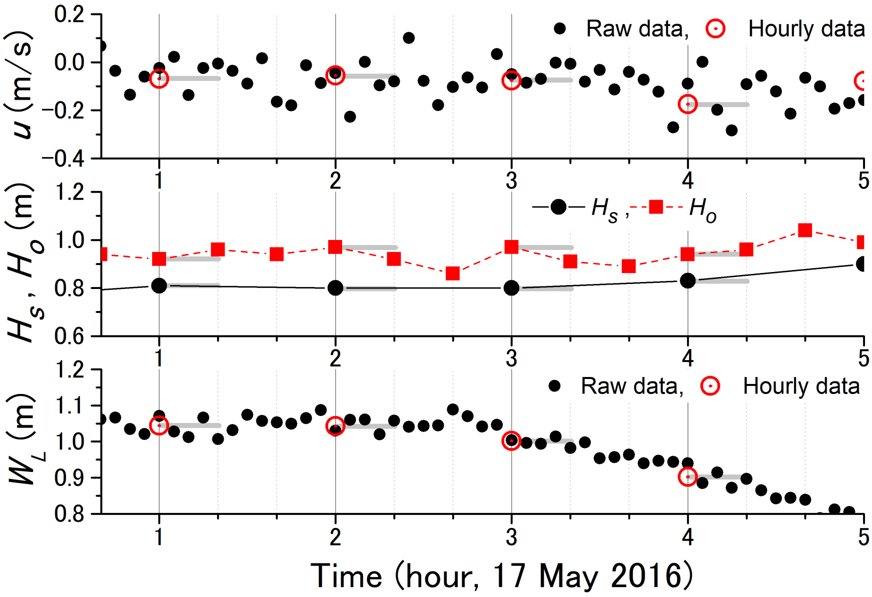

Figure 3.7: Example of data filtering of the (top) cross-shore current, (middle) wave height, and (bottom) water level during 00:40–05:00 AM on May 17, 2016. The black dots and open circles indicate raw and average data. The gray horizontal lines indicate the time of the averaging. The red rectangle represents the 20-min observed wave height at NOWPHAS.

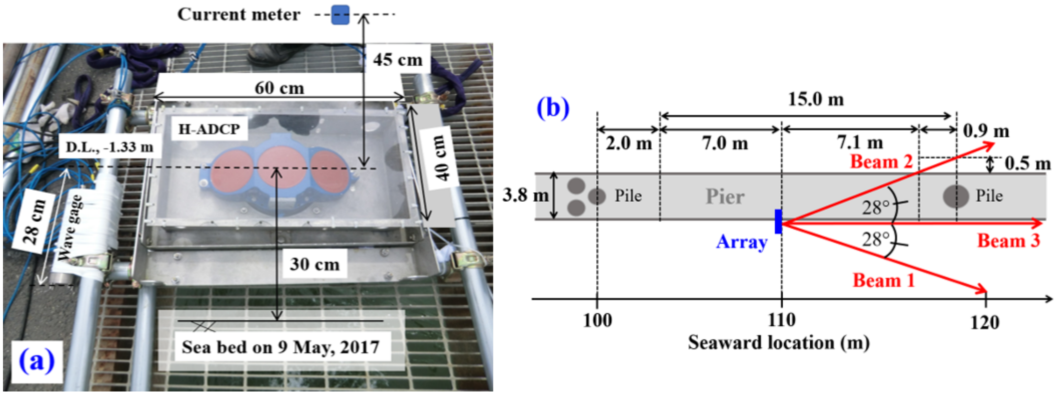

Figure 3.8: (a) An observation array complemented by three instruments: a wave gauge, a current meter and H-ADCP. (b) Emplacement of the observation array in HC17.

The installation of the observation array in HC17 was different from 2016. Fig. 3.8 illustrates the components and the emplacement of the observation array. The position of array was at the location of x = 110 m, where it could well measure current velocities and was not disturbed by the front piles. Because of that, the array was installed without an inclining angle; beam-3 was parallel to the pier. The distance from the center of the array (-1.33 m, D.L.) to the seabed was 0.30 m and the first bin was at about x = 116 m. Three of the same instruments used in 2016 were also put in this array. Moreover, the wave direction driving longshore gradient shows a deficiency angle with the longshore current. Next, the differences of the emplacement and occurred deficiency of the HC16 and HC17 are respectively illustrated.

3.2.4 Correlation between observed longshore current and wave direction

The wave directions at the end of the pier (θ) were estimated by the wave direction observed at the offshore site (θ_o) at a water depth of 23.4 m, which acquired through the Nationwide Ocean Wave information network for Ports and HArbourS (NOWPHAS), using Snell's law.

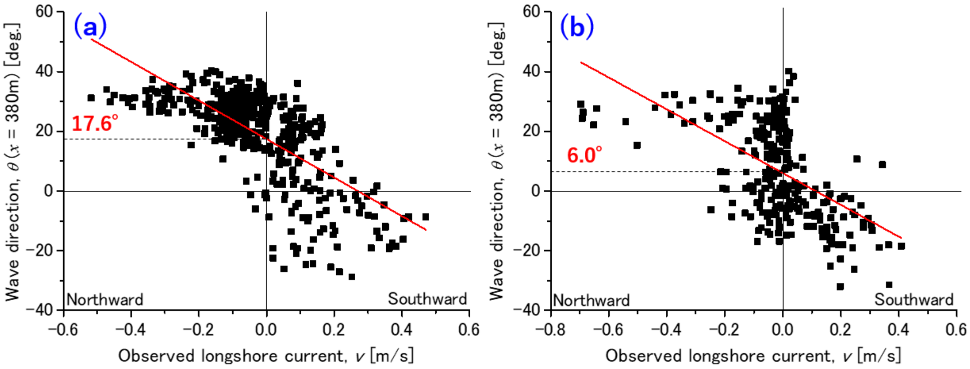

Figure 3.9: Correlation between the observed longshore current and adjusted wave direction for (a) HC16 and (b) HC17.

However, wave-generated longshore momentum dominates the longshore current. The larger the incident wave angle is, the stronger the longshore current velocity. Fig. 3.9 presents the correlation between the longshore current obtained at the first bin of the H-ADCP position ($x = 96$ m and 116 m for HC16 and HC17, respectively) and the calculated wave directions. This reveals a discrepancy indicating the effect of the wave refraction. Therefore, after using Snell's law, the wave directions were again adjusted with a shifted angle of 17.6° and 6.0° to the origin for HC16 and HC17, respectively. In this analysis, the cross-shore component of the wave energy flux (E_{fu}) mentioned in Section 4.1.3 and 4.2.3 were then converted using this final adjusted wave direction (θ_s).

3.3 Analysis of undertow exceedance probability

The probabilistic distribution of undertow current is described by using the exceedance probability (P_E) with the consideration of occurrence probability in an extreme condition. The basic equation for the measured P_E is given by

$$P_E = \frac{\alpha}{N_0 + 1}, \tag{3.4}$$

where α is the order of the high to low amount of normalized undertow (i-th rank of $u_E/\overline{u}$), and N_0 is the sum of the number data for the different wave energy levels and cross-shore locations.

An example of the wave-energetic distribution of undertow P_E at the location x = 126 m of HC16 (Fig. 3.10) is given to demonstrate the procedure of analysis. The dots represent the data plotted between the values of normalized undertow velocity and its P_E value. Each wave energy level is represented by different colors. After that, the data of undertow P_E were well-fitted by using the Weibull distribution. The P_E of the Weibull distribution is expressed as Eq. 3.5, and the explanation of the Weibull distribution was mentioned in Section 2.4.

$$P_E = \exp(-a\beta^b) \tag{3.5}$$

where a and b are two important parameters known as the scale and shape parameters, respectively, and β is the value of $u_E/\overline{u}$.

P_E can normally be examined by several empirical models; e.g., a Weibull distribution, Gumbel distribution, Generalized Extreme Value (GEV) distribution, or Rayleigh distribution. In coastal applications, the Weibull distribution has widely been utilized to increase the understanding of hydrodynamic mechanisms on a coast; wave runup [103], polymodal sediment [92], and long-shore currents [29]. Moreover, this Weibull distribution is an uncomplicated function compared to other models to be used in practice. Thus, the author chose the Weibull distribution to fit the curves of the distribution of undertow P_E in this research.

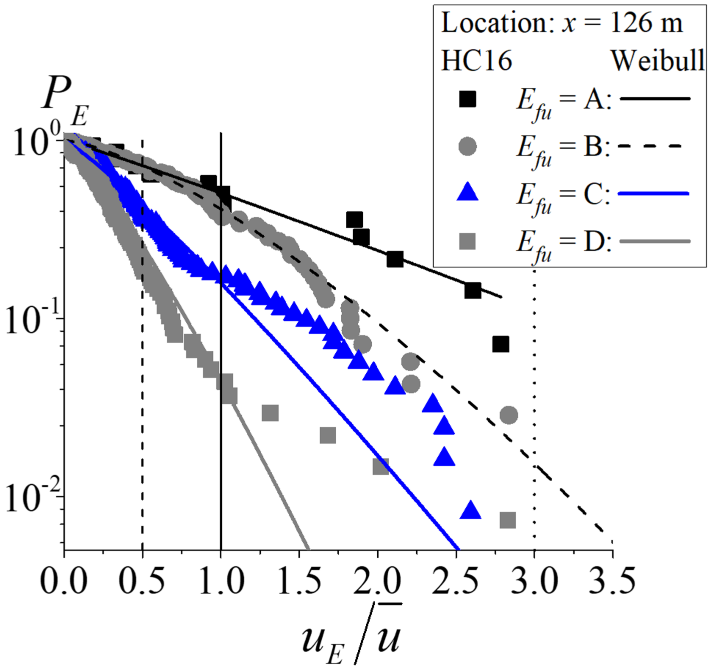

Figure 3.10: Exceedance probability of observed and Weibull distributions applicable to normalized undertow at the location x = 126 m of HC16.

When applying the Weibull distribution to each observed P_E curve, the curves were well fitted by changing the Weibull parameters. It can be considered that the parameters were affected by the normalized values of the wave energy flux, relative cross-shore location, and normalized water depth. This brings about the development of the statistical model for predicting undertow P_E, and this will be later discussed together with both results of HC16 and HC17 datasets in Section 5.4 of Chapter 5.

To demonstrate the effect of tidal ranges on the undertow, the observed P_E of undertow was distinguished using the water levels: high-tide or low-tide data. The definitions of high-tide and low-tide durations in this study were determined by using the values of MWL and its standard deviation. The description relating to this part will appear in Section 5.5 of Chapter 5.

Chapter 4

Field Datasets

In this chapter, the field datasets and the undertow analysis are described, including the generalization of the Weibull distribution to develop a statistical model for estimating undertow. Tidal elevation data are used to demonstrate the characteristics of undertow probabilistic distribution differentiated by changes in water level.

4.1 Data description for the field observation in May 2016 (HC16)

The observed datasets of HC16 are described in three main folds as follows:

- **Bathymetry profile**
- **Wave condition**
- **Variability of cross-shore current**

The description of the HC17 that presents a different feature of planar beach will be given in Section 4.2.

4.1.1 Bathymetry profile of HC16

Fig. 4.1 presents beach profiles surveyed in HC16. Initial, final and average seabed profiles are represented by brown, red and black lines, respectively. Gray bound scopes standard deviation of seabed elevation in each location. Two sandbars were observed around x = 60 and 190 m. The mean water level (MWL) was +0.75 m relative to the datum level at the site (Tokyo Peil -0.687 m). In this research, the position of the shoreline was set at the still MWL. x_L indicates a distance measured from shoreline to a considered location, X_B refers to the location of the outer sandbar at $x = 191$ m, and x_L/X_B is a considered location relative to the outer bar. Five seaward locations of $x = 96$, 116, 126, 161, and 191 m ($x_L/X_B = 0.46$, 0.57, 0.63, 0.83, and 1.00) are discussed in the analysis. In addition, W_L is water level, h is the water depth from the water surface to the seabed at the location of x, and h_B is the depth at the outer bar. Between the inner and outer bars, the depth at the trough ($x = 161$ m) was 3.20 m below the MWL.

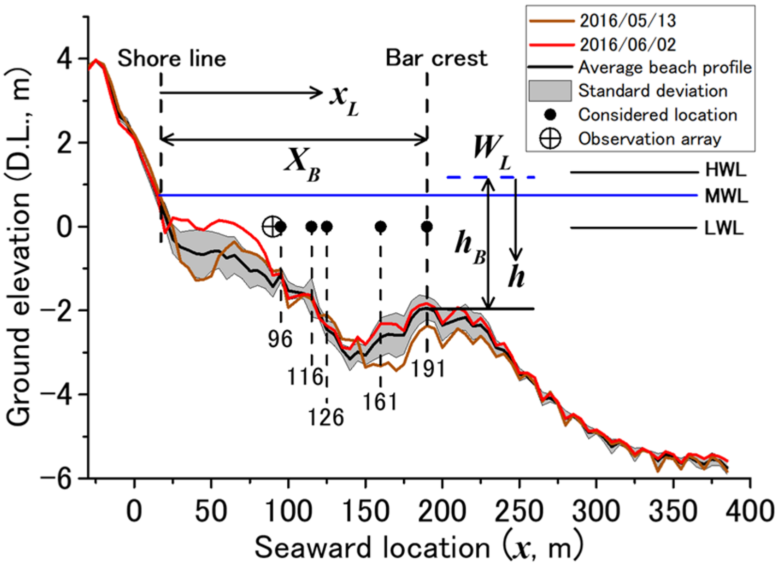

Figure 4.1: Beach profile of HC16 with average and standard deviation.

4.1.2 Wave condition of HC16

The time-series data of wave height, wave period and wave direction are presented in Fig. 4.2. The red and black lines refer to waves observed at the tip of the pier ($x = 380$ m) and the offshore site at a water depth of 23.4 m (NOWPHAS), respectively. The offshore wave direction (θ_o) in Fig. 4.2c was recorded as a positive angle of a clockwise rotation, where 0° denotes the direction parallel to the pier from offshore to onshore. The significant wave directions (θ) were then estimated by using the offshore wave direction calculated with Snell's law as mentioned in Chapter 3.

The significant wave observed at the tip of the pier was used for the analysis. The average wave height ($\langle H_s \rangle$) was 1.00 m with a range of 0.47 m $< H_s <$ 2.39 m, and the average wave period ($\langle T_s \rangle$) was 7.07 s with a range of 4.40 s $< T_s <$ 9.30 s.

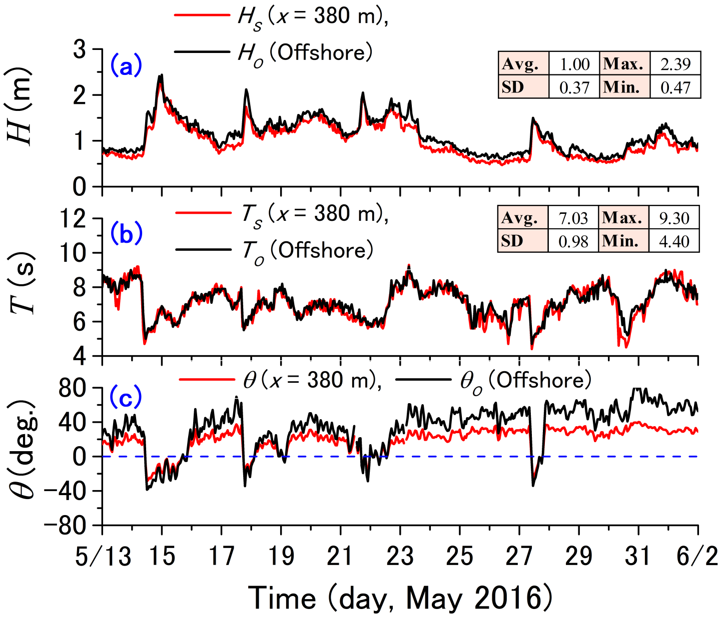

Figure 4.2: Time-series data indicating wave condition in HC16: (a) wave height, (b) wave period, and (c) wave direction.

The wave height was relatively higher than the average from May 14 to 24 because of a storm event. In addition, The average wind velocity ($\langle U \rangle$) was 5.63 m/s with a range of 0.24 m/s $< U <$ 14.87 m/s.

4.1.3 Variability of cross-shore current in HC16

The time-series data of the observed cross-shore currents, cross-shore component of wave energy flux, and water level are presented in Fig. 4.3. Fig. 4.3a shows the temporal and spatial variation of the cross-shore currents at locations of $x =$ 96, 116, 126, 161, and 191 m. The directions of the currents are indicated by the dashed line. The data below and above the dashed line refers to the shoreward and seaward currents, that is, the undertow, respectively (see more the average, standard deviation, maximum, and minimum of the undertow velocity at each considered location in Table 8.2 of Appendix. A). The blanks are missing data. The dashed blue line in Fig. 4.3b indicates averaged value of cross-shore component of wave energy flux ($\langle E_{fu} \rangle$) of 7.88 kN/s. In Fig. 4.3c, the solid gray line indicates mean water level (D.L. +0.75 m), and the dashed pink and blue lines indicate plus and minus a half of the standard deviation (W_{SD}) of 0.28 m: $W_L >$ MWL+0.5W_{SD} (0.89 m) for high-tide duration and $W_L >$ MWL+0.5W_{SD} (0.61 m) for low-tide duration.

From the HC16 observations (Fig. 4.3), it can be seen that E_{fu} was higher than the average from May 14 to 16 and May 18 to 24, and it intensified the undertow as the dominant driver. Under this high-energy wave condition, the cross-shore current velocity was seamlessly measured at nearshore locations (e.g., x = 96, 116, and 126 m). However, some data were missing owing to water bubbles at the farther locations (e.g., x = 161, 191, and 221 m), where the wave breaking points could be anticipated around x = 160 m. After May 24, the waves were calm and broken at the nearshore side of the observation array. Accordingly, the cross-shore current was subject to the change in water depth owing to the water level. A higher magnitude of undertow was periodically observed when the water level was decreasing. By contrast, the undertow was weak when the water level was rising. In addition, the spatial variation of undertow shows changes in the velocity depending on the cross-shore locations. Undertow was stronger at the nearshore (x = 96, 116, and 126 m) and offshore-sandbar (from x = 191 m) locations, while weaker undertow was observed in the trough region (x = 161 m). Hence, the undertow can be affected by either the wave energy or the change in water depth.

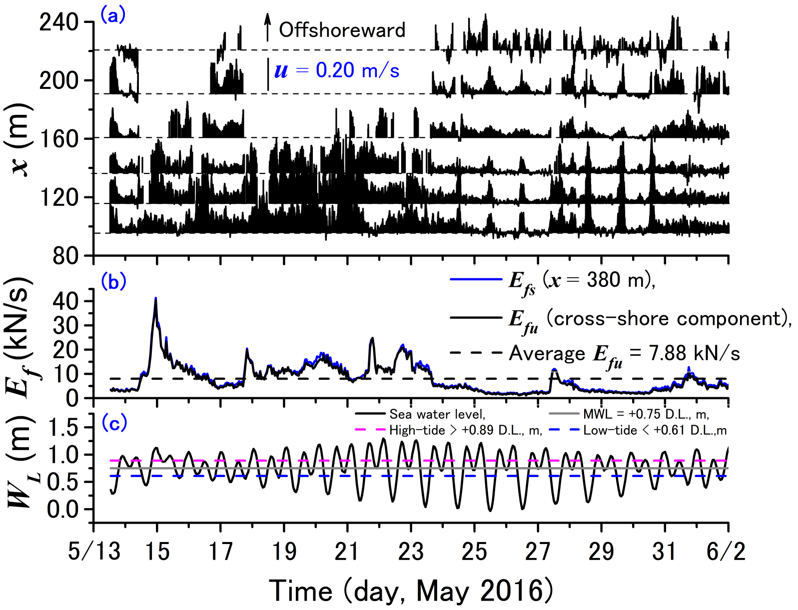

Figure 4.3: The observed time-series datasets of HC16: (a) cross-shore currents, (b) wave energy flux (blue) with a cross-shore component (black), and (c) the water level.

4.2 Data description of the field observation in May 2017 (HC17)

Not only wave processes, but also beach profile evolution is responsible for inducing nearshore currents. Thus, the difference of seabed feature in HC17 compared with HC16 should be taken into account for this analysis. The feature of the seabed profile was previously presented in Section 4.2.1. Furthermore, Section 4.5 and Section 4.2.3 will provide time-series data of wave condition and cross-shore current variability, respectively.

4.2.1 Bathymetry profile of HC17

Fig. 4.4 presents beach profiles surveyed in HC17. Each line indicates the difference of each conditional seabed profiles as already appeared in Section 4.1.1. The MWL was +0.66 m relative to the datum level at the site (Tokyo Peil -0.687 m), and the position of the shoreline was set at the still MWL. First day of the observation on May 9, a sandbar was observed at the location of x = 115 m with a water depth of 2.22 m below the MWL. This sandbar was eroded by a wave-induced longshore current during a storm event occurring from May 13 to 18, and the beach profile was then changed and had a planar slope with a highest ripple at the location of x = 190 m. The depth at this ripple was 3.36 m below the MWL. Five seaward locations of x = 116, 126, 161, 191 and 221 m (x_L/X_B = 0.57, 0.63, 0.83, 1.00 and 1.17) are discussed in the analysis. Note that X_B refers to a location nearby the highest ripple at x = 191 m.

4.2.2 Wave condition of HC17

The time-series data of wave height, wave period, and wave direction are presented in Fig. 4.5. The indication of each line is same as previously mentioned in Section 4.1. The significant wave observed at the tip of the pier was used for the analysis. The average wave height was 0.95 m with a range of 0.29 m $< H_s <$ 2.48 m, and the average wave period was 7.40 s with a range of 4.60 s $< T_s <$ 10.30 s. The wave height became larger on May 13 and then decreased after the occurring storm had disappeared on May 18. In addition, The average wind velocity was 4.52 m/s in a range of 0.17 m/s $< U <$ 12.38 m/s.

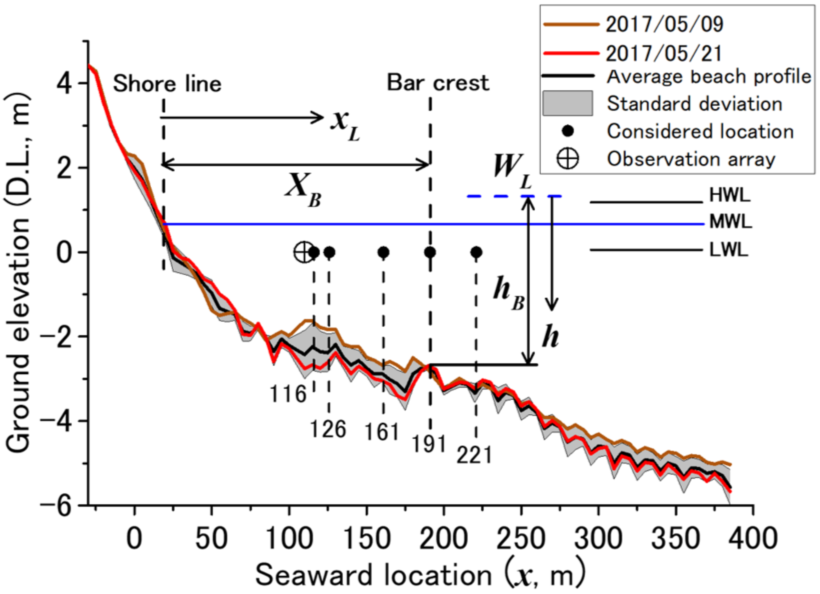

Figure 4.4: Beach profile of HC17 with average and standard deviation.

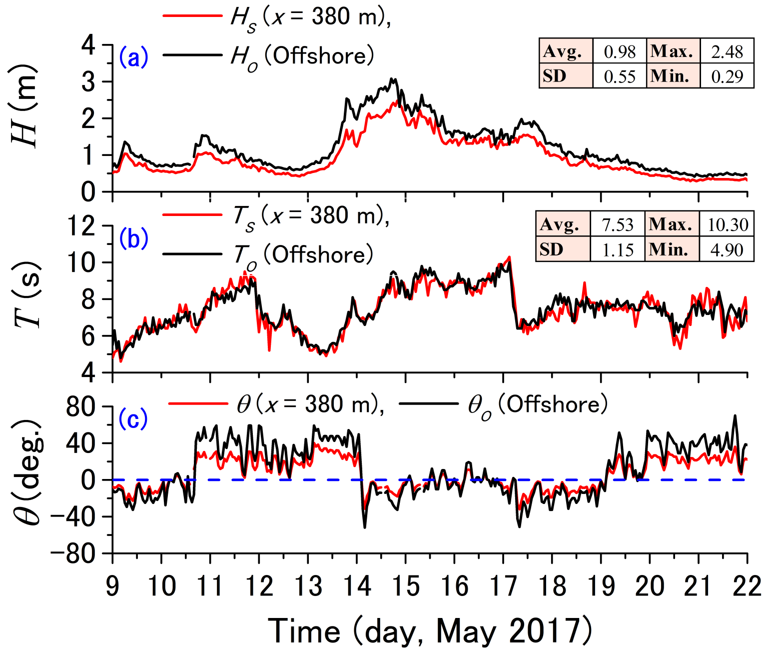

Figure 4.5: Time-series data indicating wave condition in HC17: (a) wave height, (b) wave period, and (c) wave direction.

4.2.3 Variability of cross-shore current in HC17

The time-series data of the observed cross-shore currents, cross-shore component of wave energy flux, and water level are respectively presented in Figs. 4.6a-c. The temporal and spatial variation of the cross-shore currents at locations of $x = 116$, 126, 161, 191 and 221 m were selected for the analysis (Fig. 4.6a). The undertow velocity is indicated by the vertical line above each dashed line and the missing data are the blank area (see more the average, standard deviation, maximum, and minimum of the undertow velocity at each considered location in Table 8.2 of Appendix. A). The average cross-shore component of wave energy flux of 10.00 kN/s in Fig. 4.6b is represented by the dashed blue line. In Fig. 4.6c, the solid gray line indicates mean water level (D.L. +0.66 m), and the dashed pink and blue lines indicate plus and minus a half of the standard deviation of 0.26 m: $W_L > \text{MWL}+0.5W_{SD}$ (0.79 m) for high-tide duration and $W_L > \text{MWL}+0.5W_{SD}$ (0.53 m) for low-tide duration.

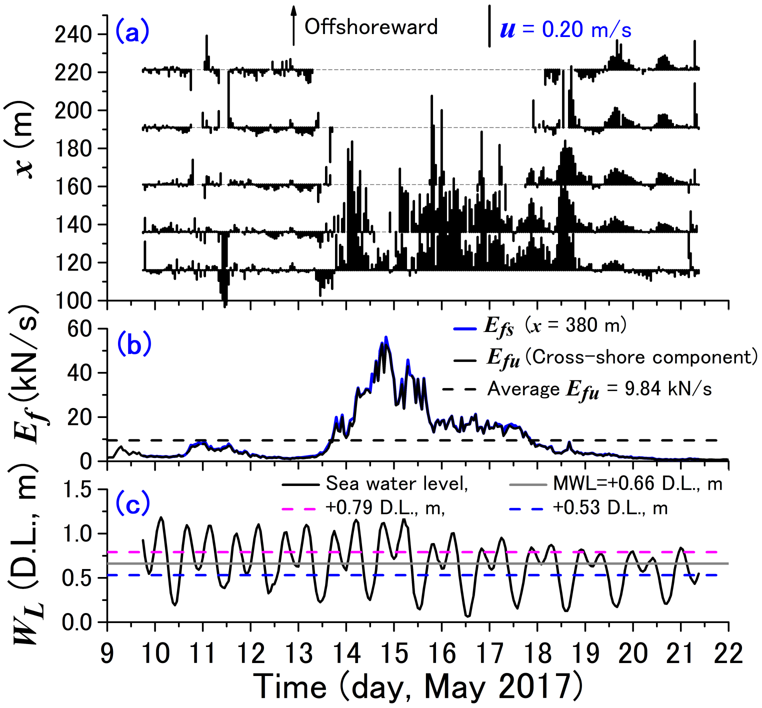

Figure 4.6: The observed time-series datasets of HC17: (a) cross-shore currents, (b) wave energy flux (blue) with a cross-shore component (black), and (c) the water level.

Form Figure 4.6, the undertow characteristics were similar to the HC16 case.

During the high-energy wave period from May 13 to 18, waves were breaking around x = 190 m, and E_{fu} was the dominant factor inducing a strong undertow. The undertow data were fully observed at x = 116, 126, 136, and 161 m, and missing data at farther locations, that is, x = 191 and 221 m. On May 18, after the storm ended, the undertow was dominated by the changes in water depth, where peak velocity of the undertow was observed during the lowest water depth periods.

Chapter 5

Statistical Analysis of Undertow

5.1 Statistical distributions of undertow current data

Undertow is significantly generated by wave energy flux (E_f) after wave breaking. When incoming waves are propagating with a small wave angle, the energy flux due to wave motion will instantly induce the strong undertow, on the other hand, the lager wave angle, the increase in longshore mass flux, and the longshore currents will be strengthened. To demonstrate the effect of wave energy flux on the undertow velocity, the energy flux needs converting to cross-shore component by wave direction. In this study, the author used the adjusted wave direction mentioned in Section 3.2.4 to calculate the cross-shore component of wave energy flux (E_{fu}).

5.1.1 Sorting the cross-shore component of wave energy flux

The overview of seabed profiles on the first and last day of the observations and considered locations of the analysis for both HC16 and HC17 is presented in Fig 5.1 by pink and blue colors respectively. The first and last day of the field observations are indicated by solid line and dashed line for each year, respectively. With respect to wave energy flux, HC17 has a wider range and a higher standard deviation of E_{fu} (0.58 kN/s $< E_{fu} <$ 51.88 kN/s and $E_{fu-SD} = 11.20$ kN/s, respectively) than those of HC16 (1.40 kN/s $< E_{fu} <$ 34.47 kN/s and $E_{fu-SD} = 5.43$ kN/s, respectively). To deal with the different ranges of wave energy between HC16 and HC17, datasets of both cases were merged and ranked from the maximum to minimum energy flux. We then sorted them into four levels (A to D), as shown in Fig. 5.2.

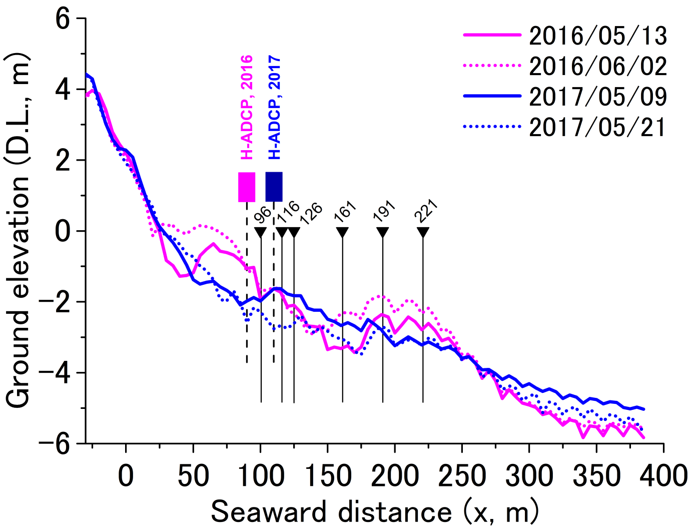

Figure 5.1: Overview of seabed profiles of HC16 and HC17.

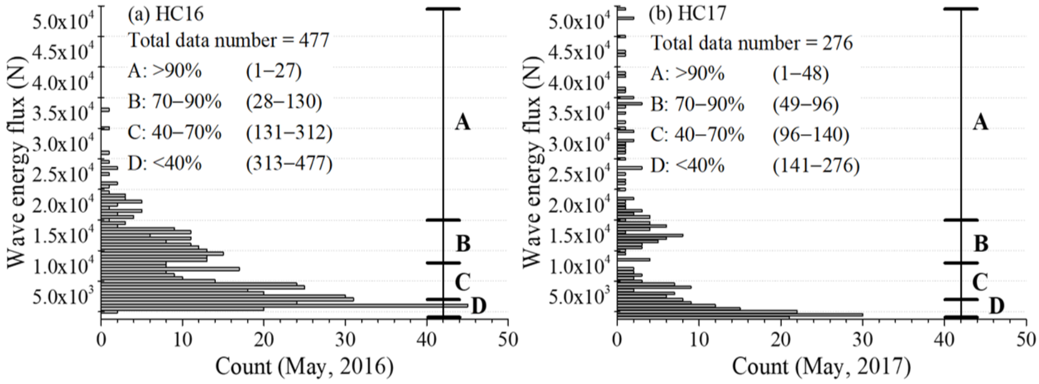

Figure 5.2: Histograms of the cross-shore component of the wave energy flux and range of each wave energy level from the highest A to the lowest D for (a) HC16 and (b) HC17.

The energy level of A is the highest rank of E_{fu} that accounted for the top 10% of all the data points. Subsequently, levels B, C, and D were assigned for lower E_{fu} ranks, which accounted for 20%, 30%, and 40% of all the data points, respectively. For each wave energy level, the average wave conditions, i.e., the average values of the wave height, wave period, and the cross-shore component of the wave energy are shown in Tables 5.1 and 5.2 for HC16 and HC17, respectively.

Table 5.1: Average wave conditions under each wave energy level for HC16.

Wave Condition	Wave energy flux level	Percentile (%)	Range of wave energy (kN)	$\langle H_s \rangle$ (m)	$\langle T_s \rangle$ (s)	$\langle E_{fx} \rangle$ (kN/s)	$\frac{\sum E_{fx}}{\int (E_{fx})_T}$ (%)
High energy wave	A	>90	$17.8 < E_{fx}$	1.80	6.90	21.77	15.8
	B	70–90	$10.7 < E_{fx} < 17.8$	1.38	6.86	13.27	36.7
Low energy wave	C	40–70	$4.4 < E_{fx} < 10.7$	1.00	7.17	7.13	34.9
	D	<40	$E_{fx} < 4.4$	0.63	7.00	2.85	12.6
Total				1.00	7.03	7.81	100

Table 5.2: Average wave conditions under each wave energy level for HC17.

Wave Condition	Wave energy flux level	Percentile (%)	Range of wave energy (kN)	$\langle H_s \rangle$ (m)	$\langle T_s \rangle$ (s)	$\langle E_{fx} \rangle$ (kN/s)	$\frac{\sum E_{fx}}{\int (E_{fx})_T}$ (%)
High energy wave	A	>90	$17.8 < E_{fx}$	1.89	8.46	30.22	53.4
	B	70–90	$10.7 < E_{fx} < 17.8$	1.37	7.98	14.50	25.6
Low energy wave	C	40–70	$4.4 < E_{fx} < 10.7$	0.94	7.65	6.45	10.5
	D	<40	$E_{fx} < 4.4$	0.54	7.00	2.10	10.5
Total				0.98	7.53	9.84	100

From Tables 5.1 and 5.2, the average wave height of energy level A was approximately triple that of energy level D for HC16, and almost four-times that for HC17, respectively. The sum of E_{fu} of levels A and B amounted to 52.5% and 79.0% for HC16 and HC17, respectively, and their average values were significantly greater than those in the entire average periods in levels C and D. Thus, the author determined the wave energy from levels A to B and C to D as the high- and low-energy wave conditions, respectively. The range between the maximum and minimum values of E_{fu} in the HC17 case was larger than that of the HC16 case.

5.1.2 Wave-energetic and spatial distributions of undertow data

In this analysis, the offshore-directed current data are determined as undertow, u_E, and the shoreward current data are ignored. To investigate the characteristics of undertow due to the effects of the wave energy flux and cross-shore locations, the undertow velocities were normalized based on the arithmetic average values of undertow measured at the first bin of H-ADCP within the entire observation period, ($\overline{u}$ = -0.10 m/s at x = 96 m for HC16 and $\overline{u}$ = -0.13 m/s at x = 116 m for HC17), that is, $u_E/\overline{u}$, were arranged according to the rank of wave energy level (Fig. 5.2). The number of undertow datasets at each seaward location, N_x, is summarized in Tables 5.3 and 5.4 for HC16 and HC17, respectively.

From Tables 5.3 and 5.4, the number of undertow data under high-energy waves (levels A and B) accounted for 27% and 35% of the total data in HC16 and HC17, respectively, and the number of data decreased towards offshore from x = 161 m and there was none at x = 221. The approximately other 70% of the total undertow data was observed under low-energy waves, and a high rate of obtaining data over 50% is presented until x = 161 m for both observations.

Table 5.3: Number of undertow data and its percentage relative to the total number in each wave energy level for and the six locations considered for HC16.

Wave Condition	Wave energy flux level	Number of 2016 undertow datasets						
		x (m)	96	106	116	126	161	191
		x_L/X_B	0.45	0.51	0.57	0.63	0.83	1.00
		N_T Total	N_{96} (%)	N_{106} (%)	N_{116} (%)	N_{126} (%)	N_{161} (%)	N_{191} (%)
High energy wave	A	27	22 (81.5)	24 (88.9)	21 (77.8)	13 (48.1)	0 (0.0)	0 (0.0)
	B	103	93 (90.3)	90 (87.4)	78 (75.7)	69 (67.0)	6 (5.8)	0 (0.0)
Low energy wave	C	182	170 (93.4)	152 (83.5)	145 (79.7)	122 (67.0)	102 (56.0)	67 (36.8)
	D	165	126 (76.4)	145 (87.9)	152 (92.1)	135 (81.8)	142 (86.0)	103 (62.4)
Total		477	411 (86.2)	411 (86.2)	396 (83.0)	339 (71.0)	395 (52.4)	170 (35.6)

Table 5.4: Number of undertow data and its percentage relative to the total number in each wave energy level for and the six locations considered for HC17.

Wave Condition	Wave energy flux level	Number of 2017 undertow datasets						
		x (m)	116	126	136	161	191	221
		x_L/X_B	0.57	0.63	0.69	0.83	1.00	1.17
		N_T Total	N_{116} (%)	N_{126} (%)	N_{136} (%)	N_{161} (%)	N_{191} (%)	N_{221} (%)
High energy wave	A	48	44 (91.7)	46 (95.8)	40 (83.3)	4 (8.3)	0 (0.0)	0 (0.0)
	B	48	47 (97.9)	47 (97.9)	46 (95.8)	14 (29.2)	2 (4.2)	0 (0.0)
Low energy wave	C	44	29 (65.9)	29 (65.9)	33 (75.0)	31 (70.5)	18 (40.9)	6 (13.6)
	D	136	58 (42.6)	83 (61.0)	93 (68.4)	79 (58.1)	62 (45.6)	60 (44.1)
Total		276	178 (64.5)	205 (74.3)	212 (76.8)	128 (46.4)	82 (29.7)	66 (23.9)

The histograms in Figs. 5.3 and 5.4 illustrate the number of undertow data separated at each wave energy level and cross-shore location, which are based on Tables 5.3 and 5.4. In each panel, the horizontal dotted line indicates the average of the normalized undertow, with the value and percentage of undertow data (N_x/N_T) are presented in the upper box. The average values of normalized undertow in each panel are noted in the upper box and indicated by the horizontal dotted line. In this study, at locations where more than 50% of data was recorded (shown with gray area) were included in the analysis. Because the offshore bar location at $x = 191$ m played a key role in wave breaking and induced a strong undertow, the author also included the datasets at this location into the discussion for both cases despite being smaller than 50% (36.8% and 40.9% for HC16 and HC17, respectively).

From the histogram for HC16 (Fig. 5.3), the number of recorded undertow data at energy levels C and D is large for a lower normalized undertow, and the values are conglomerated near to or less than average. When the wave energy increases to levels B and A, the data show more spread toward a higher value of normalized undertow, and surpass their average. This data distribution based on wave energy is defined as a 'wave-energetic distribution.'With respect to the cross-shore location, the number of data and the data acquisition rate tend to decrease seaward, whereas the average normalized undertow increases near the bar regions at $x = 96$, 116, and

191 m compared to the lower average value near the trough region at x = 126 and 161 m. Here, the data distribution was considered along the cross-shore locations, which is called a ‘spatial distribution.’

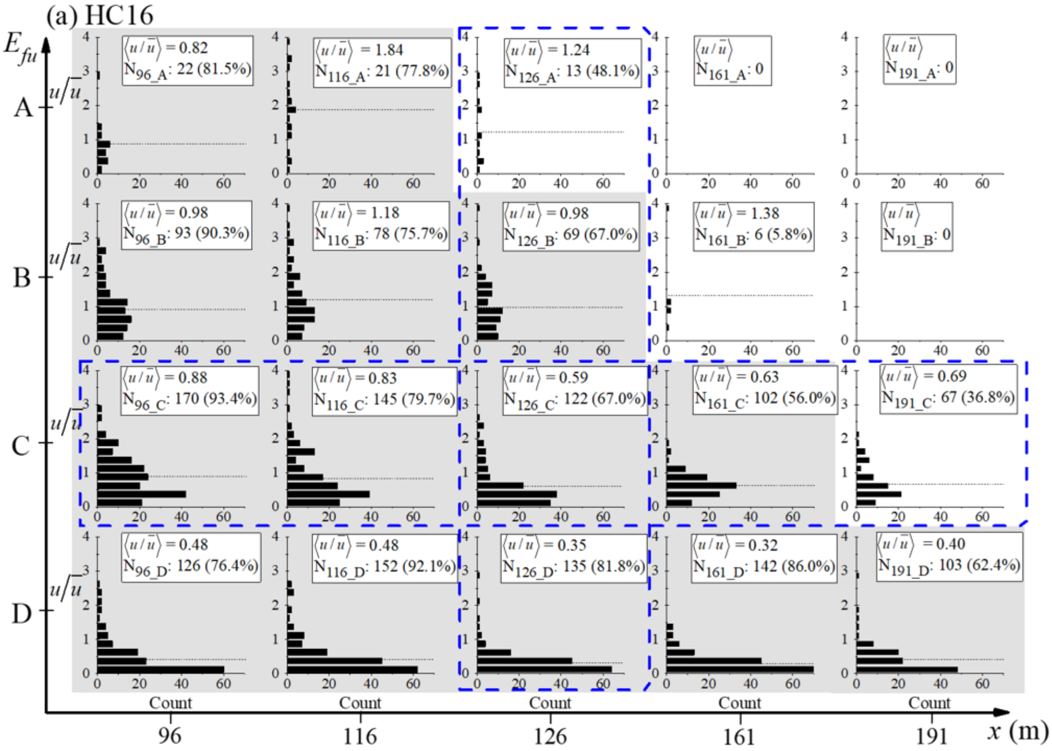

Figure 5.3: Wave-energetic and spatial distributions of histograms of undertow datasets for HC16.

According to HC17 (Fig. 5.4), the number of undertow data at energy level A spreading out toward a higher normalized value is greater than that of HC16. This means that the wave energy at level A in HC17 is higher than that of HC16. However, the number of data at level A is smaller than that of level B for the same case because the H-ADCP was installed on the crest of the small sandbar at x = 110 m at the beginning of the observation (Fig. 4.4), during which wave breaking occurred at more nearshore location. Thus, the H-ADCP could not observe the current data during that period of energy level A. After May 10, the small sandbar moved towards offshore, and the waves were then broken in front of the H-ADCP position, resulting in more data being obtained during the period of energy level B. For the same reason, the averages of the normalized undertow at energy level B at the nearshore locations of x = 116 and 126 m are higher than those of level

A. The wave-energetic and spatial distribution of datasets were then analyzed using the exceedance probability method.

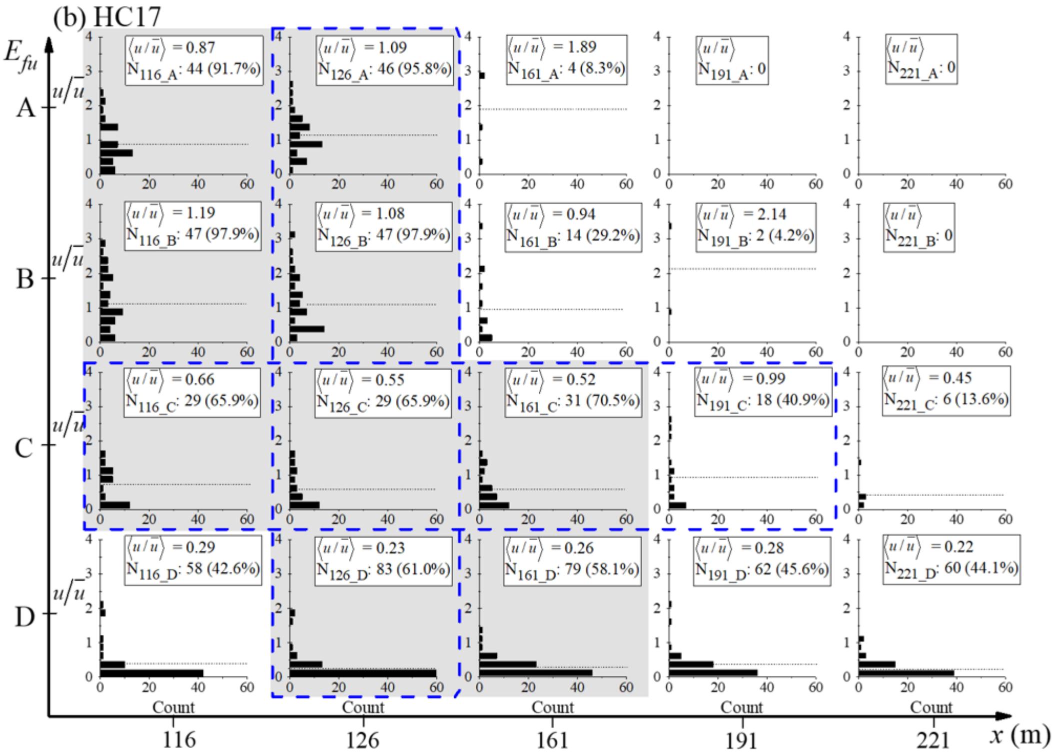

Figure 5.4: Wave-energetic and spatial distributions of histograms of undertow datasets for HC17.

5.2 Exceedance probability analysis for undertow

The wave-energetic and spatial distributions of undertow datasets have already been discussed in Chapter 3. In this Section, the spatial-energetic distributions of undertow exceedance probability is considered. The effects of high-wave-energy flux and small water depth over a bar region result in the increase of undertow intensity. This means the wave energy flux, water depth, and cross-shore location are three main hydrodynamic parameters that induce undertow. The combination of these three parameters develops an efficiency of undertow n_e that can be used for estimating Weibull parameters to predict the exceedance probability of undertow. Therefore, we have obtained a new statistical model that will be explained in details in subsection 5.4. The comparison of the observed and modeled exceedance probability of undertow is demonstrated in later to ensure the accuracy of the model.

5.2.1 Undertow exceedance probability of HC16

First, the examples of observed and Weibull distributions of exceedance probability of the normalized undertow are presented in Fig. 5.5 to demonstrate the process of defining the wave-energetic and spatial distributions of undertow. The vertical dashed line refers to $u_E/\overline{u}$ = 1.0 (u_E = -0.10 m/s). A discussion relating to well-fitting curves of the Weibull distribution has been given in the Section 3.3. Secondly, all findings of the exceedance probability analysis for every energy level and seaward locations are discussed. Fig. 5.5a presents the energetic distributions of the undertow exceedance probability for all wave energy levels at x = 116 m (x_L/X_B = 0.57). Each color indicates a different wave energy level (A, B, C, or D). For each level, exceedance probability decreases with an increase in the normalized undertow. The undertow velocity is less able to reach a higher extreme value, i.e., a comparison between the values at higher criteria of $u_E/\overline{u}$ = 2.0 and lower criteria of $u_E/\overline{u}$ = 0.5. When the wave energy flux level becomes higher (from D to A), its exceedance probability increases.

Fig. 5.5b shows the spatial distributions of the undertow exceedance probability for cross-shore locations at wave energy level of C. Each location is indicated by each color. For the normalized undertow at a bound of $u_E/\overline{u} > 1.0$, the undertow exceedance probability decreased when it was observed at locations farther offshore, and the lowest value was at x = 161 m (tough region), but exceedance probability increased slightly at x = 191 m (outer bar region). This is because the undertow is affected by the various water depths at the different locations. A shorter depth owing to alongshore sandbars induces a stronger undertow, as observed at locations of x = 96 and 191 m.

Although some variances between the curves are bigger for a higher criterion, the exceedance probability curve of all locations was similar to each other. Exceedance probability at the wave energy levels of A, B, and D also had a similar trend. The findings indicate that the exceedance probability of the undertow tends to be affected by the seaward spatial variability in addition to the fluctuation of the wave energy flux. The energetic distributions of undertow exceedance probability for all locations; x = 96, 116, 126, 161 and 191 m are included in Fig. 5.6 and the spatial distributions of undertow exceedance probability for every level of wave energy; A, B, C and D are gathered in Fig. 5.7.

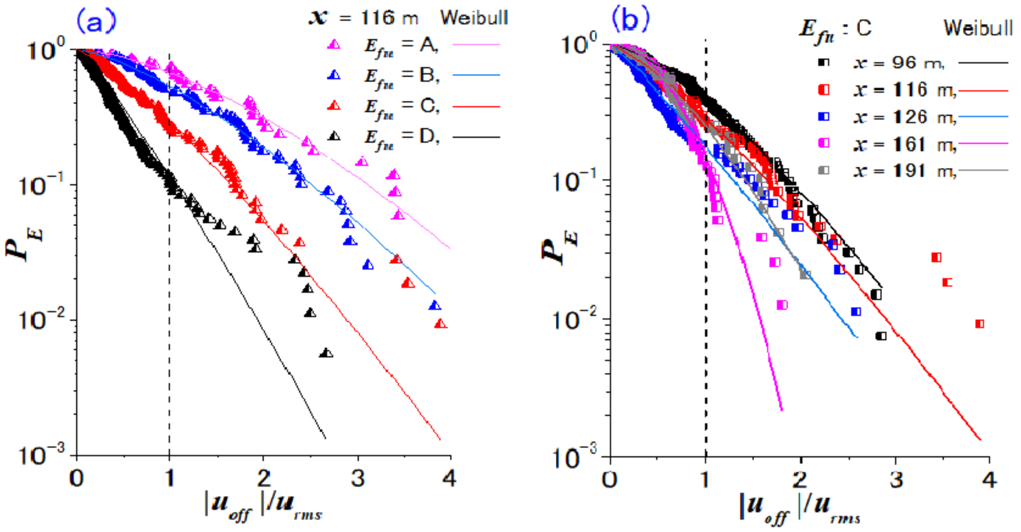

Figure 5.5: Exceedance probability of observed and Weibull distributions applicable to normalized undertow for HC16: (a) location of x = 116 m for each wave energy level and (b) wave energy level of C for each considered location.

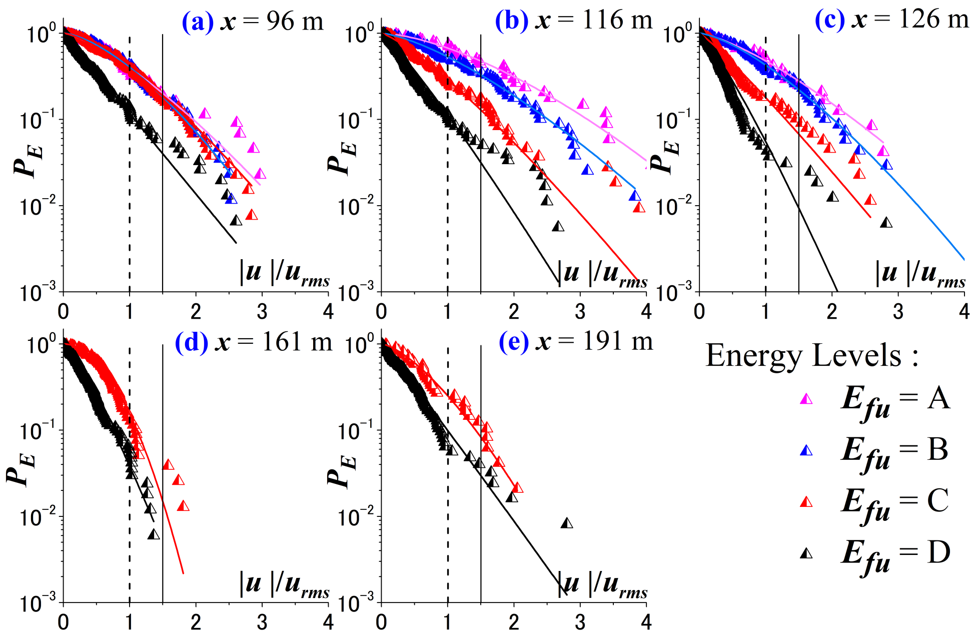

Figure 5.6: Wave-energetic distribution of the exceedance probability of observed and Weibull distributions applicable to normalized undertow for locations of: (a) x = 96 m, (b) x = 116 m, (c) x = 126 m, (d) x = 161 m and (e) x = 191 m in HC16.

From Fig. 5.6, the illustration of wave-energetic distributions of undertow exceedance probability are presented for all considered locations. Not only the location of $x = 116$ m demonstrates that the increase in wave energy flux resulted in the higher exceedance probability of undertow, but also the other locations similarly happened and had the same trend even there was no data at energy levels of A and B on the farther locations of $x = 161$ and 191 m. With regards to the location of $x =$ 96 m where the undertow exceedance probability for energy levels of A, B and C was identical, this can also be explained that the short distance of water depth at this point forces the undertow intensity instead of wave energy in during the decreasing in wave energy level.

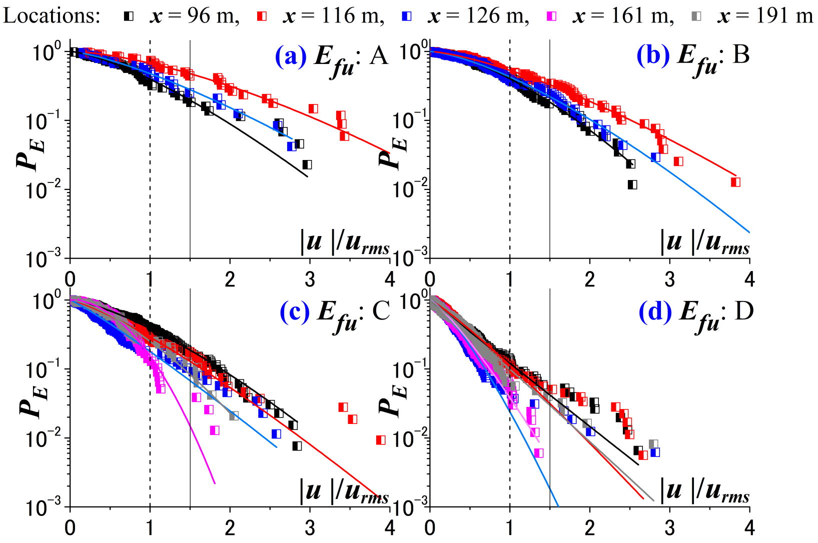

Figure 5.7: Spatial distribution of the exceedance probability of observed and Weibull distributions applicable to normalized undertow for energy levels of: (a) $E_{fu} =$ A, (b) $E_{fu} =$ B, (c) $E_{fu} =$ C, and (d) $E_{fu} =$ D in HC16.

Fig. 5.7 illustrates the effect of water depth at each seaward location on the undertow exceedance probability. The curves are slight different for all energy levels. However, the curve of undertow exceedance probability at the location of $x = 161$ m in Figs. 5.7c-d (low-energy-wave condition) can be seen the effect of water depth at trough region that less generated undertow compared to other positions where bars existed (e.g. $x = 96$ and 191 m). In the other hands, it can be concluded that the closer to nearshore location, the undertow is strengthened by water depth, and it becomes weaker at farther location and weakest at trough location.

From the results, the measured exceedance probability of undertow can well be estimated by using Weibull distribution as two reasons mentioned in following;

1) Relating to Fig. 5.5, exceedance probability of observed and Weibull distributions applicable to normalized undertow and exceedance probability were plotted in log-scale. The scatter of data can be seen from $u_E/\overline{u} > 1.5$. However, the scattering only ranges from exceedance probability = 0.001-0.3 (0.1%-3%) and small number data were counted compared to the data that well fitted by Weibull distribution when $u_E/\overline{u} \leq 1.5$.

2) The relationship between the observed and results from Weibull distribution gives good correlation with the skill of 0.96.

5.2.2 Undertow exceedance probability of HC17

In the previous section, the undertow exceedance probability under barred beach condition was considered. Here, the analysis is extended to cover a natural unbarred beach condition as mentioned in Section 4.2 that the seabed profile was approximately planar. To develop the statistical model, the undertow observation of HC17 was also included in this analysis.

The wave-energetic distributions of the exceedance probability of observed and Weibull distributions applicable to normalized undertow for all considered locations are demonstrated in Fig. 5.8. For the curve indicating the undertow exceedance probability at energy level of A, it should have the highest exceedance probability as anticipated owing to the highest level, but the lower exceedance probability than that of levels B ans C is appeared. This can be explained that H-ADCP was measuring the onshore ward currents and waves were broken after passing H-ADCP during the initial state of the storm event. After that, a sand ripple was generated in front of H-ADCP and the undertow was then more observed during the middle of storm event responsible for the lower energy levels of B, C and D. Accordingly, the exceedance probability of undertow was highest at energy level of B and became lower when wave energy was decreasing. The disappeared curve in Figs. 5.8c-d means no undertow data. The farther seaward location, the less number of undertow data.

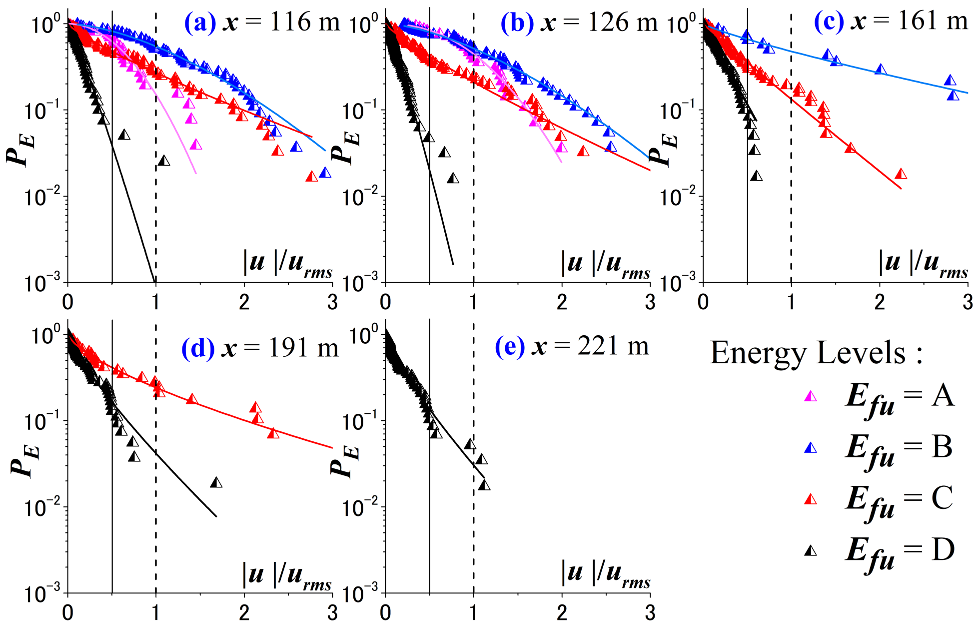

Figure 5.8: Energetic distributions of the observed undertow P_E, and Weibull distributions applicable to normalized undertow for HC17 at the locations of: (a) x = 116 m, (b) x = 126 m, (c) x = 161 m, (d) x = 191 m and (e) x = 221 m.

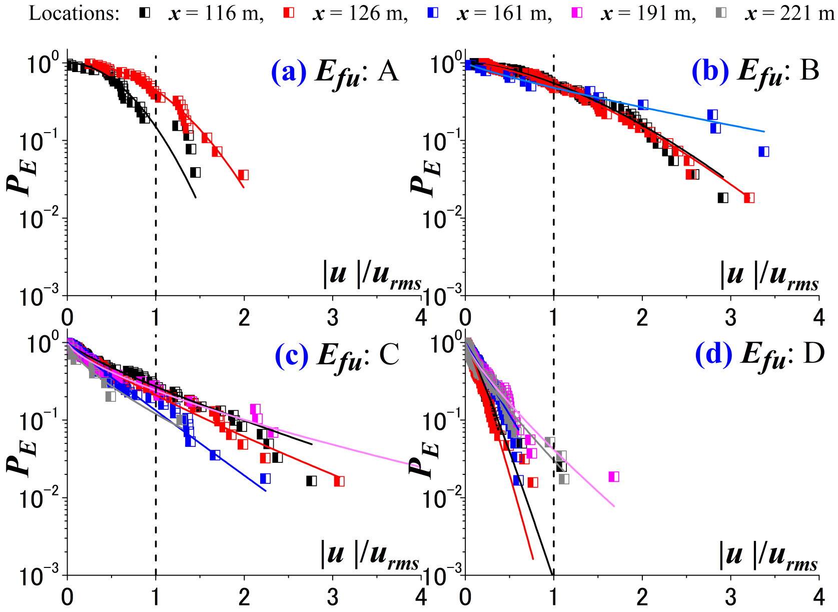

Figure 5.9: Spatial distribution of the observed undertow P_E, and Weibull distributions applicable to normalized undertow for HC17 at the energy levels of: (a) E_{fu} = A, (b) E_{fu} = B, (c) E_{fu} = C, and (d) E_{fu} = D.

In addition to energetic distribution, the spatial distribution of undertow exceedance probability at each energy level is illustrated. In Figure 5.8, the dashed line refers to the normalized undertow at the criteria of 1.0. The curves in each panel show similar trends for every location. This is same as the discussion of 2106 undertow data in Section 5.6. The energy level of B and C could lead to the stronger undertow and reach the higher extreme undertow compared with that of level A. The exceedance probability was lowest at energy level of D compared to other levels as it had the negative steepest slope. The highest exceedance probability for the energy level D was at the ripple location of $x = 191$ m.

5.3 Results of exceedance probability analysis

The correlation between the observed P_E and the normalized value of the undertow was determined to understand the undertow characteristics. The analysis presented here separately demonstrates the distributions of the observed undertow P_E, which is affected by the wave energy, cross-shore locations, and different water depths owing to the tidal range. The Weibull distribution was used to fit the observed undertow P_E, providing two values of parameters a and b individually for each curve of undertow P_E. These two Weibull parameters allow us to develop a new model of the undertow P_E, as described in Section 5.4.

5.3.1 Effect of wave energy flux

First, the wave-energetic distributions of undertow P_E at $x = 126$ m ($x_L/X_B = 0.63$), which have approximately 50% the number of data at all wave energy levels (as identified by the meshed box in Figs. 5.3 and 5.4), were chosen to demonstrate the characteristics of the undertow owing to the wave energy effect. Figures 5.10a and 5.10b depict the observed and Weibull-fitted P_E of the normalized undertow for HC16 and HC17, respectively. The different symbols, i.e., black rectangle, open gray circle, blue triangle, and gray rectangle indicate the undertow PE distribution at wave energy levels of A, B, C, and D, respectively. Each curve decreases with an increase in the normalized undertow value. Undertow P_E is less able to reach a more extreme value of $u_E/\overline{u}$, e.g., a comparison of undertow P_E at each energy level between the higher criteria of $u_E/\overline{u} = 1.0$ and lower criteria of $u_E/\overline{u} = 0.5$.

However, Fig. 5.10a of HC16 shows that when the wave energy flux level becomes higher from D to A, its P_E increases and reaches the higher criteria of approximately $u_E/\overline{u} = 3.0$ for the energy level of A. For HC17 (Fig. 5.10b), a slightly lower undertow

P_E occurred at level A than at level B, i.e., from $u_E/\overline{u} = 1.3$, and the curve of wave energy level B was able to reach the criterion of $u_E/\overline{u} = 3.0$ unlike level A. This was caused by the sandbar movement during the field observation of HC17 described in Section 5.1.2. Note that a similar trend of wave-energetic distributions was also illustrated at other locations of $x = 96$, 116, and 161 m for HC16 and $x = 116$ and 161 m for HC17.

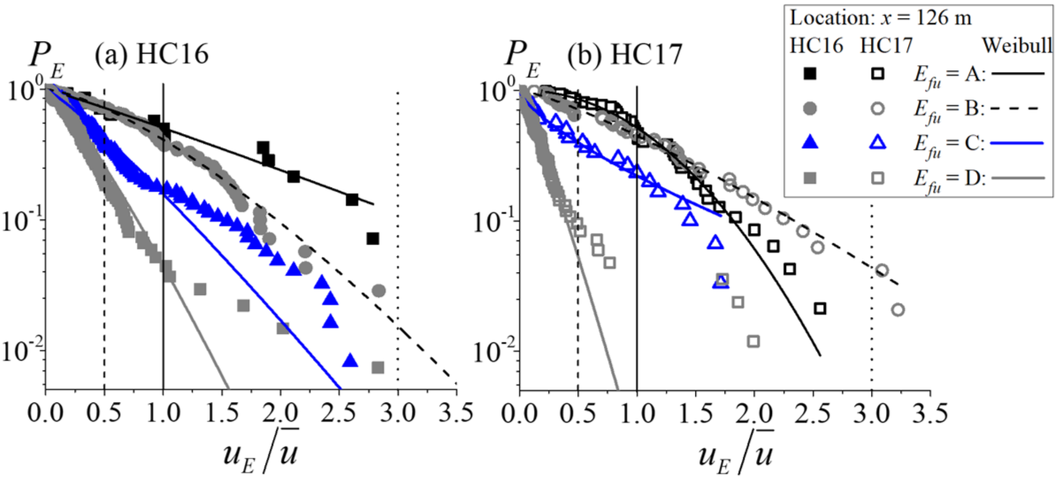

Figure 5.10: Wave-energetic distributions of the undertow P_E of observed and Weibull distributions applicable to normalized undertow at the location of $x = 126$ m for (a) HC16 and (b) HC17. The black rectangle, gray circle, blue triangle, and gray rectangle differentiate the undertow datasets at wave energy levels of A, B, C, and D, respectively. The solid and open symbols represent the observed undertow P_E for HC16 and HC17, respectively. The vertical dashed, rigid, and dotted lines refer to the criteria of normalized undertow at $u_E/\overline{u} = 0.5$, 1.0, and 3.0, respectively.

5.3.2 Effect of cross-shore location and water depth

Although wave energy flux is the main driver for the undertow, the bathymetry feature can also affect the magnitude of the undertow, particularly during LWE conditions. To demonstrate the effect of the bathymetry feature on the undertow characteristics, the spatial distributions of the undertow P_E for cross-shore locations at a wave energy level of C (as identified by the dashed box in Figs. 5.3 and 5.4 are illustrated in Figs. 5.11a and 5.11b for HC16 and HC17, respectively. Each location is indicated by a different color and symbol. Both cases represent a similar trend of undertow P_E curves for all considered locations until the criterion $u_E/\overline{u} = 1.0$. The difference of the P_E curves becomes larger from approximately $u_E/\overline{u} > 1.0$.

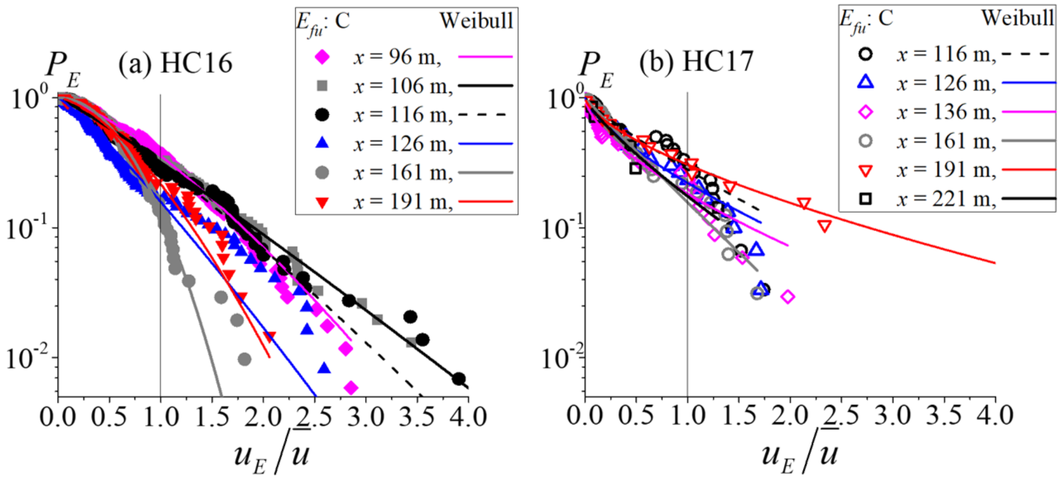

Figure 5.11: Spatial distributions of the undertow P_E of observed and Weibull distributions applicable to normalized undertow at the energy level of C for (a) HC16 and (b) HC17. The solid and open symbols represent the observed undertow P_E for HC16 and HC17, respectively. The blue triangle indicates the undertow datasets at wave energy levels of C at the location of $x = 126$ m (the same as in Figs. 5.3 and 5.4). The red upside-down triangle represents the undertow P_E, which increases at $x = 191$ m (bar region). The rigid line refers to the criterion of the normalized undertow at $u_E/\overline{u} = 1.0$.

Figure 5.11a illustrates that the undertow P_E decreased with the farther offshore locations, and the lowest value was at $x = 161$ m (trough region), whereas P_E increased again at $x = 191$ m (outer bar region). This change in the undertow P_E along the cross-shore locations occurred because the undertow was affected by the various water depths owing to the bathymetry feature. A shorter depth owing to alongshore sandbars induces a stronger undertow, as observed at locations of $x =$ 96 and 191 m.

By contrast, the planar beach condition of HC17 in Fig. 5.11b presents a similar curve of the spatial distributions of the undertow P_E for all considered locations. Interestingly, its highest P_E is at $x = 191$ m, where a small sand bar exists. Note that the distribution of undertow P_E at the wave energy level of D also had a similar trend for both cases of HC16 and HC17. Therefore, the features of the barred and planar beaches can cause different undertow characteristics under low-wave-energy conditions. The undertow can be induced around the bar region, which has a short water depth.

5.4 Modeling for undertow exceedance probability

One of our primary objectives is to develop the statistical model of the undertow. When applying the Weibull distribution to each observed undertow P_E curve, the curves are well fitted by changing the two Weibull parameters. According to the findings presented in the previous section, these two parameters are affected by the normalized values of the wave energy flux, relative cross-shore location, and normalized water depth. A higher wave energy flux generates a stronger undertow. In addition, the characteristics of the undertow can also be inversely differentiated by the cross-shore location and water depth, that is, the farther the location is from the shore with greater water depth, the weaker the undertow.

The relation between the Weibull parameters and the combination of normalized statistical values (hereafter n_e, the efficiency of the undertow) is then defined to generalize the Weibull distribution for undertow P_E. The normalized parametric values are defined as $\langle E_{fu}\rangle_O \,/\, \langle E_{fu}\rangle_T$ for cross-shore component of wave energy flux, $\langle x_L/X_B\rangle$ for cross-shore location, and $\langle h\rangle_O \,/\, \langle h_B\rangle_T$ for water depth. The most suitable combination of all trials when considering the Weibull distribution is

$$n_e \;=\; \frac{[\langle E_{fu}\rangle_O \,/\, \langle E_{fu}\rangle_T]}{[\langle x_L/X_B\rangle][\langle h\rangle_O \,/\, \langle h_B\rangle_T]} \tag{5.1}$$

where subscript O is the observed dataset of each wave energy level of each cross-shore location, T is the total observed dataset, and angle brackets represent the averaging procedure. Curve fitting methods for nonlinear and linear regression were applied to the relationship between the two Weibull parameters and n_e, as indicated in Fig 5.12 (see more the values of parameter n_e in Appendix. B, and the values of scale a and shape b parameters in Appendix. C).

Besides the polynomial function, the other functions, e.g. exponential, logarithm, and allometric functions had already been considered for scale parameter a. The explanation is separately given in Appendix. D.

The data for parameter a for energy levels A, B, C, and D are represented by a black rectangle, open circle, blue triangle, and gray rectangle, respectively. The shape parameter b is indicated by the rhombus. The solid and open symbols indicate the HC16 and HC17 datasets, respectively. It can be considered that the value of parameter a decreases with an increase in n_e from energy level D to C, and increases from energy level B to A. This trend supports our discussion that the shorter water depth under low-energy waves and the increase in wave energy under high-energy waves can increase the value of parameter a, which enlarges the P_E of the undertow.

The shape parameter b presents a linear relation with n_e. Therefore, the best fits of the scale parameter a and shape parameter b are as follows:

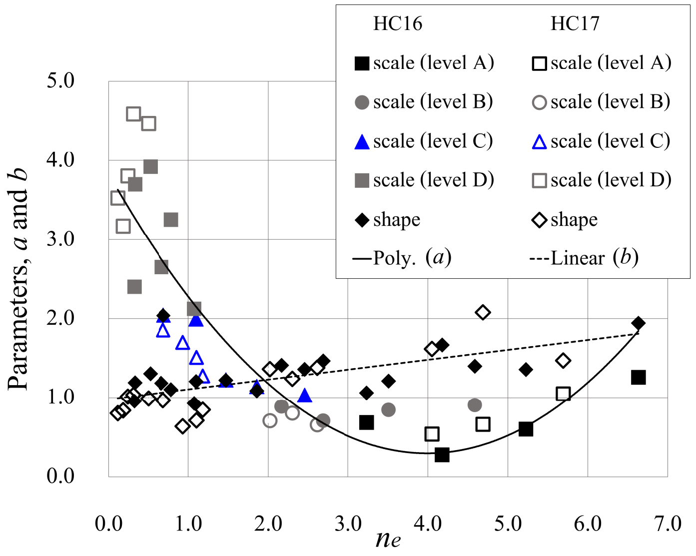

Figure 5.12: Correlation between n_e and two Weibull parameters (scale a and shape b). The scale parameter a obtained at wave energy levels of A, B, C, and D were differentiated by the black rectangle, gray circle, blue triangle, and gray rectangle, respectively. The shape parameter b was indicated by the rhombus. The HC16 and HC17 datasets were distinguished by using the solid and open symbols, respectively. The rigid and dashed lines represent the fit functions for parameters a and b, respectively.

$$a = 0.22n_e^2 - 1.77n_e + 3.83, \tag{5.2}$$

$$b = 0.13n_e + 0.98 \tag{5.3}$$

with the skill of regression coefficients of $R^2 = 0.80$ and 0.42, respectively.

The accuracy of the proposed statistical model against the observed and the Weibull distribution is demonstrated for every energy level and considered location. Fig. 5.13 shows an example of the comparison of the modeled and observed result at the location of $x = 96$ m. The modeled P_E by our proposed model is represented by the solid curve with yellow dot indicating the P_E value. Although the modeled curve does not perfectly fit the observed; however, the deficiency was only about

0.03 (3%) at the $u_E/\overline{u} = 1.5$. Moreover, the comparison result reveals that the higher undertow P_E (lower $u_E/\overline{u}$ value) was well estimated.

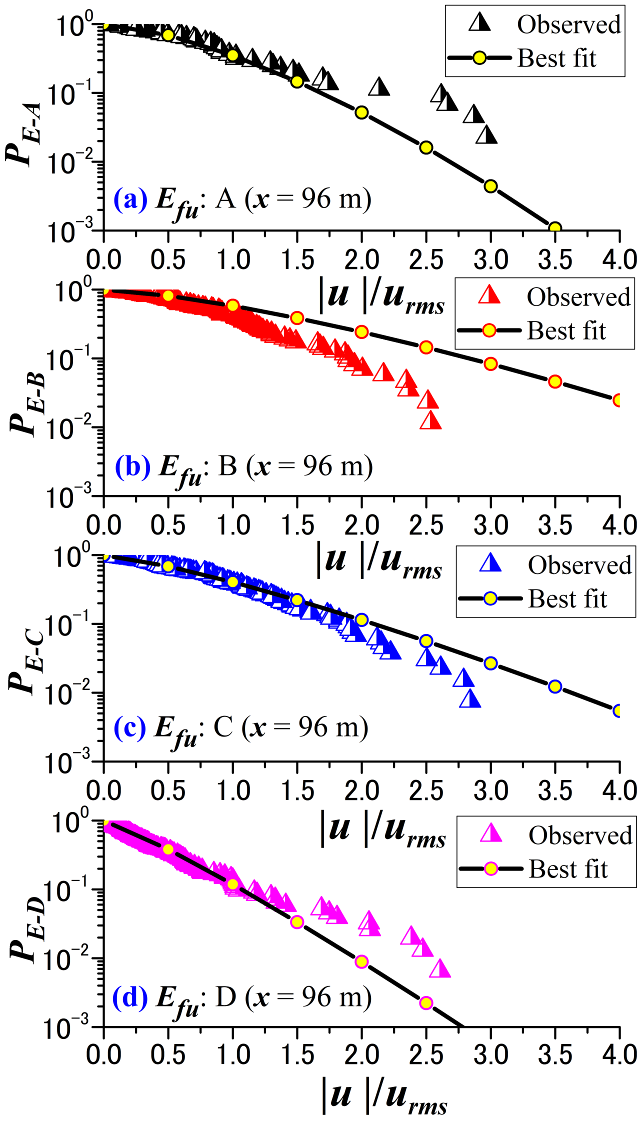

Figure 5.13: Comparison of wave-energetic distribution between the observed and modeled undertow P_E at location x = 96 m.

Also, the efficacy of our proposed model must be ensured on an extreme current of approximately $u_E/\overline{u} = 0.10$, which is five-times larger than the sediment-fall velocity (0.02 m/s [20]) for a sediment size of 0.18 mm along the Hasaki coast.

Figures 5.14a and 5.14b illustrate a comparison of the undertow P_E of the observed (black), Weibull distribution (gray), and “best-fit” (red) models for HC16 and HC17, respectively.

Our findings demonstrate that the best-fit model can properly predict P_E under both bathymetry conditions for either a barred or planar beach. The spatial distributions of the undertow for both cases of HC16 and HC17 reveal a high P_E at the high-energy levels of A and B and a low P_E at the low-energy levels of C and D. During the high-energy level A of HC16 (Fig. 5.14a(i)), the observed P_E tended to increase based on the wave energy flux at the nearshore locations from x = 96 to 116 m. However, P_E decreased at x = 126 m, which was closer to the greater water depth around the trough region.

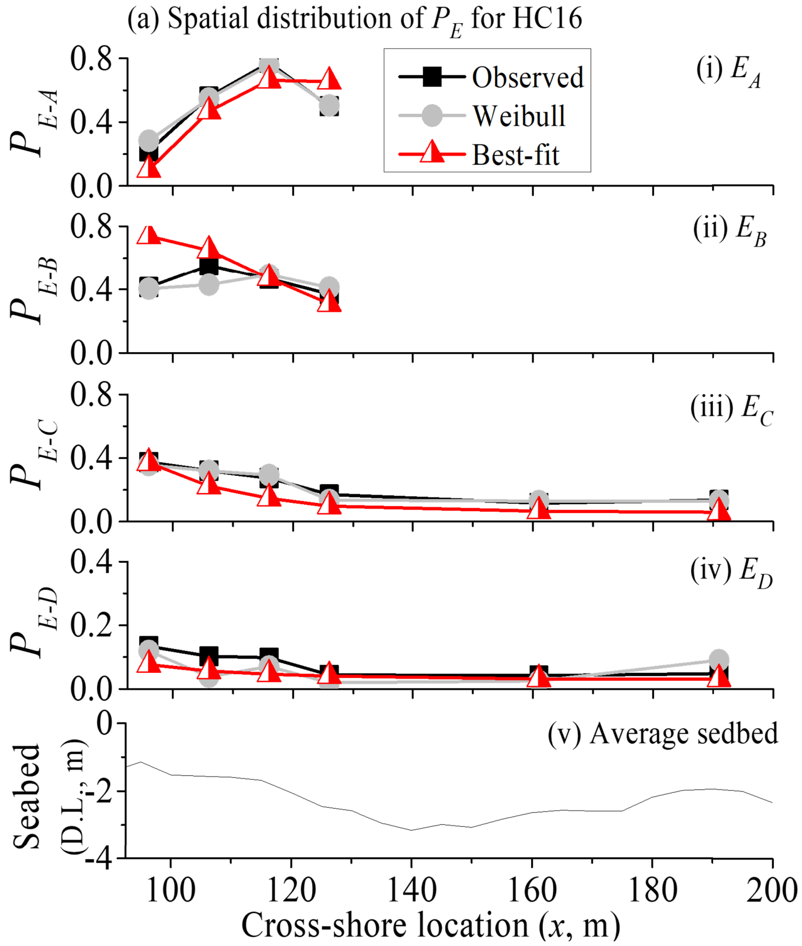

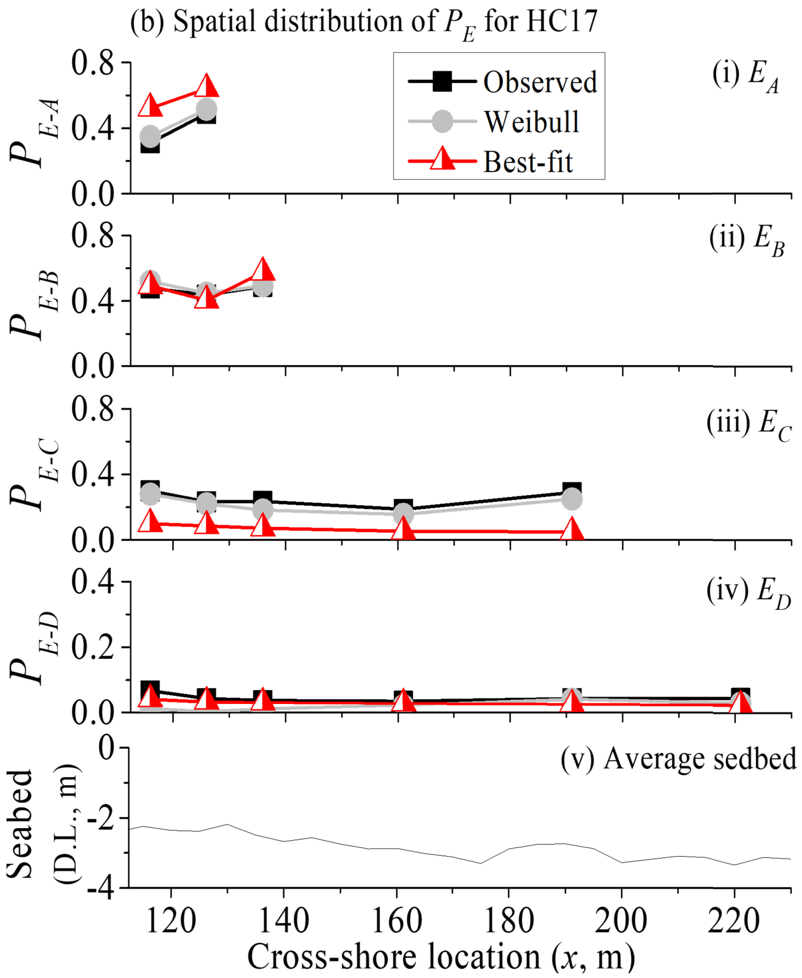

Figure 5.14: Spatial distributions of undertow P_E under the criterion of $u_E/\overline{u} = 0.10$ for (a) HC16 and (b) HC17. Panels (i)–(iv) show the results from energy levels A–D, respectively. The observed, Weibull, and best-fit model P_E were represented by a black rectangle, gray circle, and half-red filled triangle, respectively. Panel (v) illustrates the average seabed profile.

Considering low-energy waves (e.g., Fig. 5.14a(iii, iv) and Fig. 5.14b(iii, iv)), the undertow was subject to bathymetry features, that is, cross-shore location and water depth, because the observed and Weibull distribution of undertow P_E seemed similar to the characteristic of their bed profiles. Particularly at the energy level of C in HC16, P_E was the highest at a shorter water depth near the inner sandbar at x = 96 m and reduced along the seaward direction until it became the lowest within the trough region at x = 161 m. It then increased again at the outer bar at x =

191 m owing to the effect of the shorter water depth. This supports the results of a laboratory experiment [31, 44]m, where the lowest and highest undertow velocities were at the trough and bar, respectively.

In addition to the illustration of the spatial distributions, the probability percentage of undertow that exceed the certain velocity of $u_E = 0.10$ m/s is determined in Table 5.5. As already explained, the percentage of undertow exceedance probability from different three types of data are mentioned: the measured, Weibull distribution and best-fit model. At each wave energy level, the percentages of all types of data are slightly different from each others at the same location and the largest errors are on the location of $x = 96$ m of energy level B that shows the discrepancy of overestimation about 20.8% and 22.6% compared with the measured and Weibull distribution, respectively. However, The averages of modeled exceedance probability using the best-fit model are approximately 0.7 - 3.2% and 0.4 - 6.3% different from the results of measured and Weibull distribution, respectively.

Table 5.5: Percentage of undertow probability exceeding u_E = -0.10 m/s ($u_E/\overline{u}$ = 1.0) for HC16.

Location (m)	Percantage of exceedance probability at an extreme undertow of 0.10 m/s (2016)											
	Energy level A			Energy level B			Energy level C			Energy level D		
	Observed	Weibull	Best fit	Observed	Weibull	Best fit	Observed	Weibull	Best fit	Observed	Weibull	Best fit
96	31.82	39.65	34.03	41.86	40.09	62.67	38.64	38.60	41.26	13.73	11.71	14.66
106	53.49	50.02	57.93	49.41	46.10	54.55	26.72	34.54	28.12	9.94	8.62	10.76
116	67.65	67.30	62.43	49.37	53.26	39.92	25.00	28.88	20.42	10.61	11.27	9.31
126	50.00	47.71	51.77	33.33	42.66	29.81	15.91	17.91	14.55	4.94	5.51	7.89
161	-	-	-	-	-	-	10.26	15.44	9.52	5.99	3.83	6.19
191	-	-	-	-	-	-	25.00	25.08	8.81	5.65	9.92	6.16
Average	50.74	51.17	51.54	43.49	45.53	46.74	23.59	26.74	20.45	8.48	8.47	9.16

Moreover, the probability percentage of undertow that exceed the certain velocity of u_E = -0.13 m/s is indicated in Table 5.6. Similarly, the percentage of undertow exceedance probability from different three types of data are mentioned: the measured, Weibull distribution and best-fit model. Note that the number of observed undertow data in 2017 is less than 2016. At each wave energy level, the percentages of all types of data are analogous to the others at the same location and the largest errors are on the location of $x = 126$ m of energy level A that shows the discrepancy of about 10.0% and 12.6% compared with the measured and Weibull distribution, respectively. However, The averages of modeled exceedance probability using the best-fit model are approximately 1.6 - 5.7% and 2.2 - 10.0% different from the results of measured and Weibull distribution, respectively.

Table 5.6: Percentage of undertow probability exceeding u_E = -0.13 m/s ($u_E/\overline{u}$ = 1.0) for HC17.

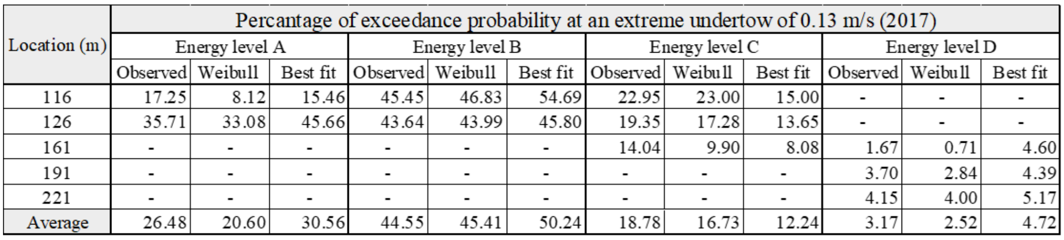

Location (m)	Percantage of exceedance probability at an extreme undertow of 0.13 m/s (2017)											
	Energy level A			Energy level B			Energy level C			Energy level D		
	Observed	Weibull	Best fit	Observed	Weibull	Best fit	Observed	Weibull	Best fit	Observed	Weibull	Best fit
116	17.25	8.12	15.46	45.45	46.83	54.69	22.95	23.00	15.00	-	-	-
126	35.71	33.08	45.66	43.64	43.99	45.80	19.35	17.28	13.65	-	-	-
161	-	-	-	-	-	-	14.04	9.90	8.08	1.67	0.71	4.60
191	-	-	-	-	-	-	-	-	-	3.70	2.84	4.39
221	-	-	-	-	-	-	-	-	-	4.15	4.00	5.17
Average	26.48	20.60	30.56	44.55	45.41	50.24	18.78	16.73	12.24	3.17	2.52	4.72

The comparison between observed and modeled undertow exceedance probability for both of HC16 and HC17 are presented in Fig. **??**. Although the spatial distribution of undertow P_E contained a small difference at x = 96 m in Fig. 5.14a(ii) and an underestimation at the energy level of C in Fig. 5.14b(iii), the best-fit model is able to reproduce a similar trend as that observed and provide good agreement with the observed data (R^2 = 0.90), as shown in Fig 5.15. Moreover, Weibull P_E agreed with the observed values with R^2 = 0.97, which means that the Weibull distribution can also accurately estimate the undertow P_E.

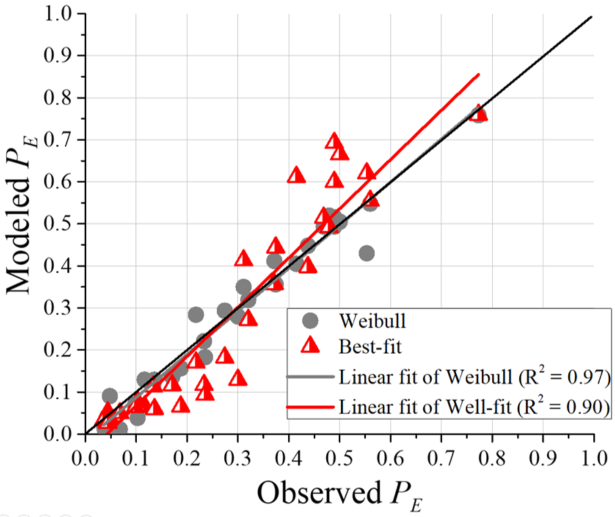

Figure 5.15: Best-fit modeled versus observed P_E (half-filled red triangle), and modeled Weibull versus observed P_E (gray circle) considering $u_E/\overline{u}$ = 1.0 for HC16 and HC17.

5.5 Tidal range effect on undertow exceedance probability

The undertow velocities vary not only for wave energy flux, water depth and cross-shore location, but also for the tidal elevation [47, 102]. The study of Pugh [73] on the estimation of extreme currents for the design of off-shore structures using field data observed at the Lincolnshire coast, in the North Sea, have already found that the tidal range subjected to the current velocities at the Inner Dowsing. The high amplitudes of currents were driven by tides and reached an extreme value on both the flood and ebb tide, but in opposite directions. To demonstrate the effect of tidal ranges on the undertow, in this Section, the exceedance probability distributions were distinguished by the water level as high-tide or low-tide data. This was defined by the MWL and its standard deviation (W_{SD}) as previously mentioned in Fig. 4.3 for 2016 and Fig. 4.6 for 2017:

$$W_L > MWL + 0.5W_{SD} : 0.89\ m \quad \text{for high-tide durations,} \tag{5.4}$$

$$W_L > MWL - 0.5W_{SD} : 0.61\ m \quad \text{for low-tide durations.} \tag{5.5}$$

Firstly, the number of undertow datasets after separating into the full, high-tide and low-tide data were counted as listed in Table 5.7. The gray-uncolored bounds the undertow datasets that accounted for more than 50% of the total data at the same band in Table **??** and were used to discuss later in Fig. 5.16. The average occupancy ratio of high-tide and low-tide data were 47.5% and 20.7% for energy level of B, 28.5% and 25.9% for energy level of C and 36.6% and 30.2% for energy level of D, respectively.

Secondly, the same procedures as Fig. 5.5 were conducted to compute the undertow exceedance probability for both the high-tide and low-tide durations. The distributions of undertow exceedance probability of 2016 datasets for the different tides of wave energy levels of B, C and D at the considered locations of x = 96, 116, 126, 161 and 191 m are shown in Fig. 5.16. Each color represents the differences of data types. The full, high-tide and low-tide data are referred by black, pink and blue color, respectively.

Table 5.7: Number of 2016 undertow datasets by separating into full-tide, high tide and low-tide durations.

Wave energy level	Tide	Number of undertow datasets (2016)									
		$x = 96$ m		$x = 116$ m		$x = 126$ m		$x = 161$ m		$x = 191$ m	
		N_{96}	%	N_{116}	%	N_{126}	%	N_{161}	%	N_{191}	%
A	High	23	53.5	18	54.5	11	47.8	-	-	-	-
	Low	5	11.6	6	18.2	6	26.1	-	-	-	-
	Total	43	100	33	100	23	100	0	-	0	-
B	High	36	42.4	38	48.7	35	51.5	5	71.4	-	-
	Low	20	23.5	14	17.9	14	20.6	1	14.3	-	-
	Total	85	100	78	100	68	100	7	100	0	-
C	High	30	22.9	31	29.0	29	33.3	22	28.6	16	34.0
	Low	43	32.8	26	24.3	20	23.0	18	23.4	3	6.4
	Total	131	100	107	100	87	100	77	100	47	100
D	High	50	32.9	67	37.6	55	34.2	63	39.1	48	39.0
	Low	49	32.2	51	28.7	51	31.7	48	29.8	35	28.5
	Total	152	100	178	100	161	100	161	100	123	100

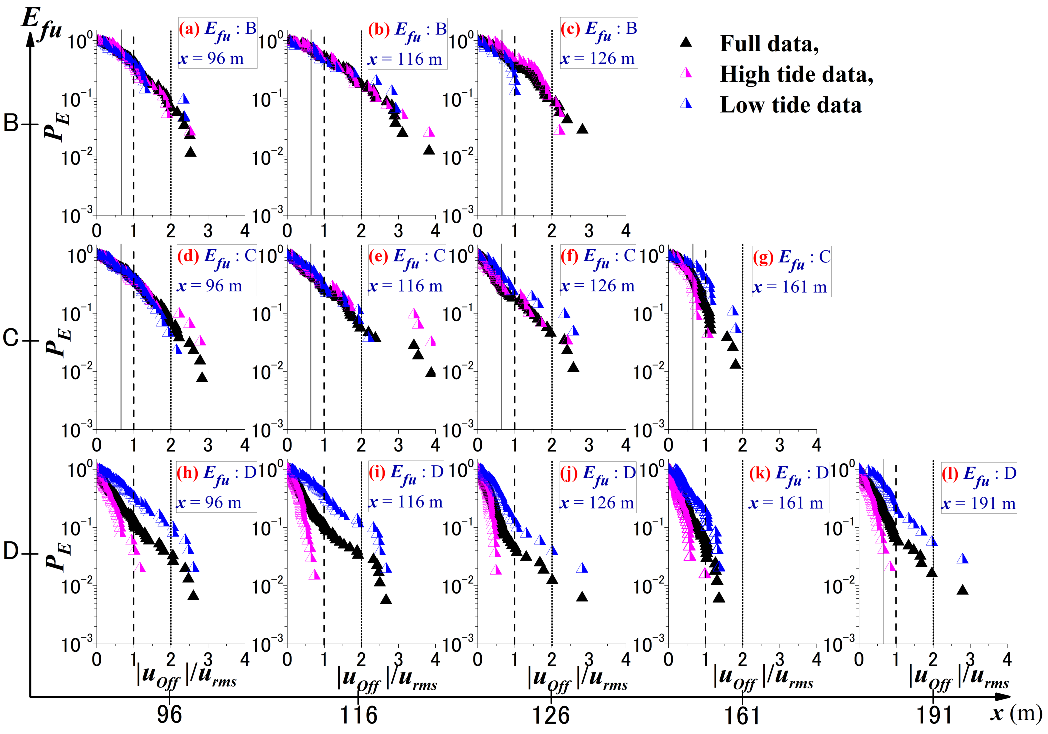

Figure 5.16: Observed exceedance probability applicable to normalized undertow distinguished by water level (field observation in May, 2016).

The undertow exceedance probability of the full, high-tide, and low-tide data had the same curves for wave energy levels of B and C, but the differences in the exceedance probability distributions increased when the wave energy flux decreased, and the undertow was more affected by the change in water level. In the energy level of D, it can be clearly seen that exceedance probability of the low-tide data was higher than that of the full data, and the exceedance probability of the high-tide data was the lowest from the criteria of $u_E/\overline{u} = 0.3$. The solid, dashed and dotted lines in each panel indicate the normalized undertow at the criteria of $u_E/\overline{u} = 0.67$, 1.00 and 2.00, respectively. Note that there was no high-tide data in excess of $u_E/\overline{u}$ $= 1$ for overall energy level of D.

Regarding the undertow exceedance probability at the criteria of $u_E/\overline{u} = 1$, Fig. 5.17 shows the spatial distributions of them for the full, high-tide, and low-tide data of each wave energy flux level. Lack of a mark denotes that there was no observed data for this criteria, and the number of data in wave energy level of A was small to be used.

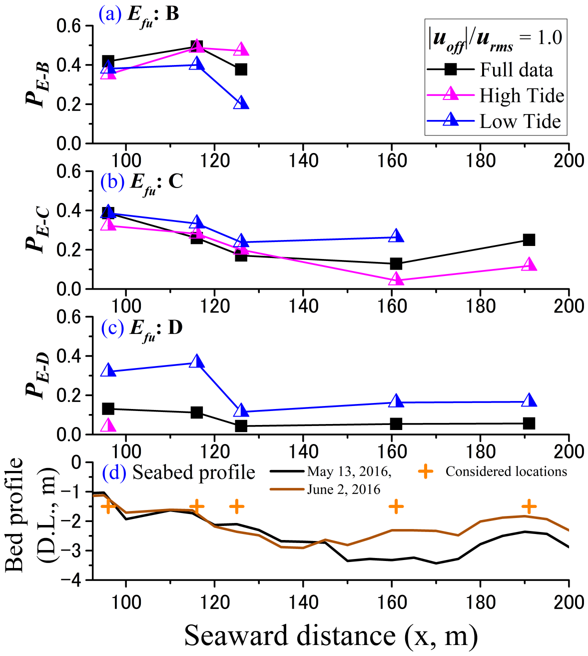

Figure 5.17: Spatial distributions of undertow exceedance probability on $u_E/\overline{u}$ for full, high-tide, and low-tide data of each wave energy flux level. (field observation in May, 2016).

Form Fig. 5.17, the undertow exceedance probability was higher near the inner bar region (x = 116 m) compared to further locations, i.e., x = 126 and 161 m. Although the trends were almost the same at each wave energy level, the spatial distribution of the undertow exceedance probability indicated a greater change by the effect of the water level when the wave energy decreased (from B to D). The distribution of the low-tide data of wave energy level D showed the highest exceedance probability in every considered location. The percentage of the measured exceedance probability at u_E = -0.10 m/s ($u_E/\overline{u}$ = 1.0) considering tide durations for the observation in 2016 was summarized in Table 5.8. The ratio of the low-tide data to full data (P_{E-low}/P_{E-full}) at energy level D was higher than those of levels B and C. The average ratios of P_{E-low}/P_{E-full} of every location for wave energy levels B, C, and D were 0.75, 1.43, and 2.87, respectively. Moreover, the average ratio of the low-tide data for wave energy level D increased to about four times higher than that of level B.

Table 5.8: Percentage of the measured exceedance probability at u_E = 0.10 m/s ($u_E/\overline{u}$ = 1.0) considering tide durations for the observation in 2016.

Wave energy level	Tide duration	Percentage of undertow exceedance probability at 0.10 m/s (2016)				
		x = 96 m	x = 116 m	x = 126 m	x = 161 m	x = 191 m
B	Full data	41.86	49.37	37.68	-	-
	High Tide	35.14	48.72	47.22	-	-
	Low Tide	38.10	40.00	20.00	-	-
C	Full data	38.64	25.92	17.04	12.82	25.00
	High Tide	32.26	28.12	20.00	4.35	11.76
	Low Tide	38.64	25.92	23.81	36.84	-
D	Full data	13.07	11.17	4.32	5.39	5.64
	High Tide	3.92	-	-	-	-
	Low Tide	32.00	36.54	11.54	16.33	16.67

From these results, the undertow velocities can also be affected by the water level. Although some theoretical undertow models have been existed and seems well to be used for predicting the mean undertow, it is necessary to account for the effect of tidal elevations in the models. It has been proven that the undertow exceedance probability of the low-tide data was approximately three times higher than that of the full-tide data, especially during low-energy wave conditions.

Table 5.9: Number of 2017 undertow datasets by separating into full-tide, high tide and low-tide durations.

Wave energy level	Tide	Number of undertow datasets (2017)									
		x = 116 m		x = 126 m		x = 161 m		x = 191 m		x = 221 m	
		N_{116}	%	N_{126}	%	N_{161}	%	N_{191}	%	N_{221}	%
A	High	11	44.0	13	48.1	-	-	-	-	-	-
	Low	9	36.0	8	29.6	-	-	-	-	-	-
	Total	25	100	27	100	0	-	0	-	0	-
B	High	18	33.3	18	33.3	7	53.8	1	-	-	-
	Low	14	25.9	15	27.8	0	0.0	0	-	-	-
	Total	54	100	54	100	13	100	1	-	0	-
C	High	23	38.3	21	34.4	22	39.3	11	39.3	-	-
	Low	11	18.3	11	18.0	12	21.4	9	32.1	-	-
	Total	60	100	61	100	56	100	28	100	0	-
D	High	8	20.5	14	22.2	9	15.3	7	13.2	10	17.5
	Low	16	41.0	20	31.7	23	39.0	23	43.4	26	45.6
	Total	39	100	63	100	59	100	53	100	57	100

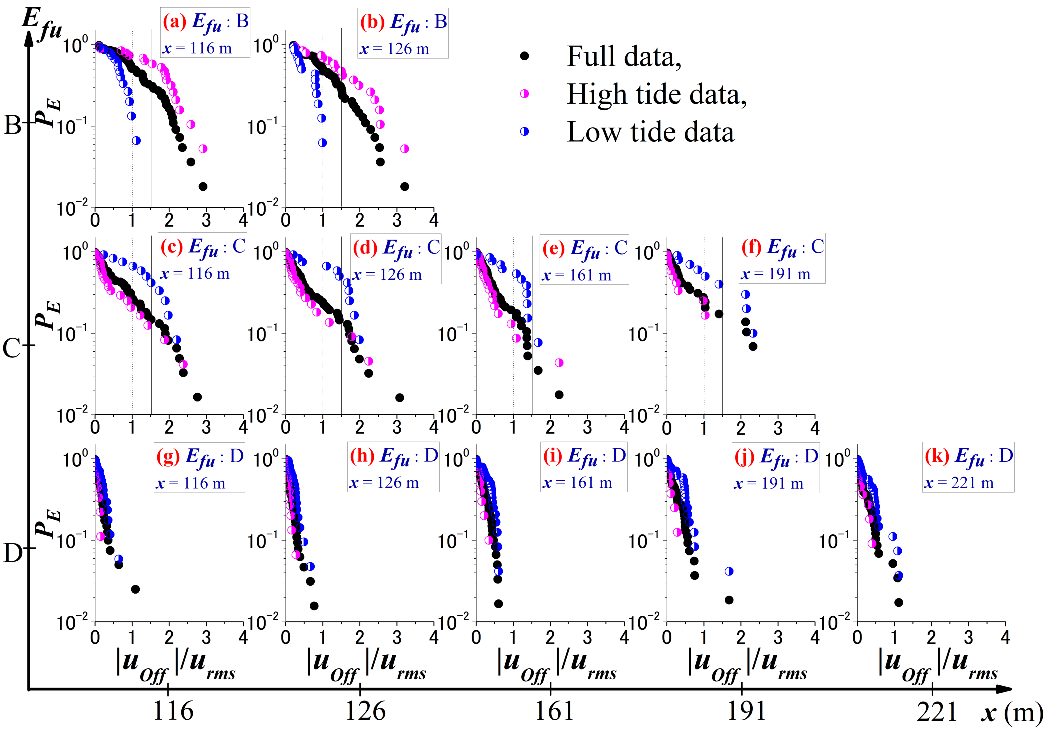

Figure 5.18: Observed exceedance probability applicable to normalized undertow distinguished by water level (field observation in May, 2017).

Besides the applying the joint tidal range analysis on the undertow exceedance probability of 2016 field data, the 2017 undertow datasets were also operated in the same processes. The definitions of high-tide and low-tide were differently defined as,

$$W_L > MWL + 0.5W_{SD} : 0.79\ m \quad \text{for high-tide durations,} \tag{5.6}$$

$$W_L > MWL - 0.5W_{SD} : 0.53\ m \quad \text{for low-tide durations.} \tag{5.7}$$

The number of undertow datasets after separating into the full, high-tide and low-tide data were summarized in Table 5.9. The gray-uncolored bounds the undertow datasets that accounted for more than 50% of the total data at the same band in Table **??** and were discussed more. The average occupancy ratio of high-tide and low-tide data were 33.3% and 26.9% for energy level of B, 37.8% and 22.5% for energy level of C and 17.7% and 40.1% for energy level of D, respectively. The distributions of undertow exceedance probability of 2017 datasets for the different tides of wave energy levels of B, C and D at the considered locations of $x = 116$, 126, 161, 191 and 221 m are shown in Fig. 5.18. Each color represents the differences of data types. The full, high-tide and low-tide data are referred by black, pink and blue color, respectively.

Differently exceedance probability distributions can be seen, the undertow exceedance probability of the full, high-tide, and low-tide data had the various curves for wave energy levels of B and C, but the same curves for wave energy level of D. At the high-energy wave condition (level B), high-tide resulted in the increase in undertow exceedance probability. In contrast, the undertow exceedance probability of high-tide decreased and was lower than that of full and low-tide data at the low-energy wave condition (level C). In addition, the exceedance probability was easier to be exceeded an extreme undertow velocity when affected by the low-tide duration. However, there was no difference of the curves in the energy level of D because of the low frequency waves of the very calm condition and the smoothness of beach profile. The dotted and solid lines in each panel indicate the normalized undertow at the criteria of $u_E/\overline{u} = 1.0$ and 1.5, respectively. Note that there was no data in excess of $u_E/\overline{u} = 1$ for energy level of D.

Fig. 5.19a and b respectively shows the spatial distributions of the undertow exceedance probability at the criteria of $u_E/\overline{u} = 1.0$ and 1.5, for the full, high-tide, and low-tide data of each wave energy flux level. Lack of a mark denotes that there was no observed data for this criteria, and the number of data in wave energy level of A was small to be used.

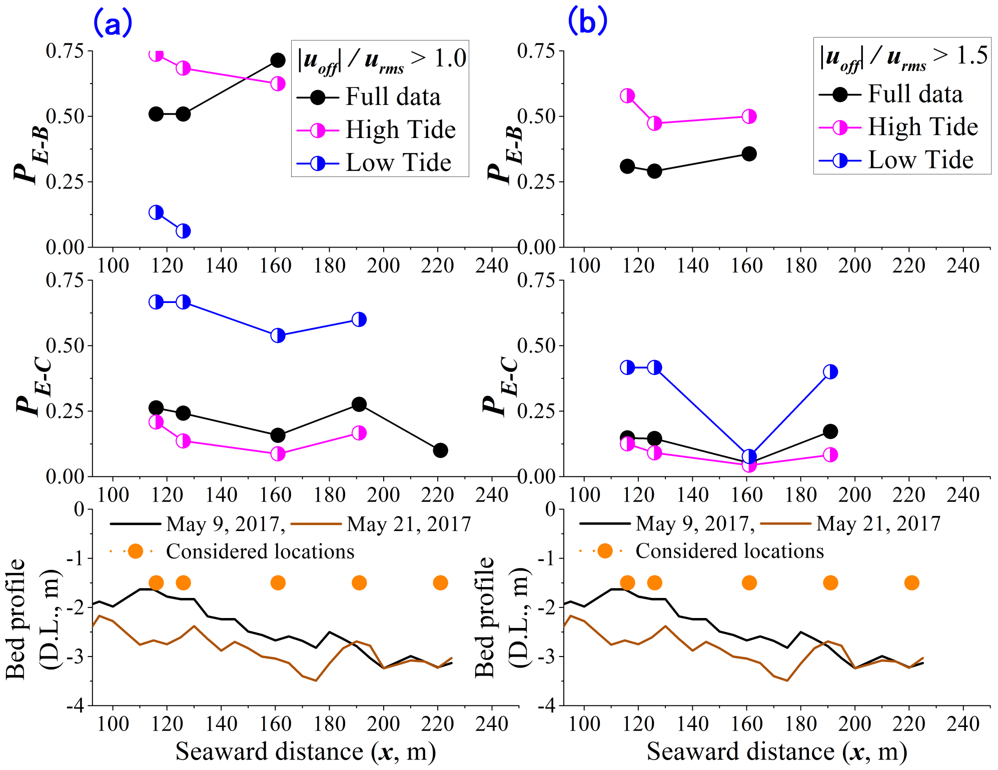

Figure 5.19: Spatial distributions of undertow exceedance probability on $u_E/\overline{u} = 1.0$ and 1.5 for full, high-tide, and low-tide data of each wave energy flux level. (field observation in May, 2017).

Both of criteria of $u_E/\overline{u} = 1.0$ and 1.5 showed that the undertow exceedance probability of high-tide was higher than that of full data at the energy level B, and the undertow exceedance probability of low-tide was in contrary higher than that of full data at the energy level C. Moreover, the exceedance probability curves at this energy level were likewise the cross-shore seabed profile. The exceedance probabilities of all full, high-tide and low-tide data were decreased due to the larger water depth in farther locations and then induced by the short water depth at the ripple region ($x = 191$ m) to having an increase in undertow exceedance probability. The percentage of the measured exceedance probability at $u_E =$ -0.13 m/s and 0.20 m/s ($u_E/\overline{u} = 1.0$ and 1.5) considering tide durations for the observation in 2017 was summarized in Table 5.10.

Table 5.10: Percentage of the measured exceedance probability at $u_E = 0.13$ m/s and 0.20 m/s ($u_E/\overline{u} = 1.0$ and 1.5) considering tide durations for the observation in 2017.

Wave energy level	Tide duration	Percentage of undertow exceedance probability at 0.13 m/s (2017)				
		x = 116 m	x = 126 m	x = 161 m	x = 191 m	x = 221 m
B	Full data	50.91	50.91	71.43	-	-
	High Tide	73.68	68.42	62.50	-	-
	Low Tide	13.33	6.25	-	-	-
C	Full data	26.23	24.19	15.79	27.59	10.00
	High Tide	20.83	13.64	8.70	16.67	-
	Low Tide	66.67	66.67	53.85	60.00	-
D	Full data	2.50	-	-	-	3.45
	High Tide	-	-	-	-	-
	Low Tide	-	-	-	-	7.41
Wave energy level	Tide duration	Percentage of undertow exceedance probability at 0.20 m/s (2017)				
		x = 116 m	x = 126 m	x = 161 m	x = 191 m	x = 221 m
B	Full data	30.91	29.09	35.71	-	-
	High Tide	57.90	47.37	50.00	-	-
	Low Tide	-	-	-	-	-
C	Full data	14.75	14.52	5.26	17.24	-
	High Tide	12.50	9.09	4.35	8.33	-
	Low Tide	41.67	41.67	7.69	40.00	-
D	Full data	-	-	-	1.85	-
	High Tide	-	-	-	-	-
	Low Tide	-	-	-	4.17	-

From Table 5.10, the ratio of the low-tide data to full data (P_{E-low}/P_{E-full}) at energy level C was higher than that of levels B, and there was no low-tide data at this considered criteria in energy level of D. At the criteria of $u_E/\overline{u} = 1.0$, the average ratios of P_{E-low}/P_{E-full} of every location for wave energy levels B and C were 0.19 and 2.72, respectively. For the criteria of $u_E/\overline{u} = 1.5$, the average ratios of P_{E-low}/P_{E-full} of every location for wave energy level C was 2.37 and there was no low-tide data for wave energy level B. This can be concluded that undertow was also induced by tide elevation, especially in low-tide duration besides wave energy flux, water depth and seaward location.

5.6 Discussion Points

In the surf zone, undertow highly affects to the change in bathymetry as it can carry large amounts of sediment seaward [67]. Existing science dogma regarding the common conception of undertow holds that the undertow is underneath the return flow and is able to push people seaward faster than they could swim toward land [19]. In order to suitably organize beaches and safe swimming, the management of coastal lands and ecosystems, including the precautions of swimming, needs to be highly concerned about the effects of undertow [13].

With regards to the previous Section, the measured undertow data from the field observations at HORS has already been analyzed to clarify the effects of wave energy flux, water depth and seaward location on the undertow exceedance probability. We suggested that the exceedance probability of undertow can be estimated using the Weibull distribution, which were differently derived from the relationship between the two-Weibull parameters and the n_e from the barred beach or unbarred beach condition. Moreover, we also proposed that the tide elevation should be accounted for the numerical models of undertow.

Thinking of the high cost of nearshore current velocities observations and, more seriously, handling the equipment in a storm event, the undertow would be difficult to be measured [73]. The statistically developed model is a meaningful way for estimating undertow exceedance probability, including undertow velocity in the field, and it requires only three hydraulics parameters which are normally and simply observed in the fields; wave energy flux, water depth and cross-shore location.

The undertow exceedance probability can be utilized to assess the impact of undertow velocity. An extreme value of undertow velocity is differently defined and also based on the applications. Next, some examples of applying the statistical model to the realistic practices are discussed.

5.6.1 Applications of the statistical model in practices

In this Section, we demonstrates how to apply the statistical model of undertow exceedance probability in practice uses. Three different cases relating to sediment movement will be considered as follows,

1) **Case 1: Settling velocity**

   First, the consideration is based on the settling velocity, which vary on the size of sediment particle. At HORS, the median diameter of the sand particle is 0.18 mm [42]. The settling velocity for this sand diameter can be calculated following the Stoke's law as,

   $$w = \frac{gd^2\left(\frac{\rho'}{\rho} - 1\right)}{18\nu}. \tag{5.8}$$

   This yields the settling velocity of 0.067 m/s for the sand diameter of 0.18 mm. The amount of velocity seems pretty low to be discussed, but it naturally occurs in a calm situation obviously and the cumulative effect causes the seabed profile to be changed. Assume that sediment particles are settling with the velocity of 0.067 m/s, simultaneously, the undertow velocity is generated to be 0.067 m/s or higher, the sediment particles can be hold by this undertow and moved seaward.

2) **Case 2: Root-mean-square value of undertow**

As already discussed in Chapter 5, we verified the statistical model with the measured exceedance probability and also showed the spatial distributions for every energy level and considered cross-shore location at the value of $u_E/\overline{u}$ = 0.10 m/s for 2016 data and 0.13 m/s for 2017 data, or $u_E/\overline{u}$ = 1.0. The results of the comparison have approximately been presented together with reasonably explaining.

3) **Case 3: Critical velocity**

Finally, we concern about the critical velocity for sediment diameter of 0.18 mm. Fig. 5.20 shows the diagram of the relationship between the particle size and velocity, proposed by Filip Hjulström [51]. It can be seen that the fine sand of the diameter of 0.18 mm starts moving at the cross-shore velocity about 0.20 m/s and then reaches the erosion velocity of 0.50 m/s. In this thesis, the critical velocity of 0.20 m/s is mentioned.

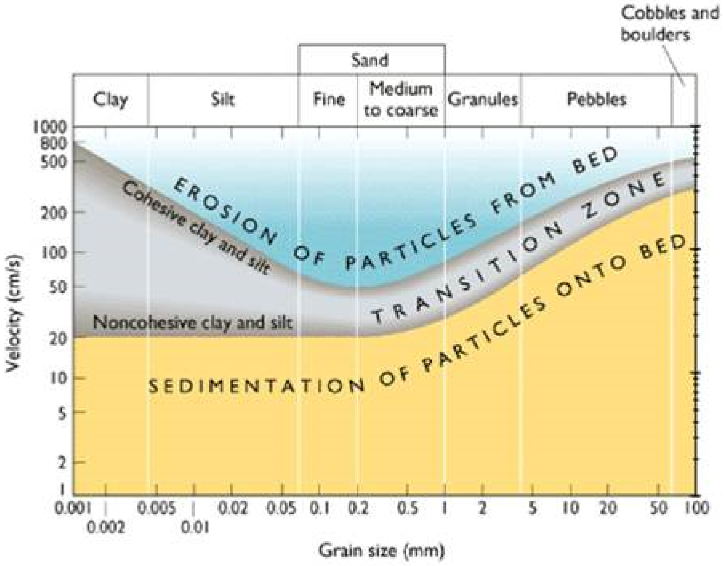

Figure 5.20: Filip Hjulström diagram [51]

Table 5.11: Summary of the velocity and normalized values of undertow in each case.

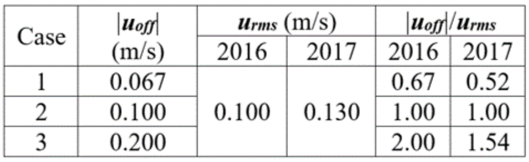

Case	$\lvert u_{off}\rvert$ (m/s)	u_{rms} (m/s)		$\lvert u_{off}\rvert/u_{rms}$	
		2016	2017	2016	2017
1	0.067	0.100	0.130	0.67	0.52
2	0.100			1.00	1.00
3	0.200			2.00	1.54

The considered velocities and the normalized values of undertow in each case for both 2016 and 2017 data are summarized in Table 5.11. The spatial distributions between the measured and modeled of undertow exceedance probability on these three of criteria are illustrated in Fig. 5.21 for 2016 data and Fig. 5.22. The symbols of square, triangle and circle represent the comparisons of case 1, 2 and 3, respectively. Different colors and lines distinguish the differences between the measure and modeled exceedance probability.

Fig. 5.21 ensure the capability of the statistical model that it can be used to estimate the undertow exceedance probability in the different cases. For high-energy wave conditions (level A and B), the error decreases as the increase in the certain values of u_E = -0.067, 0.10 and 0.20 m/s, respectively. In the contrary, the error increases as the increase in those certain values for low-energy wave conditions (level C and D). Although the exceedance probability of undertow from the location of x = 116 m to x = 191 m are underestimated at the energy levels of B and C for case 3, the differences of the average between the measured and modeled exceedance probability account for 7% and less than 1%, respectively. Furthermore, the different average values between the measured and modeled exceedance probability of wave energy levels of A and D are less than that of energy levels B at the same case. The percentage of undertow exceedance probability for all of cases, wave energy levels and locations are summarized in Table 5.12.

Similarly, the 2017 undertow datasets were conducted to investigate the spatial distributions of undertow exceedance probability on the criteria of $u_E/\overline{u}$ = 0.52, 1.0 and 2.0 as shown in Fig. 5.22 and the percentage of undertow exceedance probability for all of cases, wave energy levels and locations are summarized in Table 5.13.

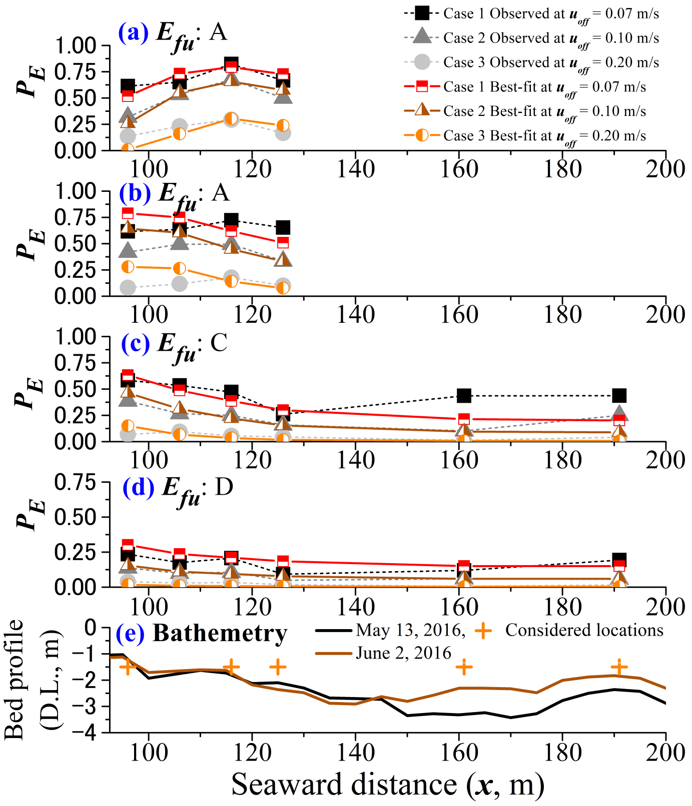

Figure 5.21: Spatial distributions of undertow exceedance probability on $u_E/\overline{u} =$ 0.67, 1.0 and 2.0 for full, high-tide, and low-tide data of each wave energy flux level (field observation in May, 2016).

Table 5.12: Percentage of undertow probability exceeding the differently extreme currents of u_E = -0.067, -0.10 and -0.20 m/s ($u_E/\overline{u}$ = 0.67, 1.0 and 2.0) for the observation in 2016.

Location (m)	**Case 1** - Percantage of exceedance probability at velocity of 0.067 m/s (2016)							
	Energy level A		Energy level B		Energy level C		Energy level D	
	Observed	Best fit	Observed	Best fit	Observed	Best fit	Observed	Best fit
96	61.36	51.73	61.63	78.85	58.33	63.27	23.53	30.14
106	65.12	73.26	63.53	74.90	53.45	48.79	17.54	23.64
116	82.35	79.43	72.15	61.93	47.22	38.71	20.67	21.06
126	66.67	72.73	65.22	50.83	26.14	29.95	9.26	18.41
161	-	-	-	-	43.59	21.45	11.98	15.07
191	-	-	-	-	43.75	20.14	19.35	15.01
Average	68.87	69.29	65.63	66.63	45.41	37.05	17.06	20.55

Location (m)	**Case 2** - Percantage of exceedance probability at velocity of 0.10 m/s (2016)							
	Energy level A		Energy level B		Energy level C		Energy level D	
	Observed	Best fit	Observed	Best fit	Observed	Best fit	Observed	Best fit
96	31.82	34.03	41.86	62.67	38.64	41.26	13.73	14.66
106	53.49	57.93	49.41	54.55	26.72	28.12	9.94	10.76
116	67.65	62.43	49.37	39.92	25.00	20.42	10.61	9.31
126	50.00	51.77	33.33	29.81	15.91	14.55	4.94	7.89
161	-	-	-	-	10.26	9.52	5.99	6.19
191	-	-	-	-	25.00	8.81	5.65	6.16
Average	50.74	51.54	43.49	46.74	23.59	20.45	8.48	9.16

Location (m)	**Case 3** - Percantage of exceedance probability at velocity of 0.20 m/s (2016)							
	Energy level A		Energy level B		Energy level C		Energy level D	
	Observed	Best fit	Observed	Best fit	Observed	Best fit	Observed	Best fit
96	13.64	0.89	8.14	27.92	6.82	15.01	3.92	1.81
106	23.26	15.85	11.76	26.46	9.48	6.71	2.92	1.01
116	29.41	30.38	17.72	14.00	5.56	3.49	3.35	0.77
126	16.67	23.95	10.14	7.57	4.55	1.79	1.85	0.57
161	-	-	-	-	1.28	0.80	0.60	0.37
191	-	-	-	-	4.17	0.69	1.61	0.37
Average	20.74	17.77	11.94	18.99	5.31	4.75	2.38	0.82

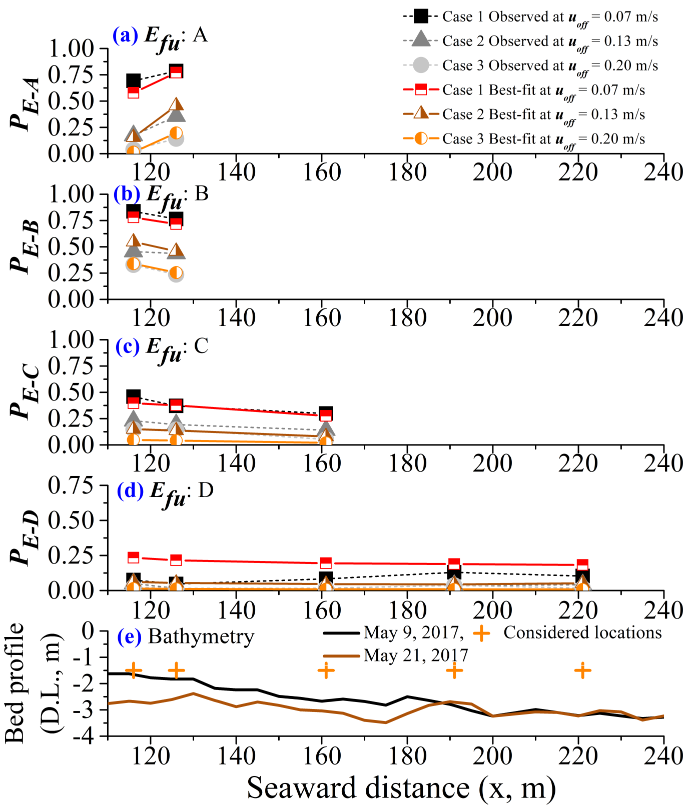

Figure 5.22: Spatial distributions of undertow exceedance probability on $u_E/\overline{u} =$ 0.52, 1.0 and 2.0 for full, high-tide, and low-tide data of each wave energy flux level (field observation in May, 2017).

From Fig. 5.22, we obviously see that the measure undertow exceedance probability in every case can well be estimated by using the proposed model. Each of exceedance probability curves in each energy level are similar to the measured. The highest difference of the average exceedance probability between the measured and modeled is 11.5% at the energy level D of case 1. Compare to the results using 2016 undertow data, the modeled exceedance probability gives the better agreement with the measured.

To summarize the above discussion, the statistical model applying Weibull distribution can be used in any extreme conditions of undertow. The model can well estimate the undertow exceedance probability even in the high-energy wave condition with the low different percentage of the average between the measured and modeled exceedance probability.

Table 5.13: Percentage of undertow probability exceeding the differently extreme currents of u_E = -0.067, -0.10 and -0.20 m/s ($u_E/\overline{u}$ = 0.52, 1.0 and 2.0) for the observation in 2017.

Location (m)	**Case 1** - Percantage of exceedance probability at velocity of 0.067 m/s (2017)							
	Energy level A		Energy level B		Energy level C		Energy level D	
	Observed	Best fit	Observed	Best fit	Observed	Best fit	Observed	Best fit
116	69.23	57.87	83.64	77.94	45.90	39.67	7.50	23.46
126	78.57	77.06	76.36	71.57	37.10	37.60	4.69	21.56
161	-	-	-	-	29.82	27.61	8.33	19.45
191	-	-	-	-	-	-	12.96	18.89
221	-	-	-	-	-	-	10.34	18.21
Average	73.90	67.46	80.00	74.75	37.61	34.96	8.77	20.31

Location (m)	**Case 2** - Percantage of exceedance probability at velocity of 0.13 m/s (2017)							
	Energy level A		Energy level B		Energy level C		Energy level D	
	Observed	Best fit	Observed	Best fit	Observed	Best fit	Observed	Best fit
116	17.25	15.46	45.45	54.69	22.95	15.00	5.00	6.20
126	35.71	45.66	43.64	45.80	19.35	13.65	1.56	5.41
161	-	-	-	-	14.04	8.08	1.67	4.60
191	-	-	-	-	-	-	3.70	4.39
221	-	-	-	-	-	-	4.15	5.17
Average	26.48	30.56	44.55	50.24	18.78	12.24	3.22	5.15

Location (m)	**Case 3** - Percantage of exceedance probability at velocity of 0.20 m/s (2017)							
	Energy level A		Energy level B		Energy level C		Energy level D	
	Observed	Best fit	Observed	Best fit	Observed	Best fit	Observed	Best fit
116	3.85	1.50	32.73	33.89	14.75	4.74	2.50	1.39
126	14.29	19.74	23.64	25.49	14.52	4.14	1.56	1.16
161	-	-	-	-	5.26	1.99	1.67	0.93
191	-	-	-	-	-	-	3.70	0.88
221	-	-	-	-	-	-	1.72	0.82
Average	9.07	10.62	28.18	29.69	11.51	3.62	2.23	1.04

Next Section, the tidal effect on the undertow in excess of the three of considered current velocities will be described by the same method as appeared in Chapter 5.

5.6.2 Tidal range effect on undertow in different cases

The example of utilizing the undertow exceedance probability in practice has already been clarified by the separation of undertow exceedance probability into high-tide and low-tide durations in Section 5.5 to discuss the effect of tidal range on undertow. In this Section, we conducted the same process but for the different extreme undertow to observe the characteristics of high and low-tide on undertow exceedance probability when the undertow exceeded an extreme velocity. The spatial distributions of undertow exceedance probability (2016) of full, high-tide, and low-tide data in excess of u_E = -0.067, -0.13 and -0.20 m/s ($u_E/\overline{u}$ = 0.67, 1.0 and 2.0) can be illustrated as shown by Fig. 5.23 and Fig. 5.24 for wave energy level B and D, respectively.

Fig. 5.23a, 5.23b and 5.23c show the spatial distributions of observed exceedance probability for full, high-tide, and low-tide data of wave energy level B for different criteria of undertow, u_E = -0.067, -0.13 and -0.20 m/s ($u_E/\overline{u}$ = 0.67, 1.0 and 2.0), respectively. Each criterion is represented in Fig. 5.16 by the solid, dashed and dotted vertical lines. Note that the no mark indicates the undertow in excess of the criteria were not observed. The initial and final beach profiles are shown in Fig. 5.23c.

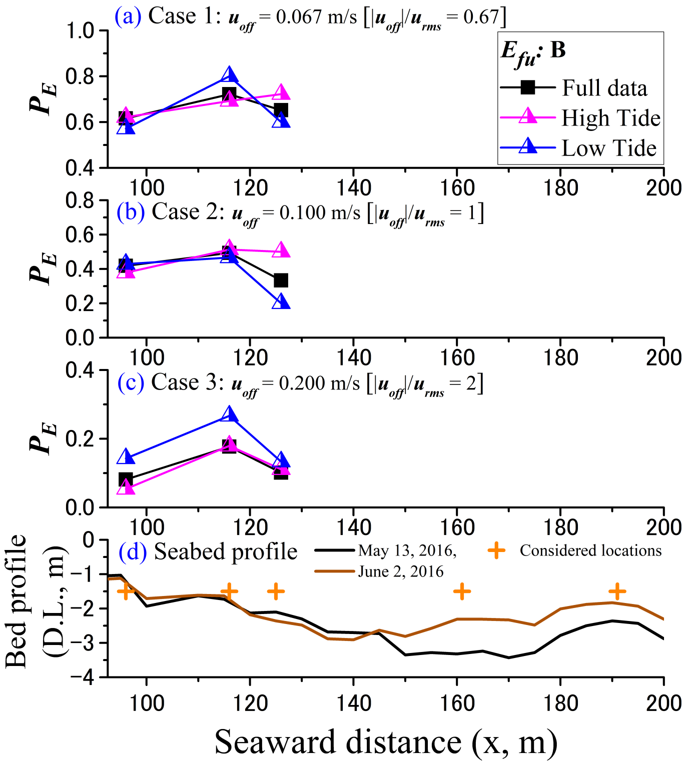

Figure 5.23: Spatial distributions of undertow exceedance probability on $u_E/\overline{u} \geq 1$ for full, high-tide, and low-tide data of each wave energy flux level (field observation in May, 2016).

At the criteria of u_E = -0.067 and -0.13 m/s, the exceedance probability curves of full, high-tide, and low-tide data were similar, except u_E = -0.13 m/s at the location of x = 126 m where the high-tide data showed the highest exceedance probability. The increase in the criteria of undertow to u_E = -0.20 m/s resulted in the higher exceedance probability of low-tide data. Moreover, the spatial distribution of low-tide data at the highest criteria had the high exceedance probability in every location.

Fig. 5.24a, 5.24b and 5.24c show the spatial distributions of observed exceedance probability for full, high-tide, and low-tide data of wave energy level B for different criteria of undertow, u_E = -0.067, -0.13 and -0.20 m/s ($u_E/\overline{u}$ = 0.67, 1.0 and 2.0), respectively. Each criterion is represented in Fig. 5.16 by the solid, dashed and dotted vertical lines. Note that the no mark indicates the undertow in excess of the criteria were not observed. The initial and final beach profiles are shown in Fig. 5.24c.

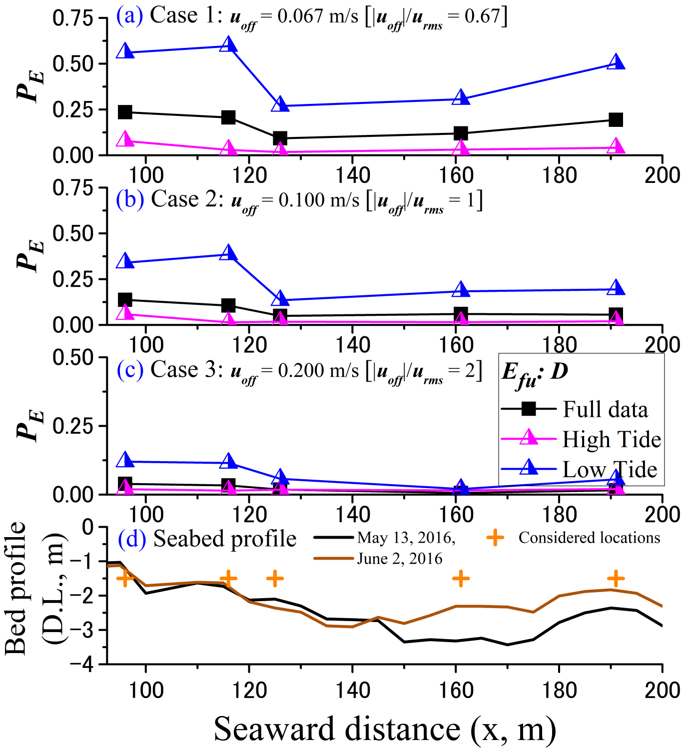

Figure 5.24: Spatial distributions of undertow exceedance probability on $u_E/\overline{u} \geq 1$ for full, high-tide, and low-tide data of each wave energy flux level (field observation in May, 2016).

For the low-tide duration, the spatial distributions of undertow exceedance probability were larger than those of the full and high-tide data for all cross-shore location. The increase in the criteria of undertow velocities from case 3 to case 1 led low-tide to more affect the undertow exceedance probability. Specially, the highest exceedance probability was on the lowest criteria of u_E = -0.067 (Fig. 5.24a). The results of energy level D contrasted to that of energy level B.

In conclusions, the different criteria of undertow differentiated the tidal effect on the spatial distribution of undertow, and low-tide induced the undertow in both high and low-energy wave condition. The undertow exceedance probability from the lower to higher criteria (u_E = -0.067, -0.13 and -0.20 m/s, respectively), the spatial distribution of low-tide during high-energy wave condition (level B) increased and showed a high exceedance probability at the highest criterion of u_E = -0.20 m/s. In the contrary, the spatial distribution of low-tide during low-energy wave condition (level D) decreased and showed a high exceedance probability at the lowest criterion of u_E = 0.20 m/s.

Chapter 6

XBeach (Kingsday Release)

Undertow in during storm events is easily generated by wave energy as a significant driver of coastal erosion. Periodically, undertow can also be induced by water level, that leads undertow to be stronger on a short water depth over an alongshore sandbar. Undertow can be predicted from theoretical models that were developed by comparing the modeled undertow to the observed undertow from laboratory. Because observations during the extreme storms are often unavailable owing to the difficulty of handling, or the instrument malfunction, some numerical models were used to simulate the wave-driven undertow to compare to the theoretical model and then create an approach to improve the accuracy of the existing model. Numerically simulated undertow was also validated by the observed data to evaluate model accuracy.

In this thesis, the observed undertow datasets at HORS were more usefully applied to assess the undertow prediction from a numerical scheme, XBeach model, since it had often been validated by only experimental undertow data. The modeled undertow was compared with the observed undertow to understand and quantify the accuracy of undertow prediction under the differences of hydraulics conditions. Although the simulations were modified several times by adjusting the parametric values, the model reproduced the underestimated undertow with the low qualification compared to the observed undertow. In order to increase the accuracy of the model, the results were theoretically recalculated by using a parameter of water depth ratio. The improvement resulted in better qualification of modeled undertow in all considered locations.

6.1 Introduction

A serious condition of storms can cause extensive changes to coastal bathymetry, including beach erosion and the formation of new inlets. These changes leads the coastal zone to be more vulnerable to future storms. Alongshore sandbars in the surf zone are normal features and show influences on the seabed profile changes [100]. In the coastal management, artificial sandbars were responsible for the prevention shoreline to the large storms as a soft solution and proposed to construct in many nourishment projects [56, 60]. To predict the sediment transport rate and the deformation of a sandbar, the nearshore currents are necessay for the calculation [44].

However, undertow is not easy to measure, particular under an extreme condition. High-energy waves and critical beach changes can damage the measuring instrument. One solution to dealing with the observational problems is to numerically simulate undertow. The consideration about a numerical model called 'XBeach' [80] was conducted.

With regards to many improvements of the XBeach model, the estimation of undertow have less been mentioned and also verified by only experimental data. For examples, Roelvink et al. [80] examined XBeach model against laboratory and prototype scale experiments of breaching of the Zwin sand dike, as presented by Visser [106]. The comparisons between the measured and simulated flow velocities of the breach width in time were given and the simulated flow velocity was higher than the measured. Considering about the surf zone, Jamal et al. [35] figured out that the onshore and offshore velocity profile envelopes expressed by using the Lagrangian formulation for XBeach were lower than the threshold velocity for the coarse sediments, compared to the higher of that obtained from the Eulerian formulation. This also causes to a smaller changes of seabed profile than it should be.

In order to simulate the undertow using XBeach for the future benefit of extending the statistical model of undertow to more energetic waves that were missing, the accuracy of the modeled undertow must be evaluated. In this study, the field datasets of undertow from HORS were used to evaluate the mean undertow prediction in XBeach model. Since the undertow datasets had been measured as having two differently hydraulic conditions: high-energy and low-energy wave conditions related to wave energy flux, and XBeach model could not adjust the parameters by itself, the undertow velocity in each condition was separately simulated across the ranges of conditions that have corresponding undertow observation. The objective is two-fold,

(1) To understand and quantify the accuracy of undertow predictions by using field data under the difference of hydraulic conditions.

(2) To improve the mean undertow prediction in XBeach model.

6.2 Methodology

The same of field hydraulics datasets at Hasaki coast (HORS), using for the development of the statistical model in Chapter 5 were also utilized to give a comparison between the observed and simulated undertow from XBeach model. According to the data description of the field observation in 2016, the undertow datasets had been measured as having two differently hydraulic conditions: high-energy and low-energy wave conditions related to wave energy flux, and also XBeach model could not adjust the parameters by itself, we separately simulated undertow velocity across the ranges of conditions that have corresponding undertow observation. Meanwhile, we were trying to assess the accuracy of the XBeach undertow prediction by tuning some parametric values, however, the results were underestimated compared to the measured. In order to increase the accuracy of the modeled undertow, we present a solution for improving the undertow prediction based on assimilating theoretical model results and observations. Next section, we provide a brief summary of XBeach model following XBeach manual, proposed by Roelvink et al. [81], and then describe the extraction of undertow prediction.

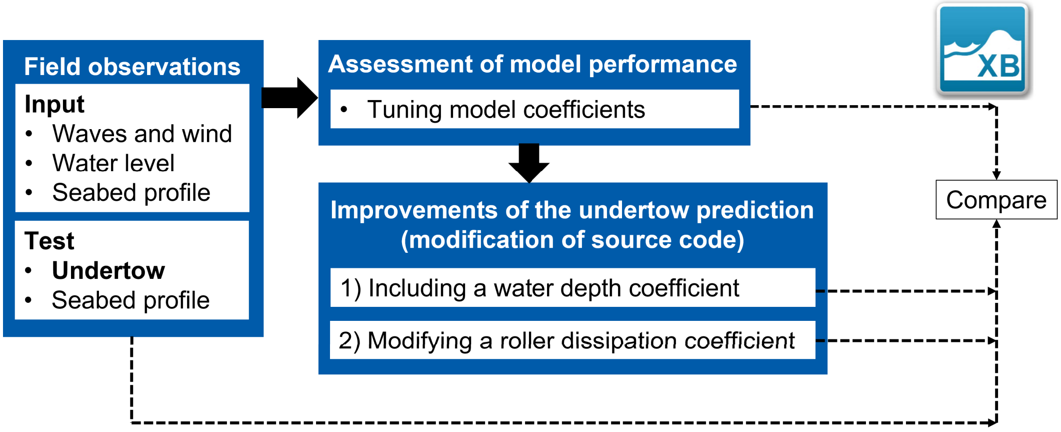

Figure 6.1: Chart of methodology for modeling undertow using XBeach.

6.2.1 Model description

XBeach model or ‘eXtreme Beach’was proposed by TU Delft, Netherlands. The model was initailly developed to simulate two-dimentional conditions of nearshore beach under hurricane or storm events [80]. The philosophies are to numerically assess the dominant hydrodynamics conditions and then absolutely resolve critical processes occurring on sandy coasts. The applications of XBeach model to some natural beaches have already been existed in various studies (e.g. McCall et al. [54], Williams et al. [109]). Recently, Roelvink et al. [79] increased the accurate prediction of wave run-up by improving the wave groupiness factor, and also clarified the effect of a new approach of single directional calculation $(single - dir)$ on the simulation, that decreased the deficiency in the two-dimensional infragravity runup.

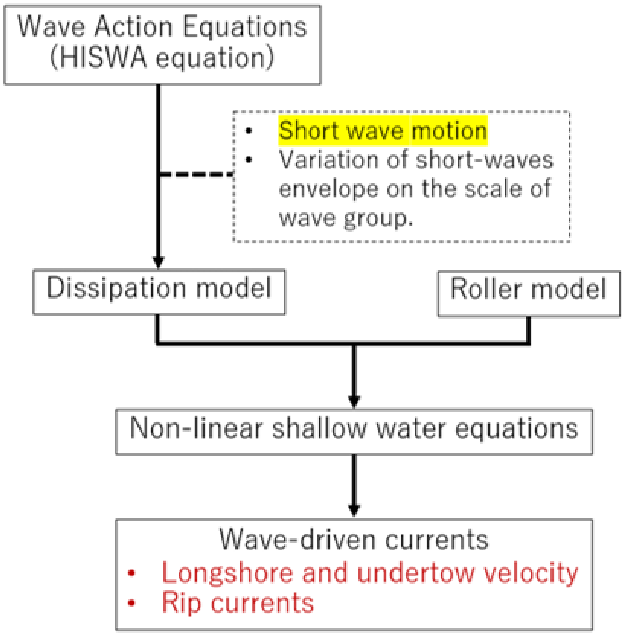

Figure 6.2: Chart of numerical processes for simulating undertow in XBeach model.

Basically, XBeach reproduces both of short- and long-wave motions generated by the variation in wave height in time through the wave action equation or so-called ‘surf-beat’. In the surf-beat mode, the wave action equation envelops the variation on the scale of Groupiness factor, and uses it in the employed dissipation model and roller model to represent surface momentum after wave breaking. Then, the radiation stress generated by this variation induces the infragravity waves and reversely unsteady currents (i.e. undertow) in the water column. To solve the wave-induced currents, the non-linear shallow water equation is included. Fig. 6.2 illustrates the above explanation. Here, the wave action equation, the dissipation model and the roller model are briefly explained because they are similar to the descriptions given in Chapter 2. The shallow water equation is described in Subsection 6.2.2.

- **Wave-action equation**

  The short-wave action equation is similar to a numerical model for the hindcasting of waves in shallow water, HISWA model [34]. This equation contains a parameter of wave energy dissipation after wave breaking (D_b). Following the formulation of Daly et al. [18] (*roelvink_daly*), the total wave energy dissipation, i.e. directional-integrated can be expressed as,

  $$\langle D_b \rangle = 2\frac{\alpha}{T_{rep}} Q_b E \tag{6.1}$$

  where,

  $$Q_b = 1 \quad \text{if } H_{rms} > \gamma h, \tag{6.2}$$

  $$Q_b = 0 \quad \text{if } H_{rms} < \gamma_2 h, \tag{6.3}$$

  the total wave energy dissipation is transferred proportionally over wave directions as given by,

  $$D_b(x, y, t, \theta) = \frac{S(x, y, t, \theta)}{E(x, y, t)} \langle D_b \rangle (x, y, t). \tag{6.4}$$

  According to linear wave theory, this can evaluate the radiation stresses as,

  $$S_{xx} = \int \left[\frac{C_G}{C}(1 + \cos^2\theta) - \frac{1}{2} \right] S d\theta, \tag{6.5}$$

  $$S_{yy} = \int \left[\frac{C_G}{C}(1 + \sin^2\theta) - \frac{1}{2} \right] S d\theta, \tag{6.6}$$

  $$S_{xy} = S_{yx} = \int \sin\theta \cos\theta \left[\frac{C_G}{C} S \right] d\theta. \tag{6.7}$$

- **Roller-energy balance**

  The roller energy balance is coupled to the wave action equation. According to the equation given by Reniers et al. [78], the total roller energy (D_r) is expressed as,

  $$\langle D_r \rangle = \tau_r C_G \tag{6.8}$$

where,

$$\tau_r = \frac{\rho g A_r}{L}\beta_r \tag{6.9}$$

the total roller energy dissipation is then proportionally given by,

$$D_r(x,y,t,\theta) = \frac{R(x,y,t,\theta)}{M(x,y,t)}\left\langle D_r\right\rangle(x,y,t). \tag{6.10}$$

The roller contribution to radiation stresses is expressed as,

$$R_{xx} = \int \cos^2\theta R d\theta, \tag{6.11}$$

$$R_{yy} = \int \sin^2\theta R d\theta, \tag{6.12}$$

$$R_{xy} = R_{yx} = \int \sin\theta\cos\theta R d\theta. \tag{6.13}$$

6.2.2 Undertow prediction

The shallow water equation is used to reproduce the low-frequency waves and wave-induced mean flow. The return flow, i.e. undertow is expressed in the form of Generalized Lagrangian Mean flow (GLM), as formulated by Andrews et al. [6]. The resulting GLM-momentum equations are given by,

$$\begin{aligned}\frac{\partial(u_L)}{\partial t} + u_L\frac{\partial(u_L)}{\partial x} + v_L\frac{\partial u_L}{\partial y} - f v_L - \nu_h\left(\frac{\partial^2 u_L}{\partial x^2} + \frac{\partial^2 u_L}{\partial y^2}\right)\\ = \frac{\tau_{sx}}{\rho h} - \frac{\tau_{bx}}{\rho h} - g\frac{\partial W_L}{\partial x} + \frac{F_x}{\rho h},\end{aligned} \tag{6.14}$$

$$\begin{aligned}\frac{\partial(v_L)}{\partial t} + u_L\frac{\partial(v_L)}{\partial x} + v_L\frac{\partial v_L}{\partial y} - f u_L - \nu_h\left(\frac{\partial^2 v_L}{\partial x^2} + \frac{\partial^2 v_L}{\partial y^2}\right)\\ = \frac{\tau_{sy}}{\rho h} - \frac{\tau_{by}}{\rho h} - g\frac{\partial W_L}{\partial y} + \frac{F_y}{\rho h},\end{aligned} \tag{6.15}$$

$$\frac{\partial W_L}{\partial t} + \frac{\partial h u_L}{\partial x} + \frac{\partial h v_L}{\partial y} = 0. \tag{6.16}$$

Where F_x and F_y represent the wave forcing combining the radiation stress due to wave breaking and surface roller in x- and y-directions, respectively,

$$F_x(x,y,t) = -\left(\frac{\partial S_{xx} + R_x x}{\partial x} + \frac{\partial S_{xy} + R_x y}{\partial y}\right), \tag{6.17}$$

$$F_y(x, y, t) = -\left(\frac{\partial S_{yy} + R_y y}{\partial y} + \frac{\partial S_{xy} + R_x y}{\partial x}\right). \tag{6.18}$$

For the observed undertow in this thesis, the calculation is presented in the Eulerian velocity as,

$$u_E = u_L - u_S, \tag{6.19}$$

where the Stokes drift in XBeach model follows the equation proposed by Phillips [71] as,

$$u_S = \frac{E\cos\theta}{\rho h C}. \tag{6.20}$$

6.3 Results of undertow simulations

Two simulations were set up to compare model results to field observations for verifying the undertow prediction in XBeach model. In this thesis, the field observation at Hasaki coast (HORS), Japan, was selected. The period of model results was from May 13 to June 2 in 2016, which was separated into the storm duration, May 13 - 23, and low-energetic wave duration, May 24 - June 2. Although the XBeach model can well predict under the storms condition, the low-energetic wave condition was also selected because undertow was strong owing to Eulerian drift forced by water depth and water level. The data descriptions of tidal elevation, wave and wind condition have already been written in Chapter 4. In this Section, the modeled results are given.

6.3.1 Model set-up and tuning parameters

A uniform grid size of 5 m cross-shore by 10 m longshore was applied, with a horizontal extent of 380 m cross-shore by 100 m uniform alongshore. The Roelvink-Daly formulation [18], with $\gamma = 0.45$ and $\gamma_2 = 0.15$ was used. The dimensionless friction coefficient from the Chézy value for the Hasaki coast is 60 that is corresponding to a typical Manning value for sandy coasts of 0.02 s/m$^{1/3}$. Moreover, some parameters related to wave motions in the shallow water equation and roller-balance equation were adjusted as summarized in Table 6.1.

Table 6.1: Parameter settings.

Parameter	**Description**	**Default**	**Used**	
			H	L
γ	Breaker index	0.55	0.45	0.45
γ - 2	Breaker index (*roelvink daly*)	0.3	0.15	0.15
hmin	Minimum depth for computation of underto velocity	0.2	0.001	0.2
C	Chazy roughness value	55	60	60
βs	Slope of breaking wave front in roller model	0.1	0.05	0.05
rfb	Switch to feedback maximum wave surface slope in roller energy	0	1	1

H = High-energetic wave case, L = Low-energetic wave case

- *hmin*: In very shallow water some processes need to be limited to avoid unrealistic behavior. the increase in *hmin* value prevents very strong return flows that might be occur in the storm events. Decreasing *hmin* to the lowest value give better result for the storm case of undertow simulation.

  Fig. 6.3 shows the values of skill and slope when *hmin* was being tuned. The solid and dashed lines indicate the skill and slope values of the regression line, respectively. Each color refers to each cross-shore location where the modeled undertow was taken. The black, red and blue colors indicate the location of x = 96, 116 and 126 m, respectively. Decreasing *hmin* gave the better slope for the prediction of undertow velocity in the high-energy wave condition. For the case of low-energetic wave, we conducted the same process but there was only a small change. Therefore, we used the default value.

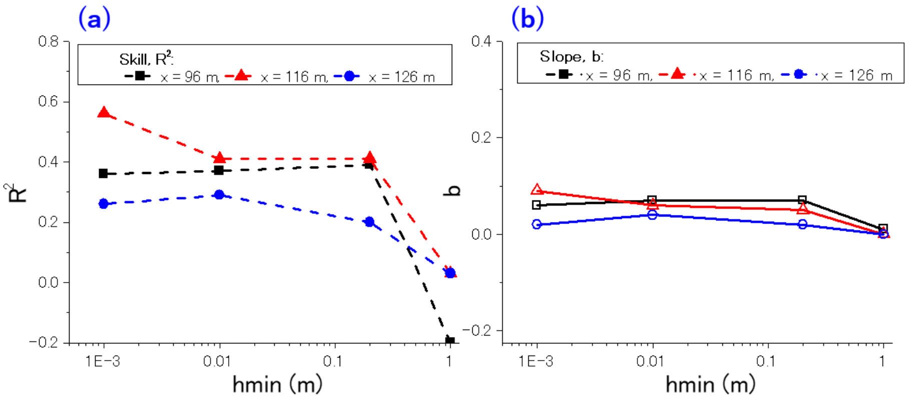

Figure 6.3: (a) skill and (b) slope values of tuning *hmin* for high-energy wave condition.

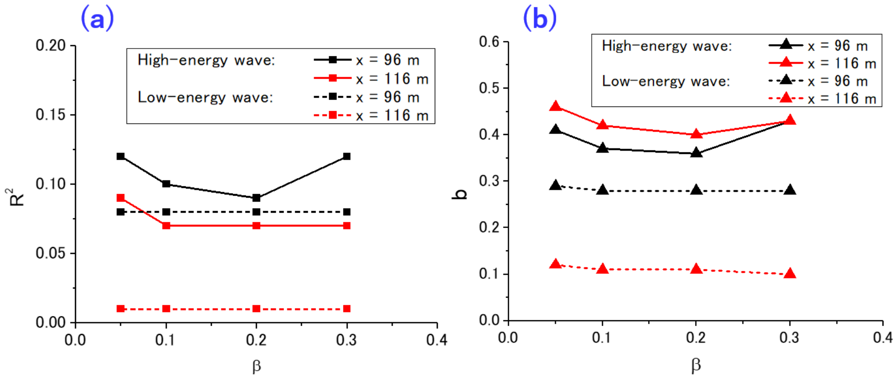

Figure 6.4: (a) skill and (b) slope values of tuning *Beta* for both of high- and low-energy wave conditions.

- ***Beta* (or β_r)**: The roller model reproduces the shoreward shift in wave-induced setup, return flow and alongshore current. *Beta* or the slope of breaking wave front is accounted for the calculation of roller dissipation in the roller model. The lower *Beta* value will give the larger shift. Regarding the validation of the hydrodynamics of the model against Delilah measurements by Roelvink [80], the prediction of the longshore velocity is sensitive to the *Beta*, with the value that is lower the default will give better results. In here, we tuned this *Beta* value for undertow.

  Fig. 6.4a and Fig. 6.4b show the values of skill and slope, respectively, when *Beta* was being tuned. The solid and dashed lines indicate high- and low-energy wave conditions, respectively. The locations of $x = 96$ and 116 m where the modeled undertow were considered, are respectively represented by black and red. The prediction of undertow velocity is also sensitive to the *Beta*, with *Beta* $= 0.05$ giving slightly better results for the high-energy wave case than the default value of *Beta* $= 0.10$.

- **rfb**: Turning rfb on (rfb = 1) is to feedback maximum wave surface slope in roller energy balance. Fig. 6.5a and Fig. 6.5b show the time-series of undertow velocity, Stokes drift and water depth at the location of $x = 96$ m for turning rfb off and on (rfb = 0 and 1), respectively. In panel 1, black and red refers to the observed and modeled undertow, respectively. The model result of rfb = 1 is closer to the observed line and higher than that of rfb = 0 as seen from the gap between these two lines and marked by yellow spots. Moreover, the comparison between the observed and modeled undertow of rbf = 1 gave the better results with the values of skill and slope of 0.11 and 0.43, compared to that of rbf = 0 with the values of skill and slope of 0.08 and 0.39, respectively. The Stokes drift and water depth in panel 2 and 3, respectively, were same between rfb = 0 and rfb = 1. Therefore, rfb = 1 was decided to apply for both undertow simulations.

6.3.2 Time shift

Although the parametric values of *hmin* and *Beta* were tuned, and the rfb was turned on to increase the accuracy the undertow prediction as much as XBeach can simulate, the skill and slope values were very low. Furthermore, the qualities of the performance of models evaluated by the models on the basis of the Relative Mean Absolute Error (RMAE) [105] and the Root Mean Square Error (RMSE) [44] were unacceptable (see more in Appendix. E for the equations of RMAE and RMSE).

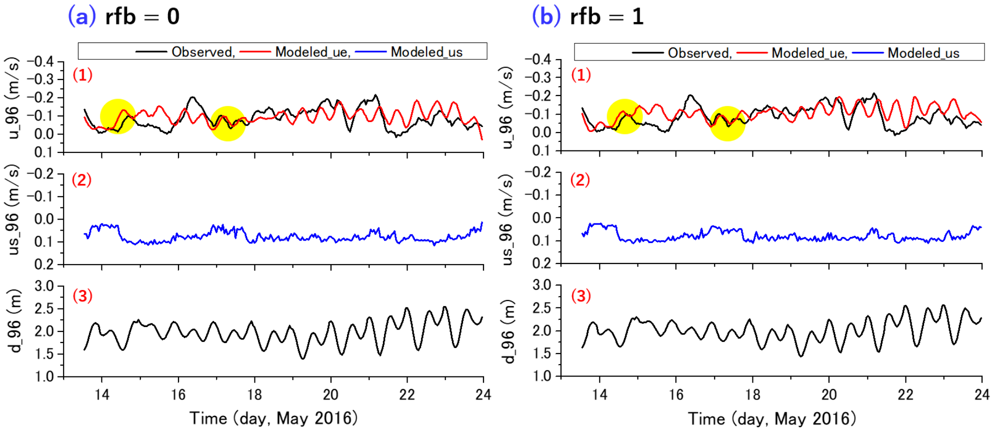

Figure 6.5: Time-series of (1) undertow velocity, (2) Stokes drift and (3) water depth at the location of $x = 96$ m: (a) rfb = 0 (b) rfb = 1.

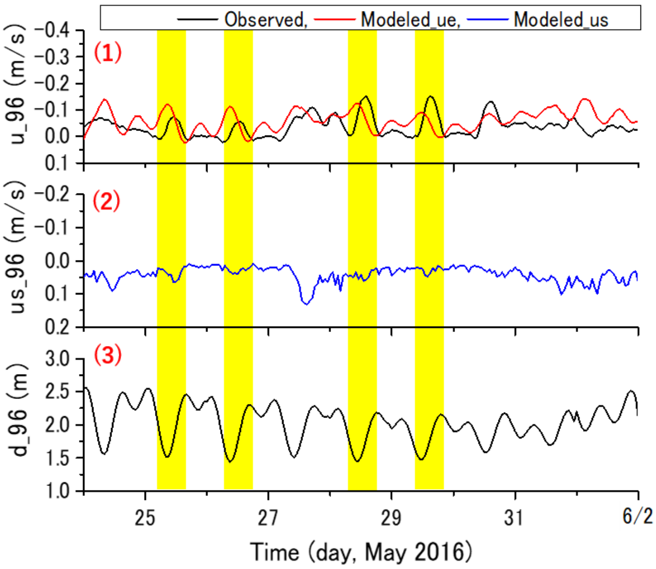

Figure 6.6: Time-series of (1) undertow velocity, (2) Stokes drift and (3) water depth at the location of $x = 96$ m for the low-energy wave case (May 24 - June 2, 2016).

Afterward, we figured out that the simulated undertow had been shifted faster than the observed for the case of low-energy wave as presented by yellow mark in panel 1 of Fig. 6.6. Black and red represent the observed and modeled undertow, respectively. To increase the quality of the model, the time difference of the peak velocities between the observed and modeled undertow was computed as summarized in Table 6.2. The mode, median and average of time difference were 5, 3 and 3.3 hours. respectively.

Table 6.2: Summary of time difference of the peak velocities between the observed and modeled undertow in low-energy wave case.

Time shift in the simulation (hour)							
Location	Time (day, May 2016)						
(x, m)	24	25	26	27	28	29	30
126	5	2	4	-	3	4	2
116	5	3	5	-	4	3	2
96	1	3	5	5	3	2	1
Mode	5						
Median	3						
Average	3.3						

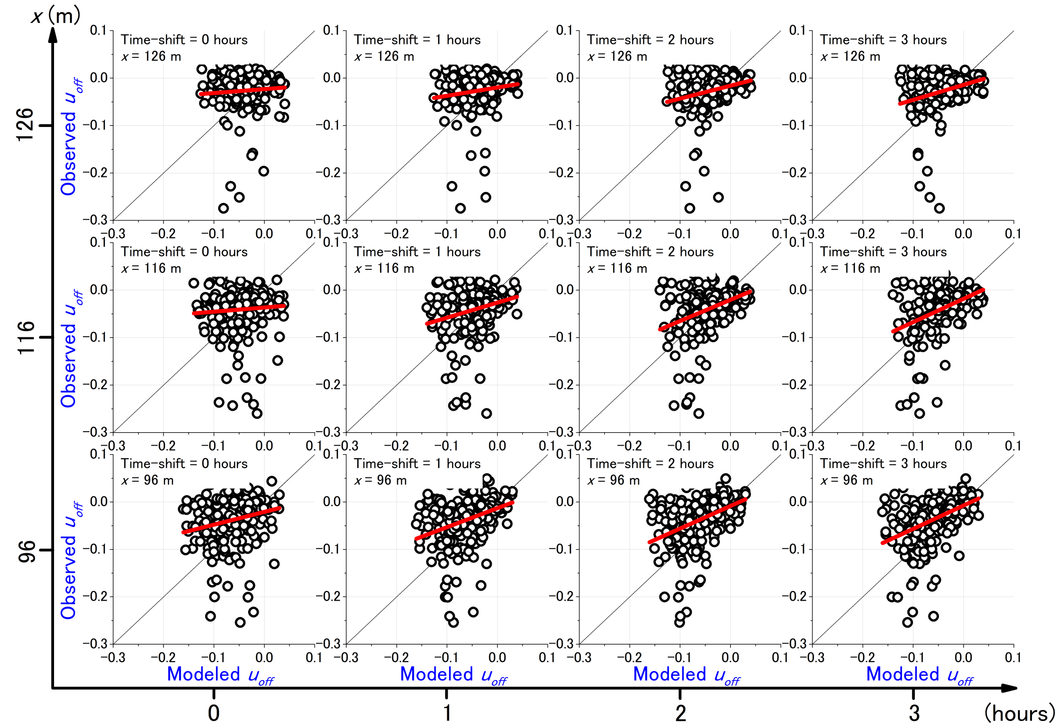

Figure 6.7: Changes of comparison of the observed and modeled undertow for the locations of $x = 96$, 116 and 161 m due to time-shif from 0 to 3 hours.

Then, the simulated undertow was shifted in the range of time difference from 0 to 5 hours to match the peak undertow velocity at the same. Shifting the modeled undertow backward resulted in better agreement with the observed as the skill and slope values increased, and the best results were at a time shift of 3 hours. After that, the skill and slope values decreased at 4 and 5 hours. Fig. 6.7 presents the effect of time shift on comparison of the observed and modeled undertow for the locations of $x = 96$, 116 and 161 m. Time-series of comparison of the observed and modeled undertow after time shift for 3 hours in case of low-energy wave was presented in Fig 6.8. Black and red refer to the observed and modeled undertow, respectively. The peaks of undertow velocity are now at the same period, but the simulation presents underestimated data. Fig. 6.9a and Fig. 6.9b indicate the values of skill and slope for each panel of Fig. 6.7. The locations of $x = 96$ and 116 are represented by black and red respectively.

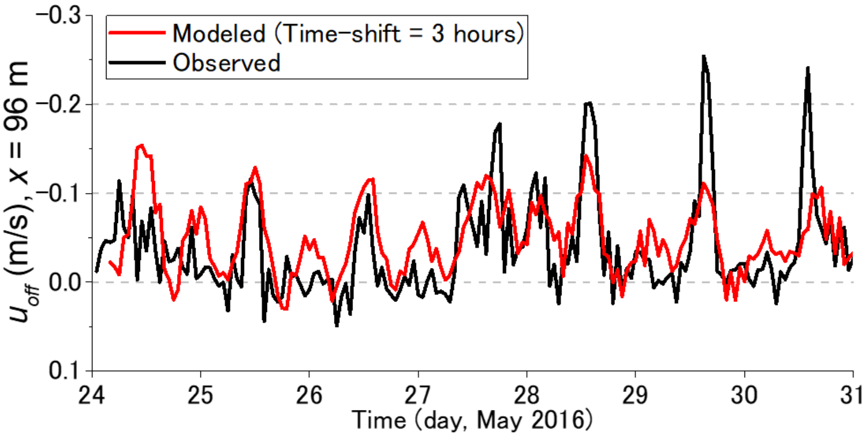

Figure 6.8: Time-series of modeled undertow after time shift for 3 hours in the case of low-energy wave.

Considering the peak of undertow velocity defined as $u_p > u_{rms}(0.1 \text{ m/s})$, we also quantified the performance of the model using the values of RMAE and RMSE as presented by Fig. 6.10a and Fig. 6.10b, respectively. It can be seen that at backward time shift of 3 hours for the modeled undertow gave the best results on the better quality for all considered locations, e.g. RMAE of the modeled undertow at $x = 116$ m changed form poor to fair quality when the the modeled undertow was shifted backward from 2 hours to 3 hours. The distributions of RMSE also gave the similar results (see more the values of RMAE and RMSE in Appendix F).

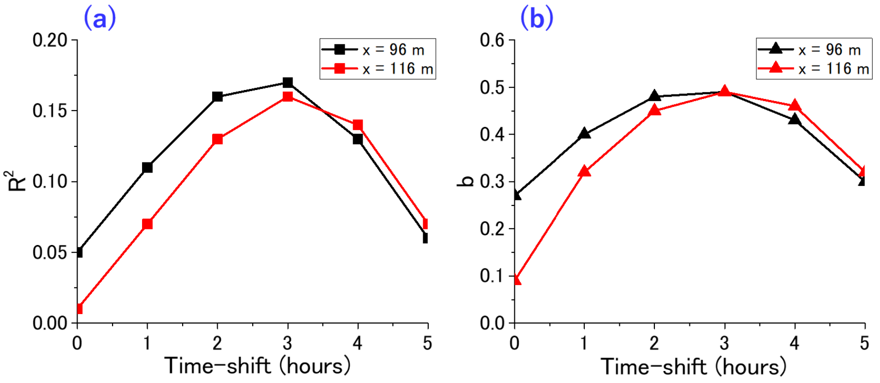

Figure 6.9: (a) skill and (b) slope values of the comparisons relating to time-shift for low-energy wave conditions.

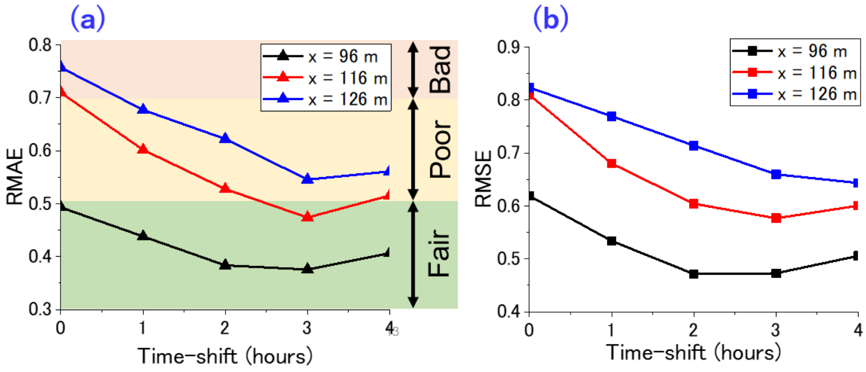

Figure 6.10: (a) RMAE and (b) RMSE of the comparisons relating to time shift for low-energy wave conditions.

The reason for time shift can be explained by using Fig. 6.11, which presents an extraction of the time-series of undertow velocity compared with the tide elevation, i.e. water level. The observed and modeled undertow (before shifted) are indicated by gray and red, respectively. The observed and modeled water level are represented by black and blue. The modeled water level was similar to the observed while the modeled undertow was simulated faster than it should be. The water level decreased from the maximum to MWL with the average rate of 3.7 mm/min. The variation of the modeled undertow was similar to the change of water level. The modeled undertow was periodically increasing when water level decreased from the maximum level to minimum level, and the undertow got to the peak when the water level decreased to about MWL (+0.66 m, D.L.) as indicated by horizontal dashed line, while the observed data was actually slower and the peak occurred at approximately the minimum water level. Therefore, the modeled undertow was underderestimated at the peak of the observed. It showed that the prediction of undertow in XBeach model is based on the water level and the undertow intensity subjects to the change of water level, as also supported by the laboratory study of Hadano et al. [33]. The prediction could well estimate undertow form the experimental data, but not for the undertow from the field data that was mainly induced by wave energy.

In addition to the deficiency of undertow prediction owing to the development from experimental data, this can explain that the development of undertow prediction between using experimental data and using field data affect the model to simulate the different results as time shift in here. Consequently, we decided to backward shift the model results for 3 hours.

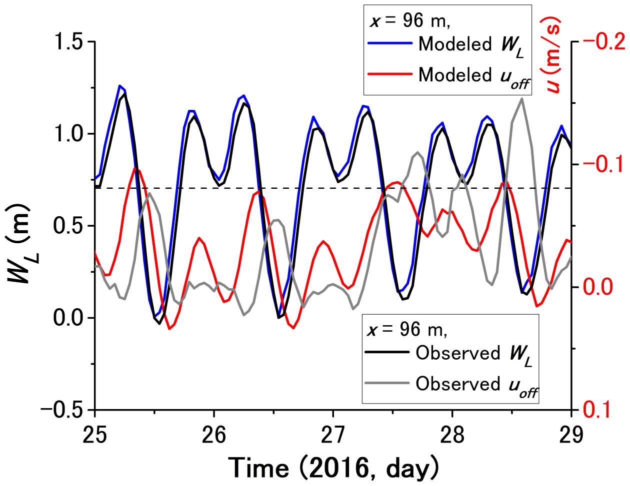

Figure 6.11: Effect of water level on undertow velocity.

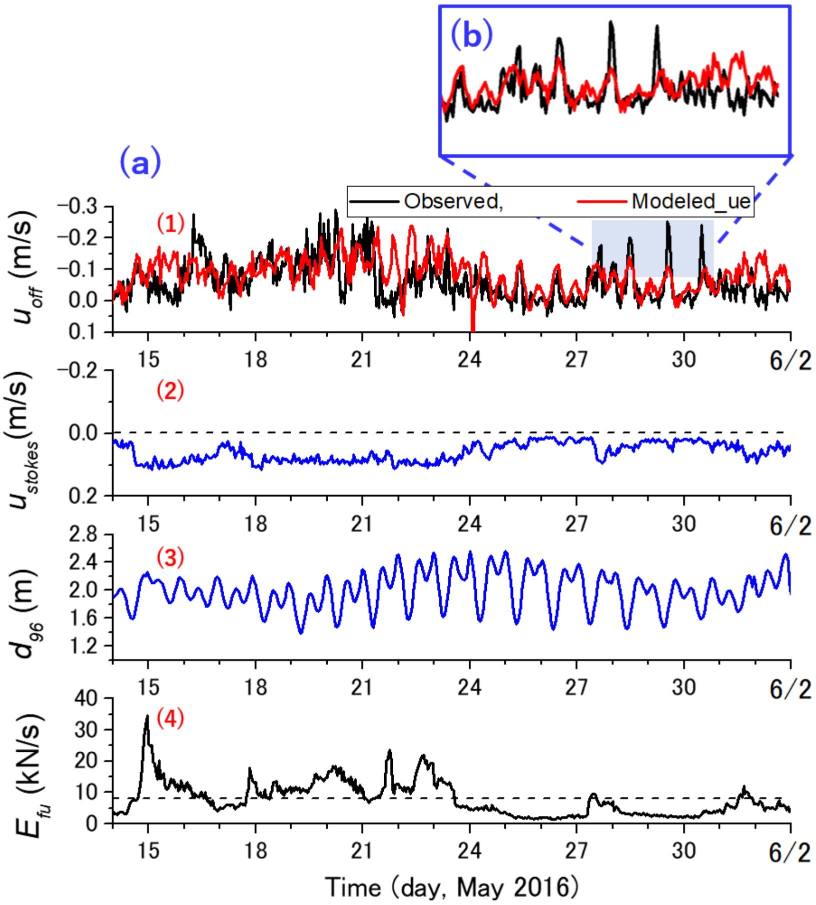

Figure 6.12: Time-series of (1) undertow velocity, (2) Stokes drift (3) water depth and (4) wave energy flux at the location of x = 96 m for the entire period.

For the case of high-energetic wave, the values of RMAE and RMSE did not much change when the modeled undertow was backward shifted in time (Appendix), even for time shift of 3 hours. Therefore, both cases of the modeled undertow had backward been shifted for 3 hours in time to proceed the same analysis and reach to the highest performance of undertow prediction in XBeach model before we merged the model results together. Time-series of undertow velocity after time shift for 3 hours, Stokes drift, water depth and wave energy flux were presented in Fig 6.12a. Black and red in panel 1 refer to the observed and modeled undertow, respectively. The peaks of observed and modeled undertow velocity are at the same period with the better values of skill, slope, RMAE and RMSE. However, the modeled undertow underestimated the observed as the peak velocity of undertow was lower (Fig. 6.12b).

6.3.3 Theoretically improving the simulated undertow

According to the explanation of undertow prediction in Sub-section 6.2.2, The equation of the Stokes drift can be expressed as Eq. 6.20 and the Stokes drift is accounted for the undertow prediction in the equation of Eulerian velocity (Eq. 6.19). It is different from the theoretical models of undertow, which basically consist of volume flux and water depth under wave trough level, but total water depth is used instead. If the Stokes drift increases by decreasing the value of total water depth, the undertow velocity will be increased. For this reason, we multiplied the total water depth with a coefficient (defined as λ) to increase the Stokes drift. The equation of Stokes drift becomes,

$$u'_S = \frac{E\cos\theta}{\rho C(\lambda h)}, \tag{6.21}$$

yields the new modeled undertow as,

$$u'_E = u_L - u'_S. \tag{6.22}$$

After that, we conducted the comparison between the observed and new modeled undertow (u'_{off}) together with using trial and error to obtain the optimal value of λ. The decision was based on the value of qualitative RMAE for defining λ. Fig. 6.13 shows the variation of RMAE due to the coefficient λ from 0.3 to 2 for the locations of $x = 96$, 116 and 126 m. Each color indicates each seaward location. The optimal value for the coefficient λ was 0.60±0.02.

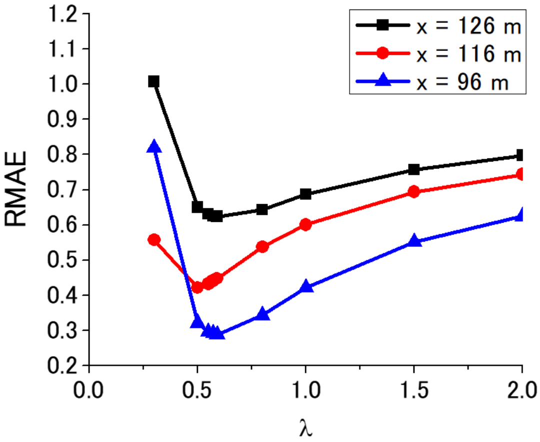

Figure 6.13: Variation of RMAE due to the coefficient λ from 0.3 to 2 for the locations of x = 96, 116 and 126 m.

At this moment, the recommended coefficient λ is 0.60±0.02 for comparing with this field data only. The undertow simulation will more be conducted to confirm the λ for using with field data in the future. Here, the comparison of the peaks between the observed and modeled undertow was given in Fig. 6.14. The modeled undertow in the cases of initial, after a time shift of 3 hours and after multiplying with λ = 0.60 are differently indicated by black, blue and red. The modeled undertow of multiplying with λ = 0.60 gave the better result with the better slope and skill values compared with the previous simulated results.

Fig. 6.15 also shows that RMAE decreased about 15.5% from the initial case after time shift of the simulated undertow and the adjustment of modeled undertow using λ resulted in the best with the good quality. RMAE decreased about 40% from the initial case in every considered location, e.g. the model result at the location of x = 96 m changed from fair to good quality with a decrease in RMAE of 40% from the initial. RMSE also have the same trend as RMAE which decreased to the lowest value for the case of using λ in all locations. RMAE and RMSE for the cases of modeled undertow after time shift and using λ = 0.60 are summarized in Table 6.3. Moreover, we show the percentage decrease in RMAE and RMSE are respectively as listed in Table 6.4 and Table 6.5.

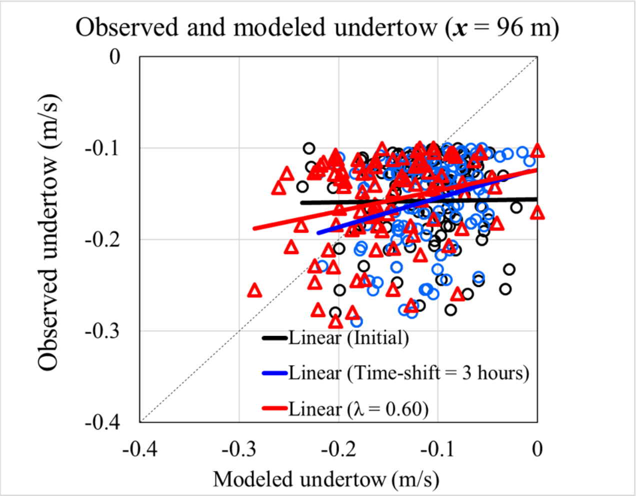

Figure 6.14: Comparison of the peaks between the observed and modeled undertow at the location of x = 96 m.

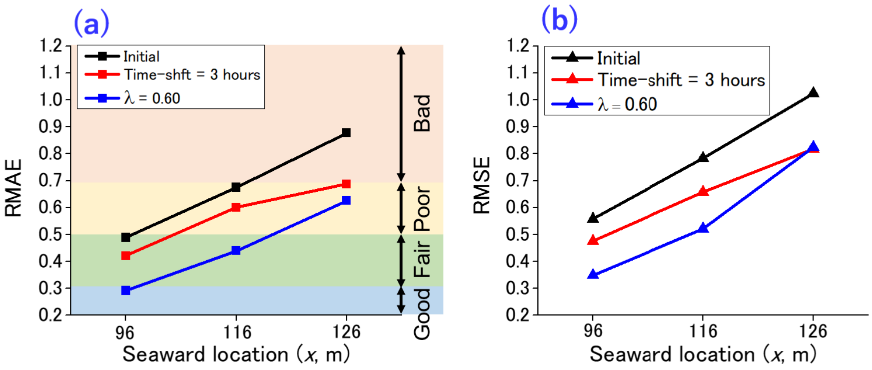

Figure 6.15: Spatial distributions of (a) RMAE and (b) RMSE at the locations of x = 96, 116 and 126 m for the modeled undertow in the different cases of initial (black), after a time shift of 3 hours (blue) and after multiplying with λ = 0.60 (red).

Table 6.3: Summary of RMAE and RMSE for the cases of modeled undertow after time shift and using λ = 0.60.

Case	RMAE			RMSE		
	x =126 m	**x** = 116 m	**x** = 96 m	**x** =126 m	**x** = 116 m	**x** = 96 m
Initial	0.877	0.675	0.489	1.024	0.784	0.558
Time-shift 3 hours	0.687	0.601	0.421	0.818	0.657	0.475
λ after time-shift	0.467	0.424	0.294	0.537	0.529	0.358

Table 6.4: Percentage decrease in RMAE for the cases of modeled undertow after time shift and using $\lambda = 0.60$.

Location	Time-shift = 3 hours		Adjusted by λ after time-shifting	
	%	Qualification	%	Qualification
x = 96 m	13.86	Fair	39.85	Good
x = 116 m	10.96	Poor	37.18	Fair
x = 126 m	21.64	Poor	46.69	Poor
Average	15.49	-	41.24	-

Table 6.5: Percentage decrease in RMSE for the cases of modeled undertow after time shift and using $\lambda = 0.60$.

Location	Time-shift = 3 hours	Adjusted by λ after time-shifting
	%	%
x = 96 m	14.84	35.82
x = 116 m	16.20	32.43
x = 126 m	20.11	47.54
Average	17.05	38.60

6.4 Discussion

To assess the accuracy of undertow prediction in XBeach model, the model was validated against the field undertow data, that was observed at HORS in 2016. The undertow simulations were separately run under high- and low-energetic wave conditions. The prediction of undertow velocity in high-energetic wave case was sensitive to the choices of roller parameter β and shallow water parameter $hmin$, with $\beta = 0.05$ and $hmin = 0.001$ m giving slightly better results than using default value. Moreover, turning rfb on resulted in the better simulated undertow than turning off for both cases of the undertow simulation.

With regard to the case of low-energetic wave, the significant issue was found on the time series of the comparison between the observed and modeled undertow. The modeled undertow was simulated faster than usual and its peak was at the different time. This brought about the underestimation of modeled undertow. The modeled undertow reached a peak when the water level decreased to about MWL, while the peak of observed undertow got to a peak when the water level decreased to about minimum level. This might be the effect of the development of undertow model by using laboratory data that leads to enlarge the error when applied to the realistic cases. After that, the modeled undertow was shifted for most matching time of 3 hours and then the peak of modeled undertow provided the better quality as shown by RMAE and RMSE.

Furthermore, the theoretical improvement was conducted by modifying the contribution of Stokes drift to undertow prediction with the coefficient of λ. The best model results were reproduced when $\lambda = 0.60$ was applied within the range of ± 0.02. In this Section, a guidance for estimating the coefficient of λ is given.

To compute a constant value of λ, we expected that it was the ratio of water depth under wave trough level to total water depth at a considered location. Because the total water depth in the equation of Stokes drift is compensated and then multiplied by the water depth under wave trough instead. Here, the demonstration of the coefficient λ is based on the average of the water depth and wave height as express by,

$$\lambda = \left\langle \frac{h_T}{h} \right\rangle = \frac{\langle h \rangle - \langle H/2 \rangle}{\langle h \rangle + \langle H/2 \rangle} \tag{6.23}$$

Table 6.6 indicates the average of water depth and wave height for the considered locations of $x = 96$, 116 and 126 m. As anticipated, the average of λ calculated by the Eq. 6.23 exactly equaled to the assumed λ of 0.60. Therefore, we can say that the coefficient of λ might be the ratio of water depth under wave trough level to total water depth. Applying this λ when comparing with the field data caused the modeled undertow to have a better quality.

Table 6.6: Average of water depth and wave height for the considered locations of $x = 96$, 116 and 126 m.

Location (x, m)	126	116	96
$\langle h \rangle$	2.91	2.52	1.90
$\langle H \rangle$	1.20	1.20	1.20
$\langle h_T \rangle$	2.31	1.93	1.30
$\langle h_T \rangle / \langle h \rangle$	0.66	0.62	0.52
$\langle \langle h_T \rangle / \langle h \rangle \rangle$	0.60		

Chapter 7

XBeach (X Release)

XBeach model has continuously been updated to extend the range of application for a variety of beach features, and there is a number of investigations into the performance of XBeach, where the effect of model coefficients for predicting morphological changes has found more attention [35] [93]. For example, the most skillful predictions under three extreme erosion events at Hasaki coast in Japan were obtained when the time-averaged flows due to wave skewness and asymmetry, $facua$, of 0.0 was used. The correlation between $facua$ and sediment volume changes was suggested to take into account for further XBeach improvements [93]. Therefore, to improve XBeach model, not only the adjustable coefficients, but the equations of each considered individual term should also be discussed.

In this study, we focused on the undertow prediction in XBeach, which is one of the important hydrodynamic mechanisms for sediment transport [83]. Whether high- or low-wave energy conditions, the cumulative effects of undertow cause extensive changes in the coastal bathymetry [11]. Recently, the betterment of undertow prediction was demonstrated by modifying the wave-roller dissipation coefficient, that is spatially variate. However, despite the improvements for high-wave-energy (hereafter HWE) conditions, the XBeach still performs poorly in predicting undertow under low-wave-energy (LWE) conditions [75].

Thus, this study aims to improve the XBeach's undertow prediction response under LWE conditions. The capability of the model to reproduce undertow current was evaluated using the field observation datasets at the Hasaki coast, that is, HC16. The model coefficients were calibrated to obtain the best prediction of undertow. However, the undertow simulation needs a modification for increasing performance, and a new coefficient of water depth is suggested. Both the temporal and spatial undertow results were analysed and discussed.

7.1 Updated functions in XBeach model

After the first version of XBeach model was released, the XBeach team have improved the model to widen its application areas. For example, in the Risc-Kit project [104], since XBeach was applied to translate offshore events that affect the coastal concrete structures for a variety of beach features, the examination, improvement and validation of the numerical and physical schemes had been conducted. Finally, the XBeach version Kingsday was achieved. The new (and modified) physical formulations, increased boundary conditions, improved numerical scheme, skillbed and bug fixes are summarized in Table 7.1.

Table 7.1: Updating of XBeach model.

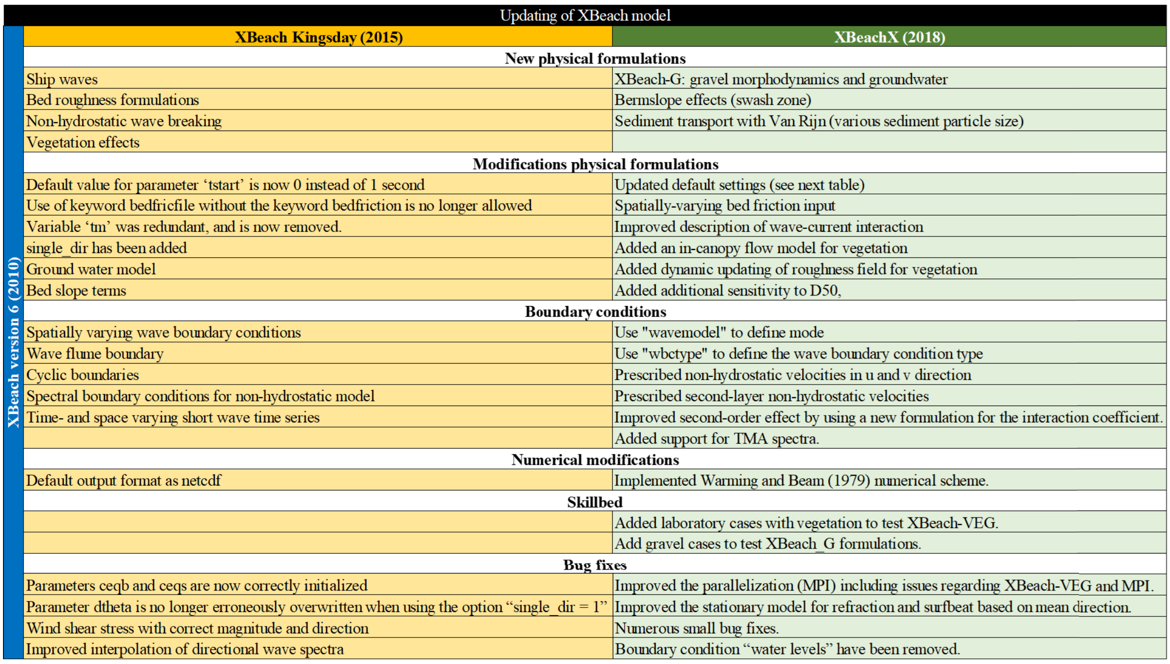

Updating of XBeach model

	XBeach Kingsday (2015)	XBeachX (2018)
XBeach version 6 (2010)	**New physical formulations**	
	Ship waves	XBeach-G: gravel morphodynamics and groundwater
	Bed roughness formulations	Bermslope effects (swash zone)
	Non-hydrostatic wave breaking	Sediment transport with Van Rijn (various sediment particle size)
	Vegetation effects	
	Modifications physical formulations	
	Default value for parameter ‘tstart’ is now 0 instead of 1 second	Updated default settings (see next table)
	Use of keyword bedfricfile without the keyword bedfriction is no longer allowed	Spatially-varying bed friction input
	Variable ‘tm’ was redundant, and is now removed.	Improved description of wave-current interaction
	single_dir has been added	Added an in-canopy flow model for vegetation
	Ground water model	Added dynamic updating of roughness field for vegetation
	Bed slope terms	Added additional sensitivity to D50,
	Boundary conditions	
	Spatially varying wave boundary conditions	Use "wavemodel" to define mode
	Wave flume boundary	Use "wbctype" to define the wave boundary condition type
	Cyclic boundaries	Prescribed non-hydrostatic velocities in u and v direction
	Spectral boundary conditions for non-hydrostatic model	Prescribed second-layer non-hydrostatic velocities
	Time- and space varying short wave time series	Improved second-order effect by using a new formulation for the interaction coefficient.
		Added support for TMA spectra.
	Numerical modifications	
	Default output format as netcdf	Implemented Warming and Beam (1979) numerical scheme.
	Skillbed	
		Added laboratory cases with vegetation to test XBeach-VEG.
		Add gravel cases to test XBeach_G formulations.
	Bug fixes	
	Parameters ceqb and ceqs are now correctly initialized	Improved the parallelization (MPI) including issues regarding XBeach-VEG and MPI.
	Parameter dtheta is no longer erroneously overwritten when using the option “single_dir = 1”	Improved the stationary model for refraction and surfbeat based on mean direction.
	Wind shear stress with correct magnitude and direction	Numerous small bug fixes.
	Improved interpolation of directional wave spectra	Boundary condition “water levels” have been removed.

While the XBeach version Kingsday was being validated, a new branch of the XBeach model, called XBeach-G was also developed for steep gravel coasts [53] [54]. A correction term of non-hydrostatic pressure was included in the non-linear shallow water equation [88], allowing phase-resolving approach for infragravity and incident-band waves in XBeach-G.

In 2017, a new release of XBeach, XBeach verion X, was issued by Deltares, IHE Delft and TU Delft. XBeachX release was named to celebrate the 10th anniversary of the first presentation of the code at the 10th International Workshop on Wave

Hindcasting and Forecasting and Coastal Hazard Symposium in Hawaii on November 11, 2007 [82]. XBeachX includes the XBeach-G, and performance updates along with many new features based on ongoing research results funded by JIP, EU and market projects. Especially, the second-order upwind scheme was corrected according to the study of Warming and Beam in 1976 [10] for reducing the numerical error owing to steepening of wave-group propagation. Table 7.2 is the list of updating default settings for XBeach version Kingsday and X summarized by the author. Not only Warmbeam scheme, but also the default value and range of each parameter were changed. Yet some changes are not listed in the manual, where the users should check while calibrating for their simulations.

Table 7.2: Default settings for the XBeach Kingsday and X release versions.

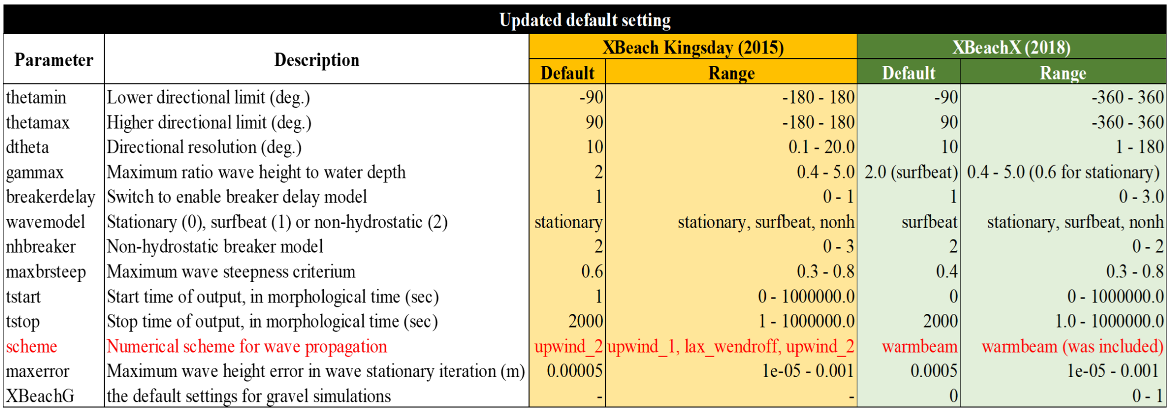

Updated default setting					
Parameter	Description	XBeach Kingsday (2015)		XBeachX (2018)	
		Default	Range	Default	Range
thetamin	Lower directional limit (deg.)	-90	-180 - 180	-90	-360 - 360
thetamax	Higher directional limit (deg.)	90	-180 - 180	90	-360 - 360
dtheta	Directional resolution (deg.)	10	0.1 - 20.0	10	1 - 180
gammax	Maximum ratio wave height to water depth	2	0.4 - 5.0	2.0 (surfbeat)	0.4 - 5.0 (0.6 for stationary)
breakerdelay	Switch to enable breaker delay model	1	0 - 1	1	0 - 3.0
wavemodel	Stationary (0), surfbeat (1) or non-hydrostatic (2)	stationary	stationary, surfbeat, nonh	surfbeat	stationary, surfbeat, nonh
nhbreaker	Non-hydrostatic breaker model	2	0 - 3	2	0 - 2
maxbrsteep	Maximum wave steepness criterium	0.6	0.3 - 0.8	0.4	0.3 - 0.8
tstart	Start time of output, in morphological time (sec)	1	0 - 1000000.0	0	0 - 1000000.0
tstop	Stop time of output, in morphological time (sec)	2000	1 - 1000000.0	2000	1.0 - 1000000.0
scheme	Numerical scheme for wave propagation	upwind_2	upwind_1, lax_wendroff, upwind_2	warmbeam	warmbeam (was included)
maxerror	Maximum wave height error in wave stationary iteration (m)	0.00005	1e-05 - 0.001	0.0005	1e-05 - 0.001
XBeachG	the default settings for gravel simulations	-	-	0	0 - 1

7.2 Undertow modeling in XBeachX

7.2.1 Model set-up

In this research, the latest release of XBeach, version X (1.23.5840), was implemented in two dimensions with a 5 m grid resolution along the cross-shore section (500 m) and 10 m grid resolution on the alongshore section (100 m). The seabed profile of May 24 of HC16 was used as the initial bathymetry condition. At the offshore boundary, JONSWAP type wave conditions were specified using the hourly time-varying wave spectra and direction observed at the pier end ($x = 380$ m). The wave breaking formulation of Daly et al. (2010) [18] was used, and the first and second thresholds were set as 0.4 to fully breaking and 0.1 for stop breaking. The hourly tidal signals were also created using the observed data at the same location. These field datasets are described in Section 3.2. The model was run under the default surfbeat mode, with each point-data resulting at every 5 min.

7.2.2 Tuning model coefficients

Based on several model-sensitivity tests to obtain better comparisons between the observed and modeled wave height, water level, and undertow velocity, the important model coefficients subject to change were: 1) a Chezy coefficient of 60 was applied as dimensionless friction, corresponding to a typical Manning value of 0.02 s/m$^{1/3}$ for the median sediment diameter of 0.18 mm at the Hasaki coast, 2) the wave surface slope in roller energy balance was implemented (=1), and 3) the slope of breaking wavefront, β_r, which accounted for the wave-roller dissipation, was applied at the lowest value of 0.05 for the LWE conditions. Other unmentioned parameters were left to default.

7.3 Modification of undertow prediction I: water depth

In the XBeach surfbeat mode, the mean off-shore directed current, i.e., undertow is solved in the form of Eulerian velocity (Fig. 7.1), u_E, as Eq. 6.19. This equation indicates two important factors of the cross-shore component of Lagrangian velocity, u_L, and Stokes drift, u_S.

From Eq. 6.20, the wave energy flux, E_f, and the total water depth, h, dominate the u_S velocity. Here, the equation was modified as given by,

$$u_S = \frac{E\cos\theta}{\rho h C \lambda}. \tag{7.1}$$

where ρ is the water density, θ_s is the wave angle, C is the wave celerity, and λ is a new coefficient of water depth. The nonlinear shallow water equations (NSWE) solves the depth-averaged u_L as follows:

$$\begin{aligned}\frac{\partial(u_L)}{\partial t} + u_L\frac{\partial(u_L)}{\partial x} + v_L\frac{\partial u_L}{\partial y} - f v_L - \nu_h\left(\frac{\partial^2 u_L}{\partial x^2} + \frac{\partial^2 u_L}{\partial y^2}\right)& \\ = -\frac{\tau_{bx}}{\rho h} - g\frac{\partial W_L}{\partial x} + \frac{F_x}{\rho h \lambda}&,\end{aligned} \tag{7.2}$$

$$\begin{aligned}\frac{\partial(v_L)}{\partial t} + u_L\frac{\partial(v_L)}{\partial x} + v_L\frac{\partial v_L}{\partial y} - f u_L - \nu_h\left(\frac{\partial^2 v_L}{\partial x^2} + \frac{\partial^2 v_L}{\partial y^2}\right)& \\ = -\frac{\tau_{by}}{\rho h} - g\frac{\partial W_L}{\partial y} + \frac{F_y}{\rho h \lambda}&,\end{aligned} \tag{7.3}$$

$$\frac{\partial W_L}{\partial t} + \frac{\partial h u_L}{\partial x} + \frac{\partial h v_L}{\partial y} = 0. \tag{7.4}$$

where t is time, x and y are respectively the cross-and longshore coordinates, v_L is alongshore component of Lagrangian velocity, ν_h is the horizontal viscosity, τ_{bx} represents the bed shear stress, g is the gravitational acceleration, W_L is the water level (SWL), and F represents the wave forces due to the short wave-action and wave-roller energy dissipation.

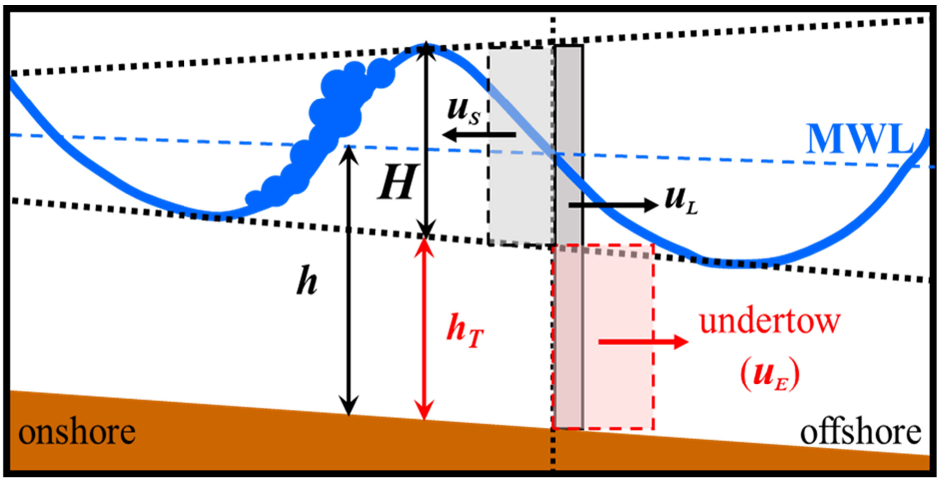

Figure 7.1: Schematic of Lagrangian velocity and Stokes drift associated with the generation of undertow.

In an attempt to increase the accuracy of undertow prediction, the modification was focused on the water depth factor, that dominates under-tow under LWE conditions. Theoretically, the undertow is driven by the water depth under the wave trough level, h_T, as shown in Fig. 7.1 [36] [63]. However, according to the Stokes drift (Eq. 7.1), the total water depth in the equation covers the entire water column from the seabed to water surface, the shoreward current velocity is, thus, being considered, and this may increase the error in predicting undertow. To neglect this shoreward current, we introduced a spatially varying coefficient of water depth in Eq. 7.1, that is λ, indicating the normalized value of h_T/h, calculated by

$$\lambda = \frac{h_T}{h} = \frac{h - (H/2)}{h}. \tag{7.5}$$

7.4 Undertow simulation under LWE conditions

7.4.1 Field datasets during LWE

As we considered the undertow during LWE condition, the seabed profile responsible for that period, i.e., May 24 and June 2, 2016, is presented in Fig 7.2. The shoreline was defined at the mean water level (MWL) at Hasaki coast of +0.65 m relative to the datum level (D.L.) at the site (T.P. -0.68 m). The water depth, h, was measured from the water surface level to the seabed. Two sandbars appeared around x = 60 and 190 m. Between the inner and outer bars, the depth at the trough (x = 140 m) was 4.20 m below the MWL. At the end of the observation period, the sediment accretion occurred from the shoreline to x =100 m and in the trough region. The inner sandbar crest was raised by approximately 1 m. However, no change was observed from x = 150 m to the farther locations.

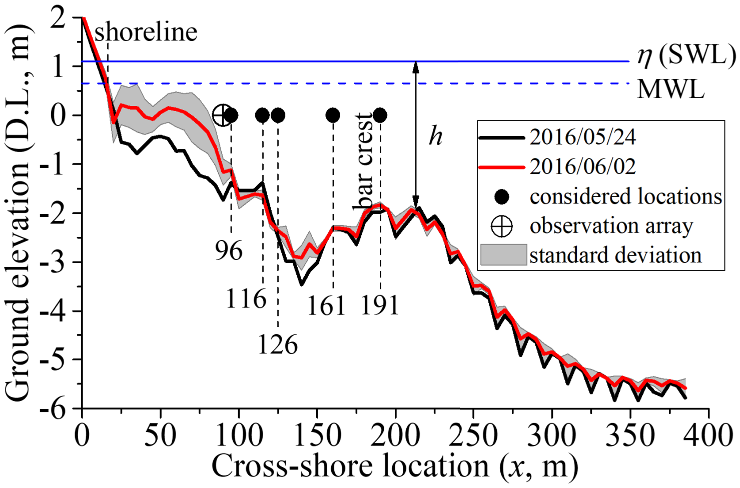

Figure 7.2: Seabed profile change during the LWE conditions.

During May 14–23, high-wave conditions continued with the wave height exceeding the average value of the whole observation period of 1.01 m. From May 24, the situation became calm and the wave height was mostly below the average. Figs. 7.3a-7.3b shows the time-series data of the wave height with wave period, and wave direction during the LWE period, respectively. The averages of wave height and wave period were 0.74 m and 7.1 s with a range of 0.47 m $< H_s <$ 1.42 m and 4.4 s $< T_s <$ 9.0 s, respectively. The wave direction changed within a range of 12.7° $< \theta_s <$ 41.8°, which did not vary much compared to the high-wave conditions or during an incident wave on May 27 (θ_{s-min} = -23.1°).

The temporal water level and the cross-shore currents at the five locations, i.e., x = 96, 116, 126, 161, and 191 m, are presented in Figs. 7.3c–7.3d, respectively. In the panel (d), the vertical line indicates the current magnitude and the horizontal dashed line indicates the considered location and distinguishes direction; the data below and above the dashed line refer to the onshore- and offshore-ward currents (i.e., the undertow), respectively. The blanks are missing data. The red dashed box indicates the analyzed period (May 28–30) that is discussed in Section 7.4.3.

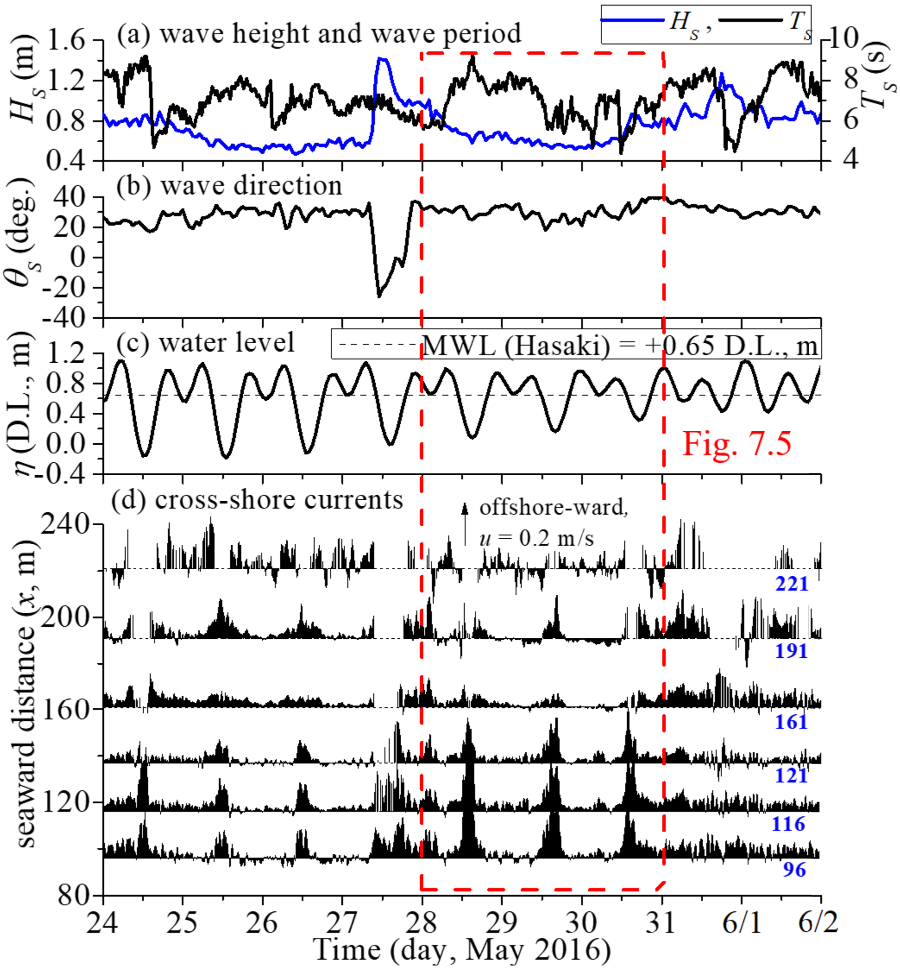

Figure 7.3: Observed time-series data during LWE of HC16: (a) significant wave height and wave period, (b) wave direction, (c) water level, and (d) cross-shore currents.

As shown in Fig. 7.3d, a strong undertow occurred periodically with the decreasing water level. This finding is significant for the undertow characteristic under the

LWE condition, where the undertow was induced by the change in water level and the remaining energy from the wave dissipation. Moreover, the differences in water depths along the seaward locations created spatial variation in the undertow, indicating that the strongest undertow was measured at the smallest water depth of $x = 96$ m. Then, it became weaker with increasing water depth at farther offshore locations (from $x = 96$–161 m) and was weakest in the trough region of $x = 161$ m. However, a stronger undertow was again induced at a smaller water depth over the outer sandbar crest ($x = 191$ m).

7.4.2 Wave comparisons under LWE

To evaluate the performance of the wave transformation in XBeach, the modeled waves were verified against the field wave measurements, provided by HORS. Three wave datasets observed in the surf zone at the locations of $x = 303$ (offshore), 145 (sandbar trough), and 40 m (nearshore), which located within the distance from the boundary at $x = 380$ m to shoreline position at $x = 15$ m, were used for testing. The wave comparisons are shown in Fig. 7.4. The black, gray, blue, and red colors indicate the observed, DF, MF-1, and MF-2 simulated wave heights, respectively. The relative mean absolute error (RMAE) proposed by Van Rijn [105] was used to qualify the wave simulations. With the same colors and qualification method, the undertow validation is also discussed in the later section. Note that the RMAEs for wave and undertow evaluations were different.

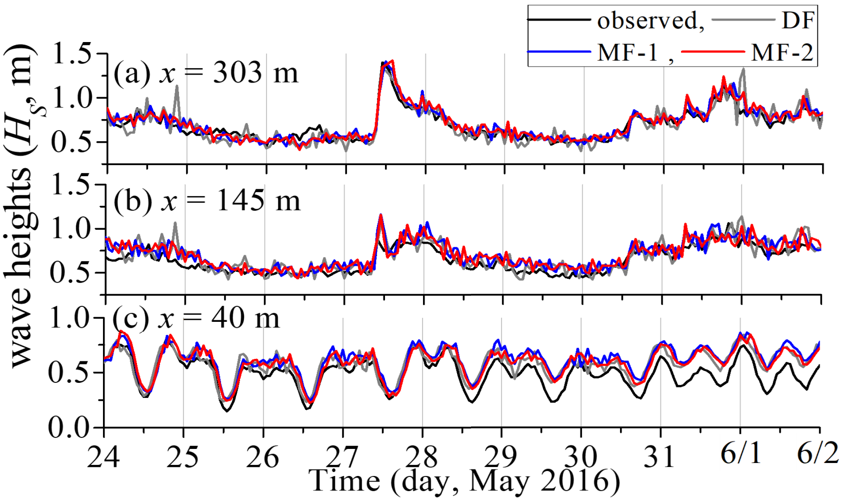

Figure 7.4: Time-series data of the observed (black), XBeach DF (gray), MF-1 (blue), and MF-2 (red) modeled wave heights at $x =$ (a) 303, (b) 145, and (c) 40 m.

In Fig. 7.4, all of the modeled wave heights using DF, MF-1, and MF-2 simulations agreed well with the observations, and the RMAE of each case is similar. Especially at x = 303 and 145 m, the RMAEs for MF-2 are 0.03 and 0.07, respectively. Although the results in panel (c) show an overestimation at x = 40 m from the midday of May 28 to the end on June 30, 2016, the variation coincides with the observed coincides with the observed wave with the RMAE in an acceptable qualification of 0.18 (fair).

7.4.3 Temporal undertow comparisons under LWE

The hourly averaged undertows response under LWE conditions between the observation and XBeach simulations were compared as presented in Fig. 7.5. Panel (a)-(e) show the undertow comparisons at five locations of x = 191, 161, 126, 116, and 96 m, respectively, and panel (f) shows the comparisons of hourly water level from May 28 to 30, 2016.

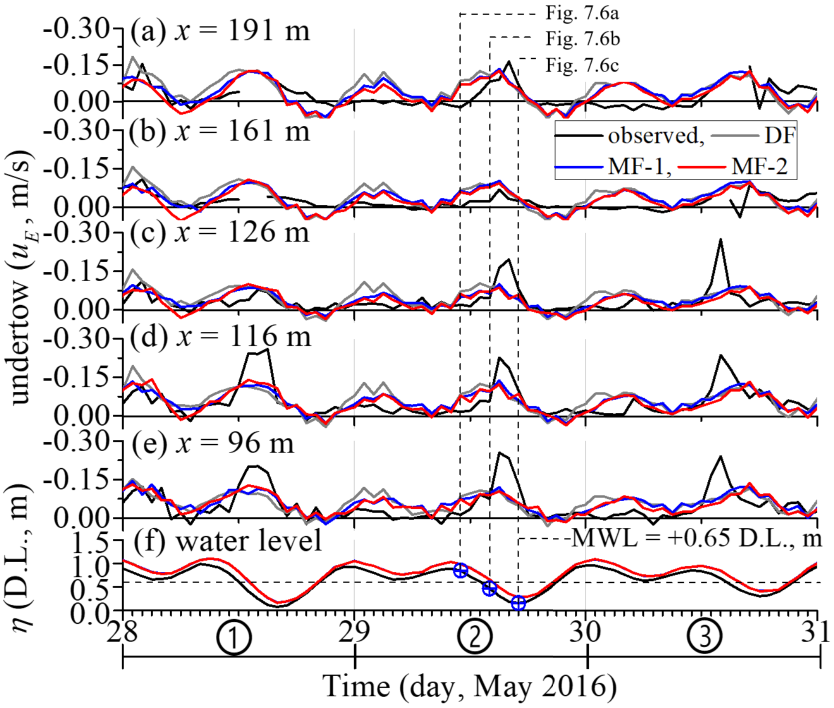

Figure 7.5: Time-series data of undertow during May 28–31, 2016, at five locations of x = (a) 191, (b) 161, (c) 126, (d) 116, and (e) 96 m, and (f) water level for the observed (black), XBeach DF (gray), MF-1 (blue), and MF-2 (red).

From the figure, the XBeach DF undertow shows an overestimation during high tide and an underestimation during low tide, yielding to a high value of RMAE $>$ 1.0 (bad qualification). Thus, the modifications of undertow prediction using λ were done for dealing with this inaccuracy. Since λ limits the generation of undertow under h_T level, an increase in simulated undertow velocity is expected here, though the results of MF-1 and MF-2 are still not much different from the DF case. However, interestingly, the less overestimated undertow during high tide, i.e., at the beginning of each day, is presented at all locations for both MF-1 and MF-2, resulting in a better RMAEs $>$ 0.7 as compared to DF.

Because of the selection of the five cross-shore locations for discussing temporal undertow velocity, some meaningful undertow data in between those locations were unseen. Therefore, the evaluation of the performance of undertow simulations were continued by examining the fixed-time undertow distributions and discussed in the next section.

7.4.4 Spatial distributions of undertow under LWE

The capability of the XBeach to predict the spatial distributions was investigated by comparing the simulated undertow with the observed data at a higher time-resolution of 20-min averaging for every cross-shore location. Fig. 7.6a– 7.6c illustrates the undertow spatial distributions at the specific high, mean, and low water levels on May 29, respectively. The timings are indicated by the vertical dashed lines in Fig. 7.5.

From the water level near MWL (Fig. 7.6b) to the low water level (Fig. 7.6c), the observed undertow velocity slightly decreased at every location with the peak of -0.11 m/s, that is still critical to the sediment movement at the Hasaki coast. While the DF and MF-1 simulations show the undertow underestimation, the MF-2 could well predict the undertow and present a similar distribution to the observed data. Note that the similar distributions at each tide were also given on May 28 and 30.

Regarding the characteristics of undertow spatial distribution explained above, the performance of the undertow simulations depend on the tidal elevation. Thus, we summarized its performance by comparing the spatially-varied undertow velocity against the observed data, and averaging the time series RMAE based on three tidal cycles during May 28–30 (Fig. 7.5, (1)-(3)).

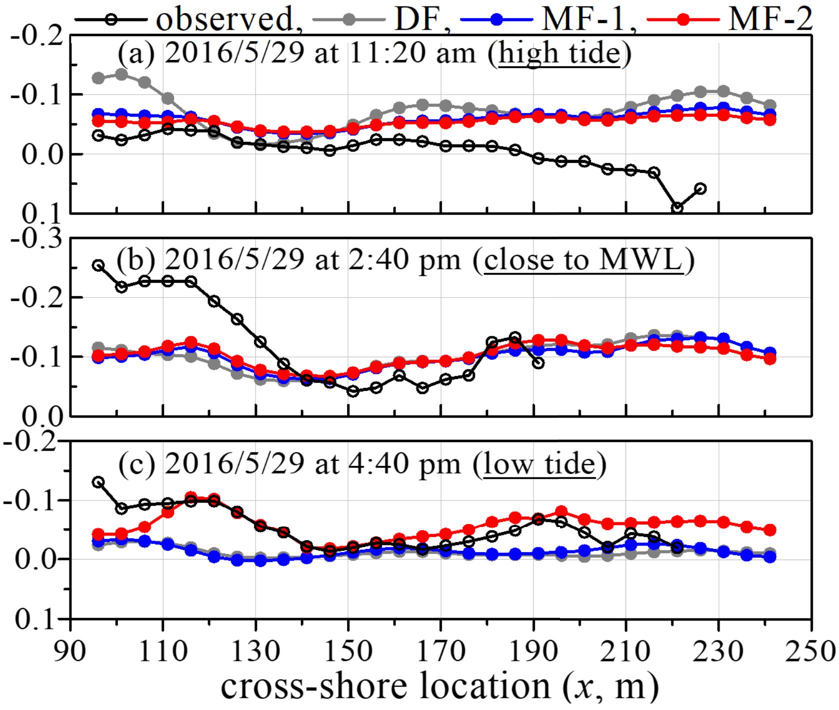

Figure 7.6: Spatial distributions of undertow on May 29 at (a) high tide, (b) close to MWL, and (c) low tide of 0.85, 0.50, and 0.16 m, D.L., respectively.

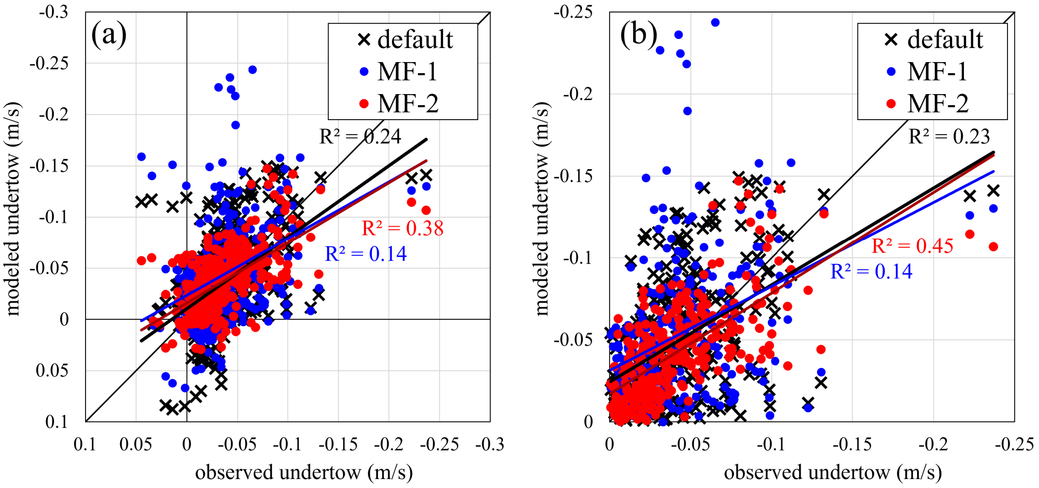

Figure 7.7: Observed vs. DF, MF-1 and MF-2 modeled undertow current velocities and regression lines response under LWE (a) with and (b) without shore-ward velocity value.

The comparison between the observed and DF, MF-1 and MF-2 modeled undertow velocities results response under LWE conditions are presented in Fig. 7.7.

Although the regression lines are similar with the overestimated and underestimated undertow at the higher and lower velocity of approximately -0.05 m/s, respectively, the undertow data are less scattered, and gathered near the ideal line for MF-2. Moreover, the improvement of undertow prediction was increased noticed by the increase in R-square values by 14% and 22% when the shore-ward velocity was considered (Fig. 7.7a) and unconsidered (Fig. 7.7b), respectively.

Figure 7.8a shows the similar curves of RMAE score with the increasing of accuracy from DF, MF-1, to MF-2 simulations, respectively. When the water level was reducing, the pressure gradient of water surface becomes maximum at the MWL and intensifies the undertow. Yet, this peak undertow could not be well predicted as the vertical dotted lines represent the top 2 lowest accuracy at 2^{nd} and 10^{th} hour. Further investigation is needed at this point. The last one at 20^{th} hour was not considered as it was mostly onshore-ward velocity. When the pressure gradient of water surface was approximately zero at the high and low tides, the undertow was mainly affected by wave mass flux only and well predicted with the highest ac-curacy as indicated by vertical dashed lines at 8^{th} and 16^{th} hour for high and low water levels, respectively. Here, given the proposed λ coefficient, the wave mass flux of both E_f (Eq. 7.1) and F (Eq. 7.2–7.3) were correctly adjusted to neglect the effect of shoreward mass flux and generate the undertow under the wave trough level.

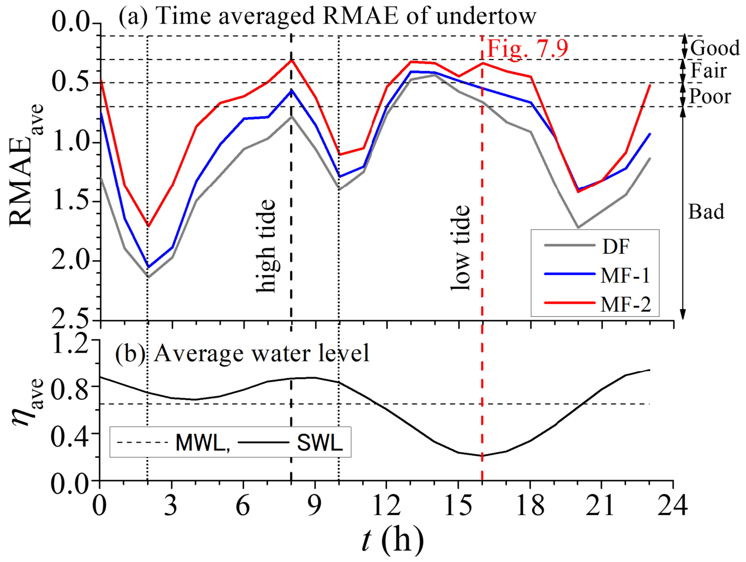

Figure 7.8: Time averaged values on three tidal cycle (Fig. 7.5, (1)-(3)) during May 28–30, 2016: (a) RMAE of XBeach DF (gray), MF-1 (blue), and MF-2 (red) simulated undertow results, and (b) observed water level.

Considering the improvement of simulated undertow at the low tides during May 28–30, that is, strong undertow, the RMAEs were temporally averaged for each cross-shore location as shown in Fig. 7.9. Although the RMAE of DF and MF-1 reveals the inaccuracy due to unpredictable undertow especially at bar trough (x = 146 m) and bar-offshore (x = 221 m) regions, the significant improvement of the undertow simulation was finally achieved using MF-2. The qualification shifted from bad to fair, with the average RMAE value decreasing from 1.057, 0.857, to 0.415 for the DF, MF-1, and MF-2, respectively.

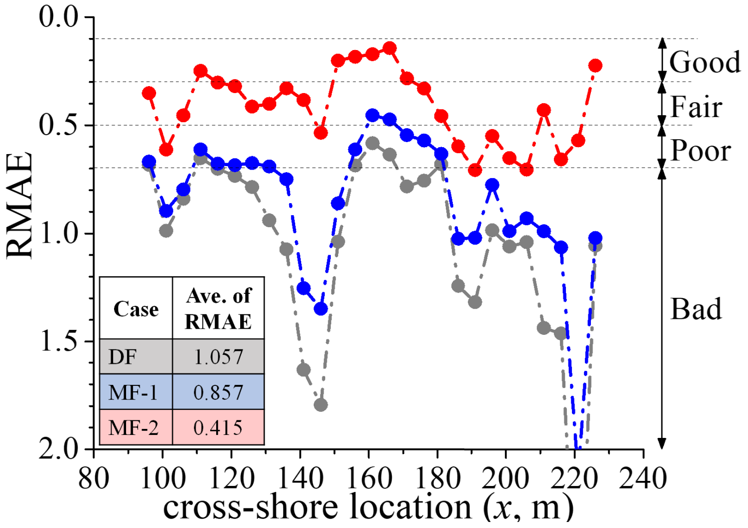

Figure 7.9: Spatial RMAE values of undertow simulation at low tide on each day during May 28-30.

7.5 Summary of undertow results under HWE conditions

Furthermore, the MF-2 modeled undertow under HWE conditions were analyzed using the same procedure as LWE, and their comparison results are summarized in Table 7.3. Even though the water-level change due to tides is a minor effect on the undertow, the undertow comparison is classified into five groups (A, B, C, D and E) based on tide condition and water-level elevation to provide detailed analysis. Interestingly, the improvement of undertow results are achieved with the increase in R-square values from group A to E by 39%, 33%, 57%, 17% and 31%, respectively. However, the underestimation errors were found at the strong undertow current velocity. The comparison result of group A (pink mark) is presented in Fig. 7.10.

Table 7.3: Default settings for the XBeach Kingsday and X release versions.

Condition	High water level	Mean sea level	Low water level
Neap tide	A (2, 4, 6, 7, and 23 h) - Skill = 0.00 → 0.39 (39%) - **underestimation**	B (1, 3, 5, and 8 h) - Skill = 0.15 → 0.48 (33%) - **underestimation**	
Spring tide	C (9, 13, 14, 17, 18, and 22 h) - Skill = 0.04 → 0.61 (57%) - **underestimation**	D (10, 12, 15, 19, and 21 h) - Skill = 0.04 → 0.21 (17%) - overestimation	E (11, 16, and 20 h) - Skill = 0.05 → 0.36 (31%) - **underestimation**

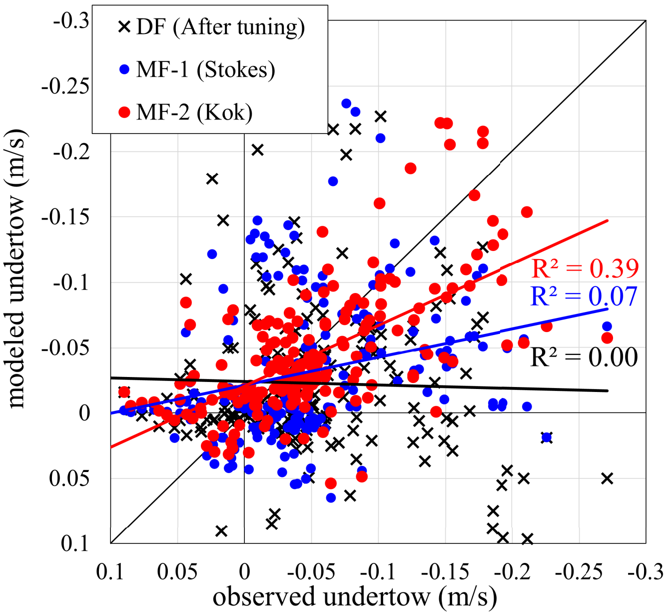

Figure 7.10: Observed vs. modeled XBeach DF (black), MF-1 (blue), and MF-2 (red) undertow velocities response HWE for data group A.

Figure 7.10 shows the comparison between the observed, XBeach DF (black), MF-1 (blue), and MF-2 (red) undertow velocity for classified group A undertow data. From no correlation in DF simulation, MF-1 and MF-2 results in the increase in performance for predicting undertow, with the R-square values of 0.07 and 0.39, respectively. The bias in prediction (slope of regression line) is also decreased and smallest for MF-2. Therefore, our approach to improving undertow prediction by using the water depth coefficient (MF-2) yield better modeled-undertow results than DF for both LWE and HWE conditions. More results and discussions are provided in the Section 7.6.2, that includes undertow results from another modification.

7.6 Modification of undertow prediction II: wave roller

From Figure 7.10, the observed shore-ward and undertow velocities were over- and underestimated, respectively. The overestimation might be caused by some unchecked model coefficients, e.g., breaking index and viscosity, and this should be later investigated. For the modeled undertow, the increase in velocity, the larger error and bias. Since the undertow under HWE was generally governed by the wave energy flux owing to wave breaking and roller, we first checked the wave-breaking zone by using the equation of wave-breaking depth [8] to confirm that if the strong undertow occurred at this zone. The equation is given as,

$$h_b = \frac{1}{g^{1/5}\gamma^{4/3}} \left(\frac{H_o^2 c_o \cos\theta}{2} \right)^{2/5}. \tag{7.6}$$

where γ is 0.8, H_o is the offshore wave height at $x = 380$ m, c_o is wave celerity, and θ is wave angle.

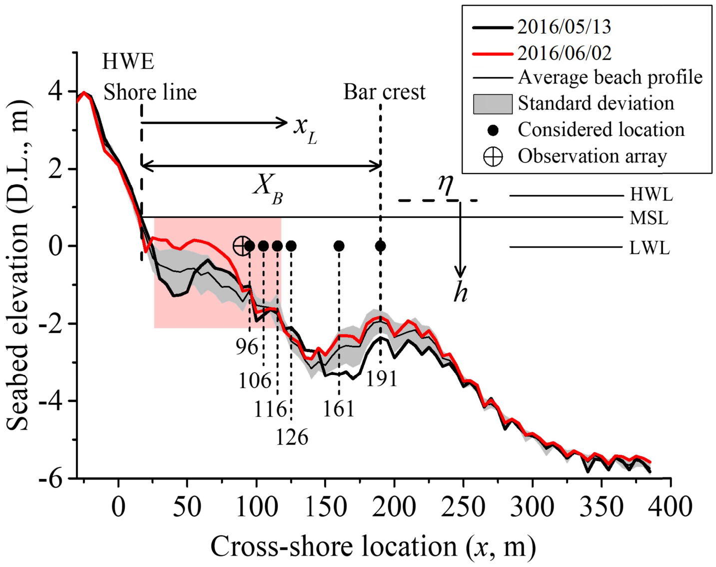

Figure 7.11: Seabed profile change during the HWE conditions and the wave-breaking zone (pink mark).

As a result, the wave-breaking zone ranged from $x = 22$ to 118 m, where the undertow data were observed (Fig. 7.11, pink mark). Therefore, the contribution of wave energy dissipation calculated as an wave force term in the shallow water equation should be considered for adjusting undertow velocity under HWE. In this research, the modification of roller dissipation coefficient was conducted according to Rafati's scheme [75]. The physical process of wave roller, and detailed modification are given in Section 7.6.1. In Sections 7.6.2 and 7.6.3, the results of undertow spatial distribution response HWE and LWE are presented.

7.6.1 Effects of wave roller on undertow

A specific location, on the sandbar crest, is where waves are broken and the undertow will be driven by that onshore mass flux, D_b. However, a big wave can also delay breaking behind or near sandbar trough region [7] [78], and the onshore mass flux is not instantly transferred to water column to generate undertow. Instead, while waves are propagating shoreward and the mass flux, D_{b1}, is carried shoreward, some flux is also lost by surface roller on the wavefront, D_r, as shown in Fig. 7.12. Then, the rest mass flux, D_{b2}, induces undertow under the wave trough level [24], which could be strengthened even at the sandbar trough location. The roller energy balance equation is given by,

$$\frac{\partial R}{\partial t} + \frac{\partial Rc\cos\theta}{\partial x} + \frac{\partial Rc\sin\theta}{\partial y} = D_b - D_r, \tag{7.7}$$

where R is the roller energy in crosshore, x, and longshore, y component for each directional bin with time, t. The terms of D_b and D_r are calculated by Eqs. 6.1 and 6.8.

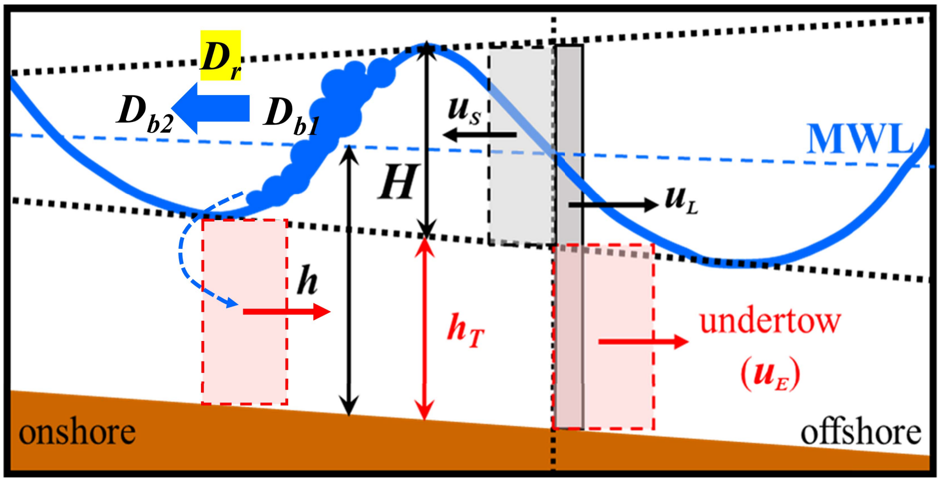

Figure 7.12: The shoreward flux is decreased due to wave roller and the rest flux induces undertow beneath the wave trough.

Based on the numerical studies [24], the roller dissipation coefficient, β_r, controls the roller energy. Especially during the HWE, the wave breaking is dominant and high roller energy is generated, resulting in undertow. In XBeach model, the coefficient β_r is a constant value that needs to be adjusted; however, the sensitivity analysis conducted by Rafati shows that the underestimation of undertow is caused by the underestimation of the roller energy, R. Here, the decrease in coefficient β_r, the roller energy is increased, and it compensates for the underestimation of undertow in wave-breaking zone. Therefore, according to the formulation of β_r [107], Rafati suggested a new equation:

$$\beta_r = 0.03kh\frac{h - Hrms}{Hrms} < 0.1, \quad \text{if} \quad kh > 0.45, \tag{7.8}$$

$$\beta_r = 0.1, \quad \text{if} \quad kh < 0.45, \tag{7.9}$$

where 0.03 and a limiter are recommended by Rafati and k is wave number.

7.6.2 Spatial distributions of undertow under HWE

To demonstrate the improvement of undertow prediction after incorporating the modification of roller coefficient in XBeach model (hereafter MF-3), we selected 23 hours of spatial distribution datasets, with every 20-min averaged. The total number of undertow velocity data, n, are 797 data. Since wave is significant during HWE and highest when the water level increases, thus, the undertow spatial distribution of group A (n = 204) is presented in this section.

Figure 7.13 shows the observed time-series data of cross-shore currents, waver energy flux, and water level from May 13 to 17 of HC16. The vertical line and number with bracket represent the considered data in group A (at high water level). Specially, the spatial distributions of undertow at 6th and 7th hour in Fig. 7.14 are at the duration indicated by the red lines.

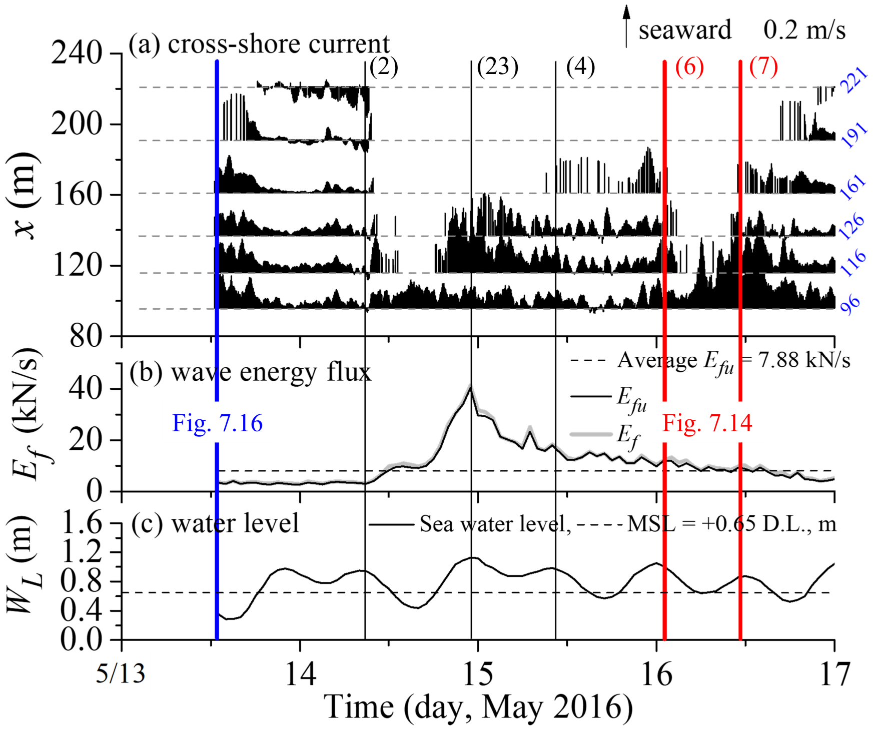

Figure 7.13: Observed time-series data during HWE from May 13 to 17 of HC16: (a) cross-shore currents, (b) wave energy flux, and (c) water level.

At the considered duration of 6^{th}, the spatial distributions of observed, DF, MF-1, MF-2, and MF-3 modeled undertow are presented in Fig. 7.14, and are indicated by black dashed, gray, blue, red, and green colors, respectively. The spatial distributions of modeled undertow in Figs. 7.14a and b show a peak velocity around $x =$ 110 and 180 m where the onshore and offshore sandbar were located. However, as previously mentioned, the location of peak undertow is depending on wave-breaking location, thus, it is possible that the peak undertow occurs near the sandbar trough region (x = 160 m) when wave delays breaking (Fig. 7.14c). Unfortunately, there were no observed data to compare with these modeled results at the offshore bar locations.

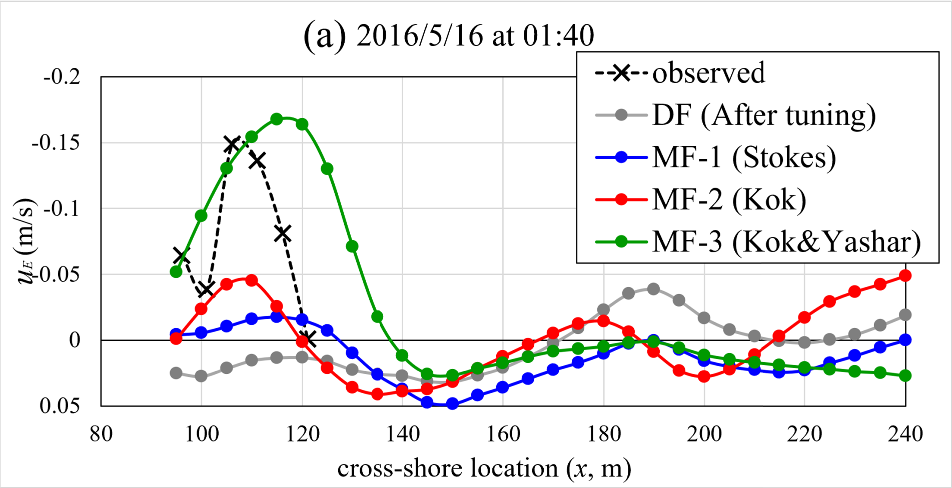
(a) 2016/5/16 at 01:40

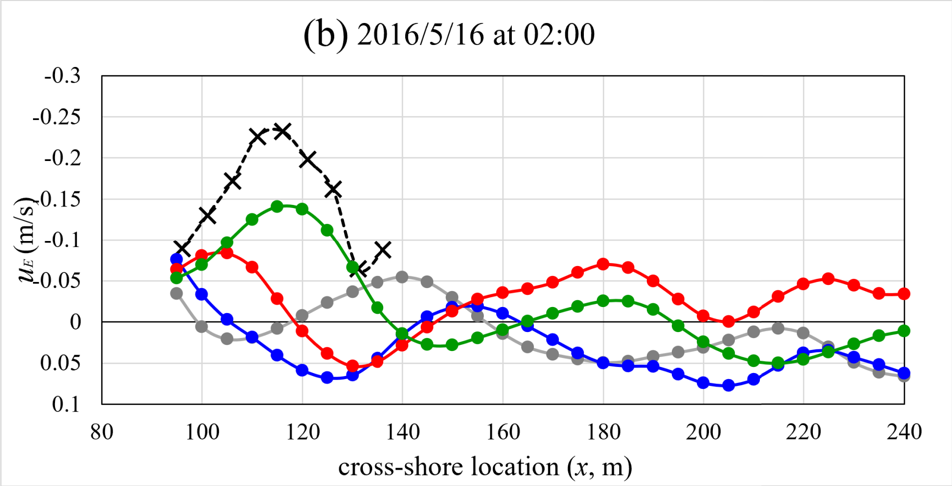
(b) 2016/5/16 at 02:00

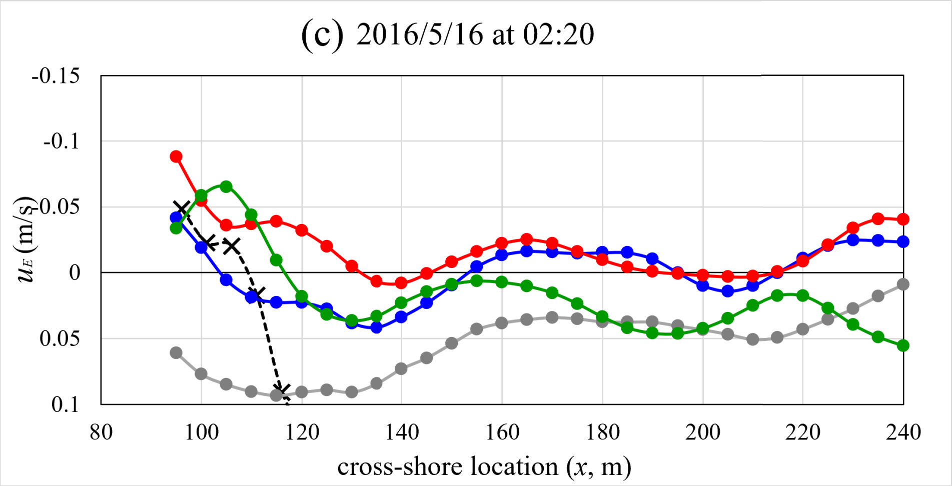
(c) 2016/5/16 at 02:20

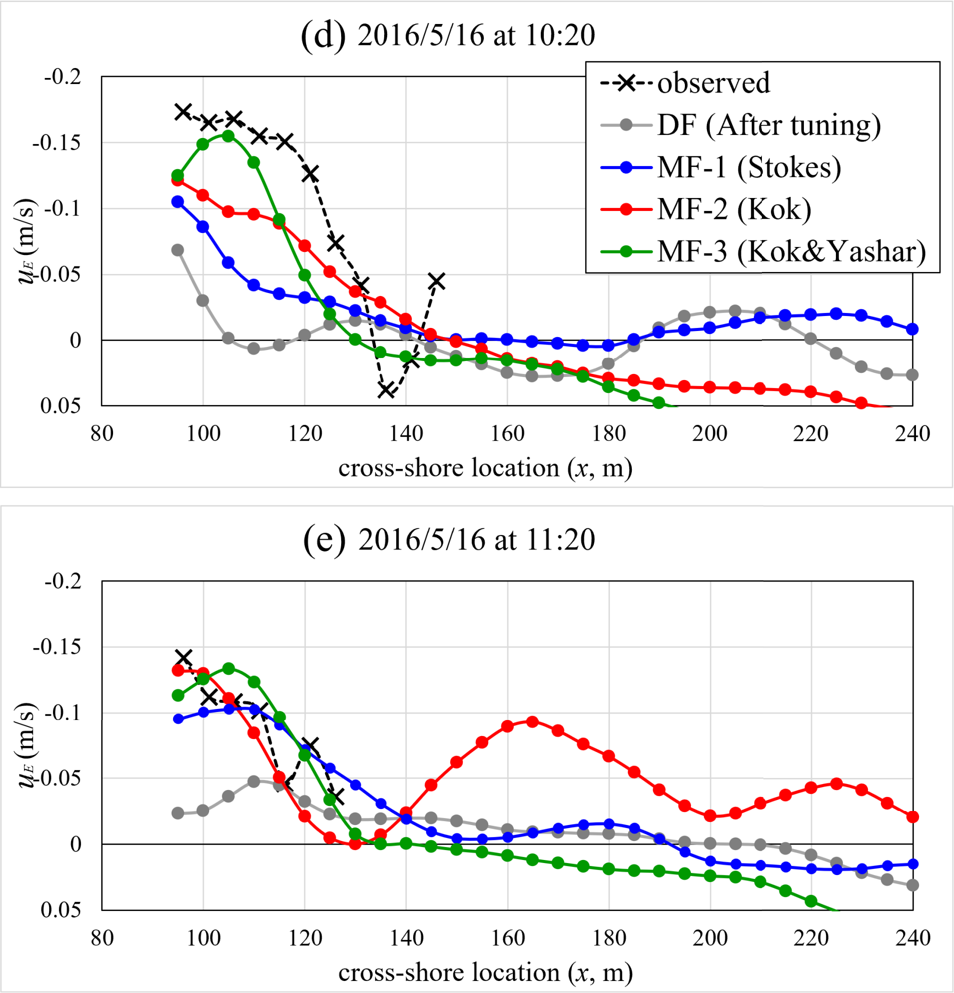

Figure 7.14: Spatial distributions of undertow of group A data on May 16 at 6^{th} hour: (a) 01:40 AM, (b) 02:00 AM and (c) 02:20 AM, and at 7^{th} hour: (d) 10:20 AM and (e) 11:20 AM.

With respect to nearshore zone, where the onshore sandbar existed in the beginning of HC16, the MF-2 was able to simulate a peak undertow and yield a higher accuracy against the observed data as shown in Figs. 7.14a, 7.14b and 7.14d, though still underestimated. Here, modifying wave roller coefficient results in the increase in undertow velocity, specially at the onshore sandbar region. Therefore, this modified version of XBeach proved that the peak undertow was governed by wave roller energy during HWE, that exactly occurred at the wave-breaking zone. Moreover, Rafati scheme should be supported for improving XBeach model. The recheck of this scheme on the undertow response under LWE is discussed in Section 7.6.3.

To evaluate the performance of XBeach model to reproduce the undertow for each modified version, the comparisons between the observed and modeled by DF (black), MF-1 (blue), MF-2 (red), and MF-3 (green) undertow velocities are presented in Fig 7.15. The result shows that the MF-3 modeled undertow gives a better agreement against the observed data, especially the underestimated undertow are improved with R-square value of 0.51, and the bias of comparison is reduced. However, the value of 0.03 in Eq. 7.9 is a site-specific coefficient, which results in best agreement with Rafati's field observed datasets, though it is not general for natural beaches. Thus, some error still remains.

Moreover, the RMAEs were temporally averaged for each cross-shore location as shown in Fig. 7.16. The RMAEs of DF and MF-1 reveal the inaccuracy due to unpredictable undertow especially at bar trough (x = 146 m) and bar-offshore (x = 221 m) regions. By using MF-2 and MF-3, the significant improvement of the undertow simulations was achieved, specially MF-3 yield the best result. The qualification shifted from bad to good, with the average RMAE value decreasing from 0.990, 0.879, 0.570, to 0.391 for the DF, MF-1, MF-2, and MF-3, respectively.

7.6.3 Recheck of the spatial distributions of undertow under LWE

Considering the application of MF-3 for LWE condition, an example of undertow spatial distribution at the beginning of HC16 on May 13 (Fig. 7.13, vertical blue line) is demonstrated. At the nearshore locations, Figure 7.17a shows that the undertow spatial distribution modeled by MF-2 is better than that of MF-3, and Figure 7.17b shows an underestimation at the location of x = 96 to 110 m for MF-3. It could be considered that the changes in water depth was dominant to the undertow generation under LWE, and only the modified water depth in MF-2 could reproduce the better results. For the offshore locations (Fig. 7.17a), the observed data were fluctuated with some high peaks of undertow velocity, which MF-2 and MF-3 underestimated the undertow, though a curve was simulated.

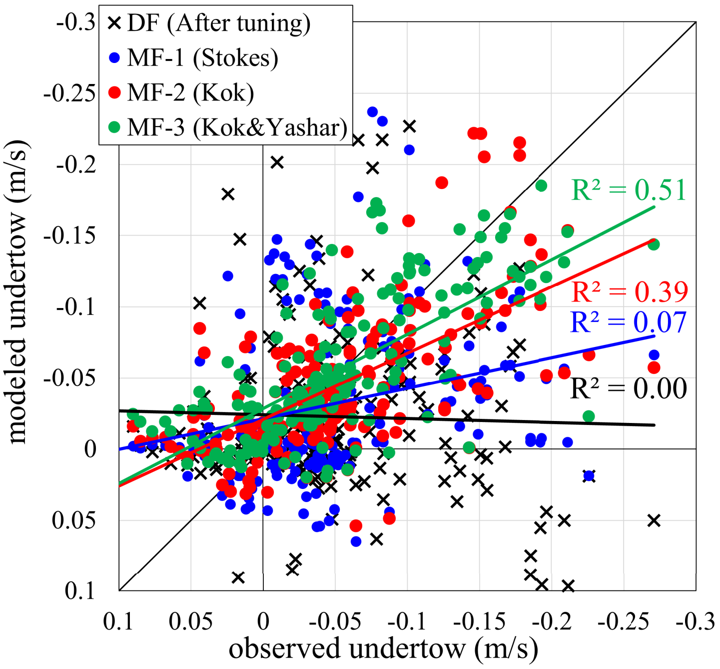

Figure 7.15: Observed vs. modeled XBeach DF, MF-1, MF-2, and MF-3 undertow velocities response HWE for data group A.

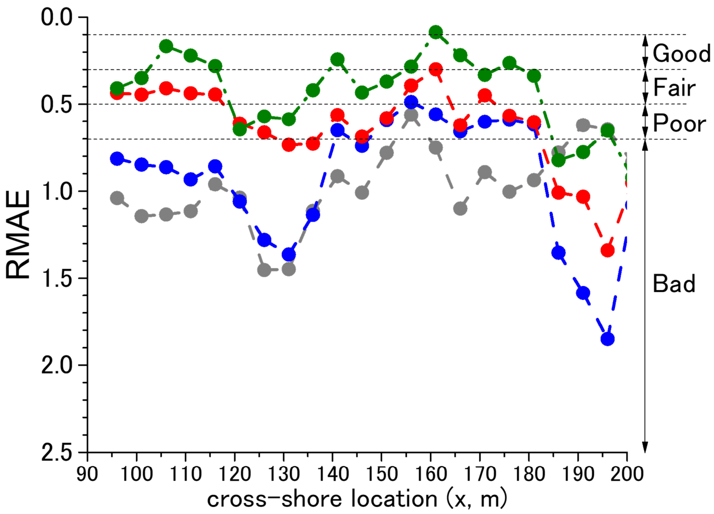

Figure 7.16: Spatial RMAE values of undertow simulation for data group A under HWE.

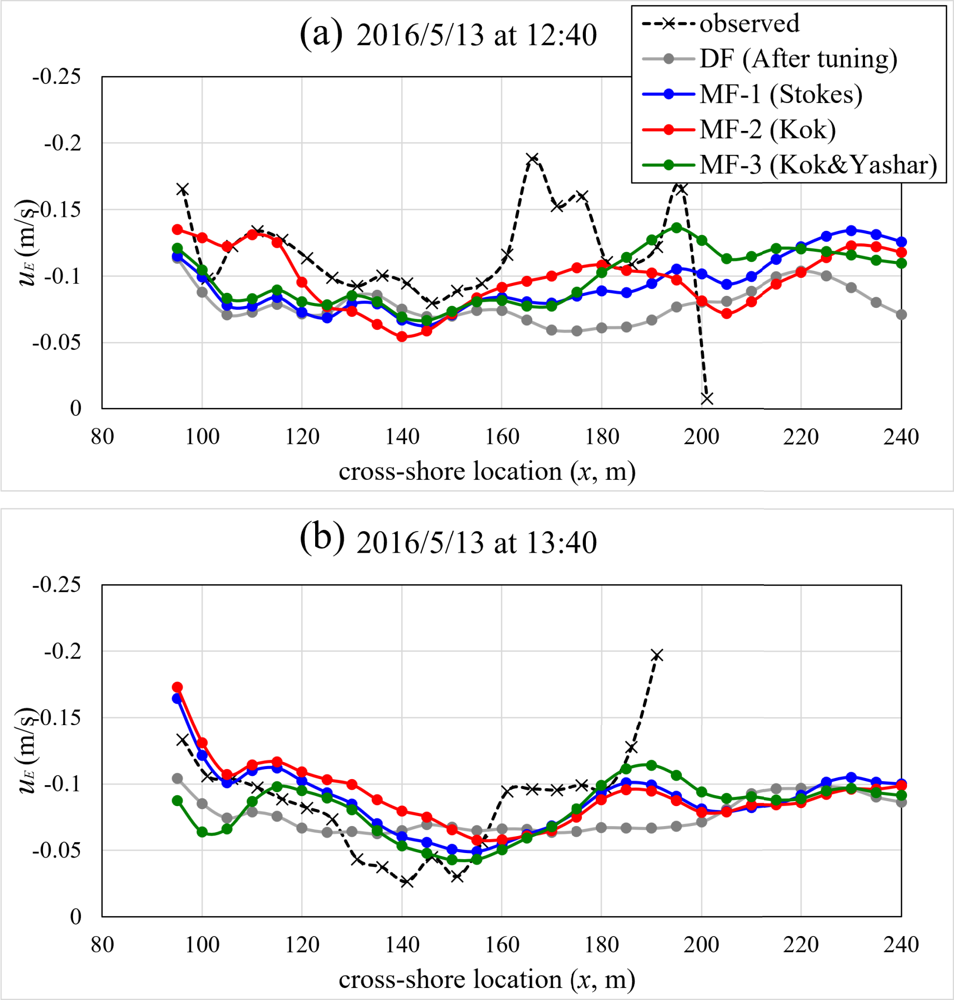

Figure 7.17: Spatial distributions of undertow on May 13 at (a) 12:40 PM and (b) 1:40 PM.

Chapter 8

Concluding Remarks

8.1 Summary of the study

Field observations were conducted along the Hasaki coast (HORS) in May of 2016 and 2017. The differences in seabed profiles between 2016 and 2017 were barred (HC16) and unbarred (HC17) beach conditions, respectively. Datasets of wave, undertow, and water level in the surf zone were observed at a 427-m long pier and then utilized using the exceedance probability method to investigate the undertow characteristics owing to the effects of wave energy, cross-shore locations, and water depth.

In this analysis, the undertow exceedance probability, P_E, was distinguished into wave-energetic and spatial distributions. The wave-energetic distributions for both cases of HC16 and HC17 revealed an increase in undertow exceedance probability with an increase in wave energy levels from D to A. Considering the seaward-spatial distributions of the undertow under low-energy wave conditions, the trend in the exceedance probability seemed similar to the bed profile. HC16 showed a high exceedance probability on the sandbar crest and low exceedance probability within the trough region, whereas a smoother trend occurred on the unbared beach for HC17. Therefore, the exceedance probability increases when an undertow is induced by either the wave energy under high-energy wave conditions, or the cross-shore location and water depth under low-energy wave conditions.

The wave-energetic and spatial distributions of the exceedance probability of the undertow were best-fitted through a Weibull distribution with two parameters, that is, the scale and shape parameters. The values of the scale and shape parameters obtained from each exceedance probability curve had parabolic and linear relationships with n_e, the efficiency of the undertow estimated using a combination of the normalized wave energy flux, normalized water depth, and relative surf zone locations. Generalizing the two Weibull parameters allows us to develop a new statistical model of an undertow. Although the bathymetry conditions were completely different between the HC16 and HC17 cases, the proposed model exhibited a good agreement of P_E against that observed for both datasets, with an acceptable R-squared value of 0.90.

In addition to the development of the statistical model of undertow, we also conducted the validation of the hydrodynamics undertow prediction of the XBeach model against the observed undertow from the same site. For the XBeach Kingsday release version model, To quantify the performance of the model, the parameters corresponding for the choices of wave motion and roller effect were firstly adjusted. The prediction of undertow gave a slightly better results when using the $hmin$ = 0.001, $beta$ = 0.05 and turning on rfb-command, than running with the default set up. Secondly, the underestimation of modeled undertow due to faster simulating was solved by backward shifted in time. The modeled undertow showed the better results after time-shifting for 3 hours. This might be the effect from the development of undertow prediction by using the experimental data in XBeach model. However, the peak of modeled undertow was still underestimated compared to the observed. To improve the modeled results, we theoretically modified the Stokes drift using the coefficient of water depth (λ). From the trial and error, the optimal value of λ = 0.60±0.02 finally reproduced the modeled undertow with the lowest RMAE and RMSE. The λ would be the ratio of water depth under wave trough level to total water depth.

Moreover, the latest XBeach X release version model was investigated and modified. The capability of the XBeach model to simulate the offshore-directed mean current, that is, undertow was tested against the field undertow observations under low-wave conditions (May 24 to June 2, 2016) at the Hasaki coast, Japan. The model-sensitivity parameters were adjusted to obtain the most skillful prediction of undertow. However, the XBeach-default simulation (DF) still could not well predict the undertow with the bad qualification of RMAE exceeding 1.0 for both temporally and spatially.

Based on the undertow mechanism limited under the wave trough level, the undertow prediction was improved by respectively including the coefficient of water depth, λ, in the Stokes drift (MF-1) and wave-forcing term in shallow water equations (MF-2). Here, simulations using the modified equations that neglect the onshore mass fluxes were better for MF-1 and most skillful for MF-2 for predicting undertow.

Moreover, the simulated spatial distribution of undertow using MF-2 gave a good agreement with the observations, especially during high and low tides. The RMAE values shifted from bad (DF) to a fair (MF-2) quality, with 61% increase in accuracy.

Simulating undertow for the high-wave condition using MF-2 also gave a better agreement with the observation, though still underestimated the undertow spatial distribution and error increased with the increase in undertow velocity. Here, the modification of wave roller was conducted by including the equation of roller coefficient (MF-3). As a result, the roller coefficient value was reduced, and the energy dissipation due to roller was decreased. Thus, the undertow was generated by the increased mass flux, resulting in the stronger undertow with well-predicted peak at the onshore sandbar locations. The results improved from the bad (DF), fair (MF-2), to good (MF-3) quality, with 42% and 56% increase in accuracy. Since the wave roller energy is significant during HWE only, the MF-3 reproduced similar undertow results with MF-2 under LWE. (The conclusion of the improvements for DF, MF-1, MF-2, and MF-3 undertow simulation using XBeach is shown in Table 8.1)

Table 8.1: Summary of the improvements of undertow prediction in XBeach model.

Version	**Modification term**	**Main focus**	**Improvement**	
			HWE	LWE
DF	Tuning parameter	Table 6.1.	x	x
MF-1	Stokes drift	Water depth under wave trough (h_T)	△	x
MF-2	Stokes drift and wave force		○	○
MF-3	Wave roller dissipation	roller coefficient (β_r)	◎	○

8.2 Limitations and recommendations

Statistical analysis

(1) Tidal effect should be taken into account for increasing the performance of undertow statistical model.

(2) The proposed model is recommended for HWE, and the undertow P_E can be computed by using a pocket calculator.

(3) The balance of alternative effects between wave and water depth should be clarified and this might be utilized for XBeach improvement.

XBeach numerical modeling

(1) Since XBeach can only simulate time-and depth-averaged velocity, the vertical distribution of the strong undertow is sometimes underestimated.

(2) According to the modified roller dissipation equation, the coefficient β_r contains an event-and site-specific value, this should be further investigated.

Bibliography

[1] T. P. S. A. F. Garcez Faria, E. B. Thornton, T. C. Lippmann. Undertow over a barred beach. *Journal of Geophysical Research*, 31(13):2399–2404, 1996.

[2] T. Aagaard and N. Vinther. Cross-shore currents in the surf zone: rips or undertow? *Journal of Coastal Research*, 24(3):561–570, 2008.

[3] T. Abreu, P. A. Silva, F. Sancho, and A. Temperville. Analytical approximate wave form for asymmetric waves. *Coastal Engineering*, 57(7):656–667, 2010.

[4] N. Ahmad and T. Suzuki. Study of dilution, height, and lateral spread of vertical dense jets in marine shallow water. *Water Science and Technology*, 73(12):2986–2997, 2016.

[5] J. Al-Humoud, M. Tayfun, and H. Askar. Distribution of nonlinear wave crests. *Ocean engineering*, 29(15):1929–1943, 2002.

[6] D. Andrews and M. McIntyre. An exact theory of nonlinear waves on a lagrangian-mean flow. *Journal of fluid Mechanics*, 89(4):609–646, 1978.

[7] A. Arcilla. The delta flume'93 experiment. *Coastal Dynamics 1994, ASCE*, 1994.

[8] Y. ASAKAWA, H. OKAMOTO, K. SEKI, and M. MIZUGUCHI. Wave reflection from compound slope. In *PROCEEDINGS OF COASTAL ENGINEERING, JSCE*, volume 55, pages 806–810. Japan Society of Civil Engineers, 2008.

[9] R. A. Bagnold. Beach formation by waves: some model experiments in a wave Tank. (Includes Photographs). *Journal of the Institution of Civil Engineers*, 15(1):27–52, 2007.

[10] R. M. Beam and R. F. Warming. An implicit finite-difference algorithm for hyperbolic systems in conservation-law form. *Journal of computational physics*, 22(1):87–110, 1976.

[11] K. BORRIBUNNANGKUN and T. SUZUKI. Statistical analysis of undertow on a barred beach. *Journal of Japan Society of Civil Engineers, Ser. B3 (Ocean Engineering)*, 75(2):I_707–I_712, 2019.

[12] K. Borribunnangkun and T. Suzuki. Effect of tidal range on undertow distributions based on exceedance probability analysis. In *Ocean Sciences Meeting 2020*. AGU, 2020.

[13] K. R. Bryan and W. P. D. Lange. Introduction to coastal erosion hazard management in New Zealand with case study examples StlRRRD, New Zealand Comparative Study Programme. (April):9.

[14] B. Castelle, T. Scott, R. Brander, and R. McCarroll. Rip current types, circulation and hazard. *Earth-Science Reviews*, 163:1–21, 2016.

[15] S. Corbella and D. D. Stretch. Predicting coastal erosion trends using non-stationary statistics and process-based models. *Coastal engineering*, 70:40–49, 2012.

[16] W. Dally. Longshore bar formation: surf beat or undertow. *Proc. Coastal Sediments'87, ASCE*, pages 71–86, 1987.

[17] W. R. Dally and C. A. Brown. A modeling investigation of the breaking wave roller with application to cross-shore currents. *Journal of Geophysical Research: Oceans*, 100(C12):24873–24883, 1995.

[18] C. Daly, D. Roelvink, A. van Dongeren, J. v. T. de Vries, and R. McCall. Short wave breaking effects on low frequency waves. *Coastal Engineering Proceedings*, 1(32):20, 2011.

[19] W. M. Davis. The undertow myth. *Science*, 61(1573):206–208, Feb 1925.

[20] W. E. Dietrich. Settling velocity of natural particles. *Water resources research*, 18(6):1615–1626, 1982.

[21] T. G. Drake and J. Calantoni. Discrete particle model for sheet flow sediment transport in the nearshore. *Journal of Geophysical Research: Oceans*, 106(C9):19859–19868, 2001.

[22] B. Dubarbier, B. Castelle, V. Marieu, H. Michallet, F. Grasso, and B. G. Ruessink. Numerical modelling of equilibrium and evolving lightweight sediment laboratory beach profiles. In *7th International Conference on Coastal Dynamics*, pages 521–530, 2013.

[23] B. Elfrink, D. M. Hanes, and B. Ruessink. Parameterization and simulation of near bed orbital velocities under irregular waves in shallow water. *Coastal Engineering*, 53(11):915–927, 2006.

[24] A. G. Faria, E. Thornton, T. Lippmann, and T. Stanton. Undertow over a barred beach. *Journal of Geophysical Research: Oceans*, 105(C7):16999–17010, 2000.

[25] F. Faridafshin, B. Grechuk, and A. Naess. Calculating exceedance probabilities using a distributionally robust method. *Structural Safety*, 67:132–141, 2017.

[26] G. George. Stokes. on the theory of oscillatory waves. *Transactions of the Cambridge Philosophical Society*, 8:441–455, 1847.

[27] Y. Goda. A unified nonlinearity parameter of water waves. *Rep. Port and Harbour Res. Inst.*, 22(3):3–30, 1983.

[28] Y. Goda. Examination of the influence of several factors on longshore current computation with random waves. *Coastal Engineering*, 53(2-3):157–170, 2006.

[29] Y. Goda. Wave setup and longshore currents induced by directional spectral waves: Prediction formulas based on numerical computation results. *Coastal Engineering Journal*, 50(04):397–440, 2008.

[30] G. Guannel and M. Haller. Modeling undertow over a barred laboratory beach. jan 2008.

[31] G. Guannel, H. T. Özkan-Haller, and M. C. Haller. Modeling undertow over a barred laboratory beach. In *Coastal Engineering 2008: (In 5 Volumes)*, pages 940–949. World Scientific, 2009.

[32] T. Gunaratna, T. Suzuki, and S. Yanagishima. Cross-shore grain size and sorting patterns for the bed profile variation at a dissipative beach: Hasaki coast, japan. *Marine Geology*, 407:111–120, 2019.

[33] K. Hadano and K. Tsubogo. Cross-Shore Current Due to Tides and the Effects of the Construction of a Structure. *Memoirs of the Faculty of Engineering, Yamaguchi University*, 59(1), 2015.

[34] L. Holthuijsen, N. Booij, and T. Herbers. A prediction model for stationary, short-crested waves in shallow water with ambient currents. *Coastal engineering*, 13(1):23–54, 1989.

[35] M. Jamal, D. Simmonds, and V. Magar. Modelling gravel beach dynamics with xbeach. *Coastal Engineering*, 89:20–29, 2014.

[36] M. P. R. Jayaratne, M. R. Rahman, and T. Shibayama. A cross-shore beach profile evolution model. *Coastal Engineering Journal*, 56(04):1450020, 2014.

[37] R. Kajima. On-offshore sediment transport experiment by using large scale wave flume. *Central Res. Inst. of Electrical Power Industry (CRIEPI)*, 1983.

[38] J. W. Kamphuis. *Introduction to coastal engineering and management*, volume 30. World Scientific, 2010.

[39] N. Kobayashi, A. Farhadzadeh, J. Melby, B. Johnson, and M. Gravens. Wave overtopping of levees and overwash of dunes. *Journal of Coastal Research*, pages 888–900, 2010.

[40] N. C. Kraus and J. M. Smith. Supertank laboratory data collection project. volume 1. main text. Technical report, COASTAL ENGINEERING RESEARCH CENTER VICKSBURG MS, 1994.

[41] Y. Kuriyama. Models of wave height and fraction of breaking waves on a barred beach. *Coastal Engineering Proceedings*, 1(25), 1996.

[42] Y. Kuriyama. Medium-term bar behavior and associated sediment transport at Hasaki, Japan. *Journal of Geophysical Research*, 2002.

[43] Y. Kuriyama, Y. Ito, and S. Yanagishima. Cross-shore variation of long-term average longshore current velocity in the nearshore zone. *Continental Shelf Research*, 28(3):491–502, 2008.

[44] Y. Kuriyama and T. Nakatsukasa. A one-dimensional model for undertow and longshore current on a barred beach. *Coastal Engineering*, 40(1):39–58, 2000.

[45] C. Lai, M. Xie, and D. Murthy. A modified weibull distribution. *IEEE Transactions on reliability*, 52(1):33–37, 2003.

[46] C.-D. Lai. Generalized weibull distributions. In *Generalized Weibull Distributions*, pages 23–75. Springer, 2014.

[47] P. Le Hir, W. Roberts, O. Cazaillet, M. Christie, P. Bassoullet, and C. Bacher. Characterization of intertidal flat hydrodynamics. *Continental shelf research*, 20(12-13):1433–1459, 2000.

[48] S. P. Leatherman. Undertow, rip current, and riptide. *Journal of coastal research*, 28(4):iii–v, 2012.

[49] M. Longuet-Higgins. The mechanics of the boundary-layer near the bottom in a progressive wave.—appendix to rch russell and jdc osorio,'an experimental investigation of drift profiles in a closed channel'. In *Proc. 6th Conf. on Coastal Engng*, pages 171–193, 1957.

[50] D.-N. M. and S. Torben. Some sand transport phenomena on coasts with bars. pages 855–865, jan 1970.

[51] V. Martin. Hydrodynamic modelling of intakes for run-of-river hydroelectric projects. In *22nd Canadian Hydrotechnical Conference*, 2015.

[52] H. Mase. Multi-directional random wave transformation model based on energy balance equation. *Coastal Engineering Journal*, 43(04):317–337, 2001.

[53] G. Masselink, R. McCall, T. Poate, and P. van Geer. Modelling storm response on gravel beaches using xbeach-g. In *Proceedings of the Institution of Civil Engineers-Maritime Engineering*, volume 167, pages 173–191. Thomas Telford Ltd, 2014.

[54] R. McCall, G. Masselink, T. Poate, J. Roelvink, L. Almeida, M. Davidson, and P. Russell. Modelling storm hydrodynamics on gravel beaches with xbeach-g. *Coastal Engineering*, 91:231–250, 2014.

[55] R. T. McCall, J. V. T. De Vries, N. Plant, A. Van Dongeren, J. Roelvink, D. Thompson, and A. Reniers. Two-dimensional time dependent hurricane overwash and erosion modeling at santa rosa island. *Coastal Engineering*, 57(7):668–683, 2010.

[56] T. N. McLellan and N. C. Kraus. Design guidance for nearshore berm construction. In *Coastal Sediments*, pages 2000–2011. ASCE, 1991.

[57] M. Moeini, A. Etemad-Shahidi, and V. Chegini. Wave modeling and extreme value analysis off the northern coast of the persian gulf. *Applied Ocean Research*, 32(2):209–218, 2010.

[58] N. Mori and T. Yasuda. A weakly non-gaussian model of wave height distribution for random wave train. *Ocean Engineering*, 29(10):1219–1231, 2002.

[59] A. H. Murphy and E. S. Epstein. Skill scores and correlation coefficients in model verification. *Monthly weather review*, 117(3):572–582, 1989.

[60] R. Murray. South gold coast beach nourishment project: Implementation, results, effectiveness. *Terra et Aqua*, 56:12–23, 1994.

[61] K. Nadaoka, M. Hino, and Y. Koyano. Structure of the turbulent flow field under breaking waves in the surf zone. *Journal of Fluid Mechanics*, 204:359–387, 1989.

[62] P. T. Nam, M. Larson, H. Hanson, et al. A numerical model of nearshore waves, currents, and sediment transport. *Coastal Engineering*, 56(11-12):1084–1096, 2009.

[63] P. T. Nam, H. Oumeraci, M. Larson, and H. Hanson. Modeling undertow due to random waves. *Ocean Dynamics*, pages 1209–1219, 2014.

[64] S. Neelamani, K. Al-Salem, and K. Rakha. Extreme waves for kuwaiti territorial waters. *Ocean Engineering*, 34(10):1496–1504, 2007.

[65] P. A. Newberger and J. S. Allen. Forcing a three-dimensional, hydrostatic, primitive-equation model for application in the surf zone: 1. Formulation. *Journal of Geophysical Research: Oceans*, 112(C8), aug 2007.

[66] P. A. Newberger and J. S. Allen. Forcing a three-dimensional, hydrostatic, primitive-equation model for application in the surf zone: 2. Application to DUCK94. *Journal of Geophysical Research: Oceans*, 112(C8), aug 2007.

[67] A. Okayasu and H. Katayama. Distribution of undertow and long-wave component velocity due to random waves. In *Coastal Engineering 1992*, pages 883–893. 1993.

[68] A. Okayasu, T. Shibayama, and K. Horikawa. Vertical variation of undertow in the surf zone, paper presented at 21st international conference on coastal engineering. *Coastal Eng. Counc. of the Am. Soc. of Civ. Eng., Costa del Sol-Malaga, Spain*, 1988.

[69] M. L. Palmsten and K. D. Splinter. Observations and simulations of wave runup during a laboratory dune erosion experiment. *Coastal Engineering*, 115:58–66, 2016.

[70] T. Pham and J. Almhana. The generalized gamma distribution: its hazard rate and stress-strength model. *IEEE transactions on reliability*, 44(3):392–397, 1995.

[71] O. M. Phillips. *The dynamics of the upper ocean*. CUP Archive, 1966.

[72] S. Pitman, S. L. Gallop, I. D. Haigh, G. Masselink, and R. Ranasinghe. Wave breaking patterns control rip current flow regimes and surfzone retention. *Marine geology*, 382:176–190, 2016.

[73] D. Pugh. Estimating extreme currents by combining tidal and surge probabilities. *Ocean Engineering*, 9(4):361–372, 1982.

[74] D. Pugh and J. Vassie. Tide and surge propagation off-shore in the dowsing region of the north sea. *Deutsche Hydrografische Zeitschrift*, 29(5):163–213, 1976.

[75] Y. Rafati, T. J. Hsu, S. Elgar, B. Raubenheimer, E. Quataert, and A. van Dongeren. Modeling the hydrodynamics and morphodynamics of sandbar migration events. *Coastal Engineering*, 166:103885, 2021.

[76] W. Rattanapitikon. Simple model for undertow profile. *Coastal Engineering*, 42(1):1–30, 2000.

[77] B. Raubenheimer. Shaping the beach, one wave at a time. *Oceanus Magazine*, 42(2), 2014.

[78] A. J. Reniers, J. Roelvink, and E. Thornton. Morphodynamic modeling of an embayed beach under wave group forcing. *Journal of Geophysical Research: Oceans*, 109(C1), 2004.

[79] D. Roelvink, R. McCall, S. Mehvar, K. Nederhoff, and A. Dastgheib. Improving predictions of swash dynamics in xbeach: The role of groupiness and incident-band runup. *Coastal Engineering*, 134:103–123, 2018.

[80] D. Roelvink, A. Reniers, A. Van Dongeren, J. v. T. de Vries, R. McCall, and J. Lescinski. Modelling storm impacts on beaches, dunes and barrier islands. *Coastal engineering*, 56(11-12):1133–1152, 2009.

[81] D. Roelvink, A. van Dongeren, R. McCall, B. Hoonhout, A. van Rooijen, P. van Geer, L. de Vet, K. Nederhoff, and E. Quataert. XBeach Technical Reference : Kingsday Release. (August 2016):1–141, 2015.

[82] D. Roelvink, A. Van Dongeren, R. McCall, B. Hoonhout, A. Van Rooijen, P. Van Geer, L. De Vet, K. Nederhoff, and E. Quataert. Xbeach documentation: Release xbeach v1. 23.5527 xbeachx final. *Deltares: Delft, The Netherlands*, 2018.

[83] J. Roelvink and M. Stive. Bar-generating cross-shore flow mechanisms on a beach. *Journal of Geophysical Research: Oceans*, 94(C4):4785–4800, 1989.

[84] R. A. Roelvink JA. LIP11D delta flume experiments: a dataset for profile model validation, Report H2130, Delft, The Netherlands. 1995.

[85] B. Ruessink, G. Ramaekers, and L. Van Rijn. On the parameterization of the free-stream non-linear wave orbital motion in nearshore morphodynamic models. *Coastal Engineering*, 65:56–63, 2012.

[86] F. Scholz. Inference for the weibull distribution. *Stat 498B Industrial Statistics*, pages 6–10, 2008.

[87] A. Seyama and A. Kimura. The measured properties of irregular wave breaking and wave height change after breaking on the slope. *Coastal Engineering Proceedings*, 1(21), 1988.

[88] P. Smit, G. Stelling, J. Roelvink, J. Van Thiel de Vries, R. McCall, A. Van Dongeren, C. Zwinkels, and R. Jacobs. Xbeach: Non-hydrostatic model: Validation, verification and model description. *Delft Univ. Technol*, 2010.

[89] J. M. Smith, I. A. Svendsen, and U. Putrevu. Vertical structure of the nearshore current at delilah: Measured and modeled. *Coastal Engineering Proceedings*, (23), 1992.

[90] P. Stansell, J. Wolfram, and B. Linfoot. Effect of sampling rate on wave height statistics. *Ocean Engineering*, 29(9):1023–1047, 2002.

[91] H. F. Stockdon, D. M. Thompson, N. G. Plant, and J. W. Long. Evaluation of wave runup predictions from numerical and parametric models. *Coastal Engineering*, 92:1–11, 2014.

[92] D. Sun, J. Bloemendal, D. Rea, J. Vandenberghe, F. Jiang, Z. An, and R. Su. Grain-size distribution function of polymodal sediments in hydraulic and aeolian environments, and numerical partitioning of the sedimentary components. *Sedimentary Geology*, 152(3-4):263–277, 2002.

[93] T. Suzuki and D. T. Cox. Evaluating xbeach performance for extreme offshore-directed sediment transport events on a dissipative beach. *Coastal Engineering Journal*, 63(4):517–531, 2021.

[94] T. Suzuki, Y. Inami, S. Yanagishima, S. Sakihama, and D. T. Cox. Sediment particle movements observed using tracers under accretive wave conditions in the nearshore zone. *Coastal Engineering Journal*, 61(4):472–485, 2019.

[95] T. Suzuki, N. Mori, and D. T. Cox. Statistical modeling of near-bed pressure gradients measured on a natural beach. *Coastal engineering journal*, 51(02):101–121, 2009.

[96] T. Suzuki, S. Shin, N. Mori, and D. T. Cox. Statistical modeling of pressure gradients on a barred beach. *Coastal engineering journal*, 50(02):123–142, 2008.

[97] I. A. Svendsen. Mass Flux and Undertow. *Coastal Engineering*, 8:347–365, 1984.

[98] I. A. Svendsen and J. B. Hansen. Cross-shore currents in surf-zone modelling. *Coastal Engineering*, 12(1):23–42, 1988.

[99] Y. Tajima and O. S. Madsen. Modeling near-shore waves, surface rollers, and undertow velocity profiles. *Journal of waterway, port, coastal, and ocean engineering*, 132(6):429–438, 2006.

[100] I. Takeda. Condition for beach erosion on a barred beach. *Z. Geomorph.*, 36:453–464, 1992.

[101] E. B. Thornton and R. Guza. Transformation of wave height distribution. *Journal of Geophysical Research: Oceans*, 88(C10):5925–5938, 1983.

[102] E. B. Thornton and C. S. Kim. Longshore current and wave height modulation at tidal frequency inside the surf zone. *Journal of Geophysical Research: Oceans*, 98(C9):16509–16519, 1993.

[103] J. W. Van der Meer and C.-J. M. Stam. Wave runup on smooth and rock slopes of coastal structures. *Journal of Waterway, Port, Coastal, and Ocean Engineering*, 118(5):534–550, 1992.

[104] A. Van Dongeren, P. Ciavola, G. Martinez, C. Viavattene, S. DeKleermaeker, O. Ferreira, C. Costa, and R. McCall. Risc-kit: resilience-increasing strategies for coasts. 2016.

[105] L. Van Rijn, D. Walstra, B. Grasmeijer, J. Sutherland, S. Pan, and J. Sierra. The predictability of cross-shore bed evolution of sandy beaches at the time scale of storms and seasons using process-based profile models. *Coastal Engineering*, 47(3):295–327, 2003.

[106] P. J. Visser. *Breach growth in sand-dikes.* Delf University of Technology, 1998.

[107] D. Walstra, G. Mocke, and F. Smit. Roller contributions as inferred from inverse modelling techniques. *Coastal Engineering Proceedings*, (25), 1996.

[108] R. Welsh. Surf bathing safety. *Journal of Physical Education and Recreation*, 47(6):52–52, 1976.

[109] J. J. Williams, A. R. de Alegría-Arzaburu, R. T. McCall, and A. Van Dongeren. Modelling gravel barrier profile response to combined waves and tides using xbeach: Laboratory and field results. *Coastal Engineering*, 63:62–80, 2012.

[110] M.-x. Xie. Three-dimensional numerical modelling of the wave-induced rip currents under irregular bathymetry. *Journal of Hydrodynamics, Ser. B*, 24(6):864–872, 2012.

[111] T. Zhang and M. Xie. On the upper truncated weibull distribution and its reliability implications. *Reliability Engineering & System Safety*, 96(1):194–200, 2011.

Appendix

Appendix. A

Table 8.2: Average, standard deviation, maximum and minimum of the undertow velocity at each considered location for both 2016 and 2017 datasets.

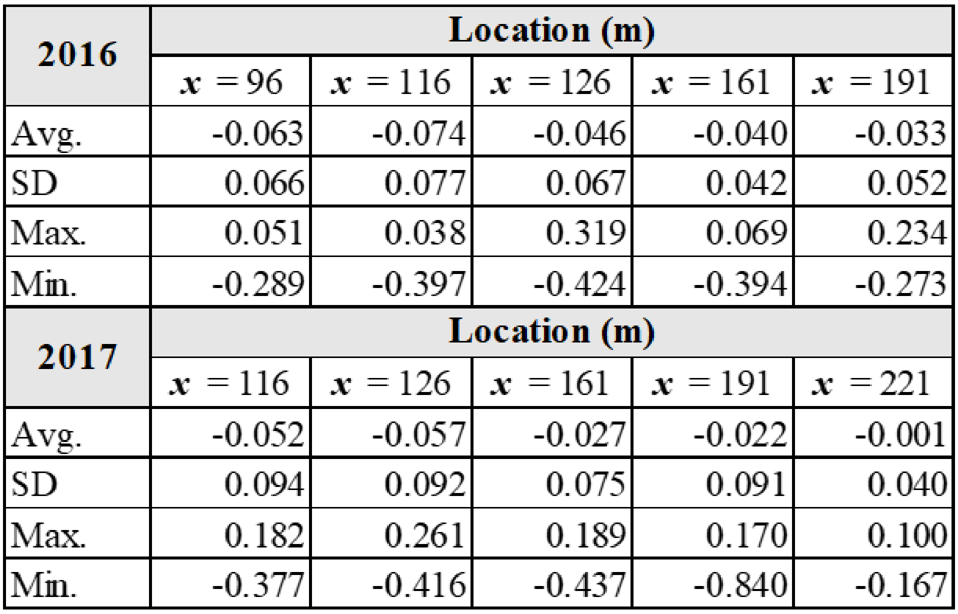

2016	**Location (m)**				
	x = 96	x = 116	x = 126	x = 161	x = 191
Avg.	-0.063	-0.074	-0.046	-0.040	-0.033
SD	0.066	0.077	0.067	0.042	0.052
Max.	0.051	0.038	0.319	0.069	0.234
Min.	-0.289	-0.397	-0.424	-0.394	-0.273

2017	**Location (m)**				
	x = 116	x = 126	x = 161	x = 191	x = 221
Avg.	-0.052	-0.057	-0.027	-0.022	-0.001
SD	0.094	0.092	0.075	0.091	0.040
Max.	0.182	0.261	0.189	0.170	0.100
Min.	-0.377	-0.416	-0.437	-0.840	-0.167

Appendix. B

Table 8.3: Efficiency of undertow n_e for 2016 datasets.

Wave energy level		**Location (2016)**					
		$\boldsymbol{x}$ = 96 m	$\boldsymbol{x}$ = 106 m	$\boldsymbol{x}$ = 116 m	$\boldsymbol{x}$ = 126 m	$\boldsymbol{x}$ = 161 m	$\boldsymbol{x}$ = 191 m
x_L / X_B		0.45	0.51*	0.57	0.63	0.83	1.00
A	$\langle E_{fu}\rangle_O$	19.02	19.49	20.10	18.47		
	$\langle d\rangle_O$	2.09	2.39	2.70	2.94		
	$\langle E_{fu}\rangle_O/\langle E_{fu}\rangle_T$	2.22	2.28	2.35	2.16		
	$\langle d\rangle_O/\langle d_B\rangle_O$	0.77	0.88	1.00	1.09		
	n_e	6.32	5.03	4.12	3.17		
B	$\langle E_{fu}\rangle_O$	12.28	12.27	12.29	12.32		
	$\langle d\rangle_O$	1.95	2.27	2.66	2.99		
	$\langle E_{fu}\rangle_O/\langle E_{fu}\rangle_T$	1.43	1.43	1.44	1.44		
	$\langle d\rangle_O/\langle d_B\rangle_O$	0.72	0.84	0.98	1.11		
	n_e	4.37	3.34	2.56	2.07		
C	$\langle E_{fu}\rangle_O$	7.33	7.22	7.05	6.81	6.33	5.86
	$\langle d\rangle_O$	1.94	2.24	2.50	2.91	3.20	2.71
	$\langle E_{fu}\rangle_O/\langle E_{fu}\rangle_T$	0.86	0.84	0.82	0.79	0.74	0.68
	$\langle d\rangle_O/\langle d_B\rangle_O$	0.72	0.83	0.92	1.08	1.18	1.00
	n_e	2.63	1.99	1.56	1.18	0.76	0.68
D	$\langle E_{fu}\rangle_O$	3.29	3.16	3.14	3.23	3.13	3.14
	$\langle d\rangle_O$	1.92	2.23	2.37	2.80	3.22	2.70
	$\langle E_{fu}\rangle_O/\langle E_{fu}\rangle_T$	0.38	0.37	0.37	0.38	0.37	0.37
	$\langle d\rangle_O/\langle d_B\rangle_O$	0.71	0.83	0.88	1.03	1.19	1.00
	n_e	1.19	0.87	0.73	0.58	0.37	0.37

Table 8.4: Efficiency of undertow n_e for 2017 datasets.

Wave energy level		**Location (2017)**					
		$\boldsymbol{x}$ = 116 m	$\boldsymbol{x}$ = 126 m	$\boldsymbol{x}$ = 136 m	$\boldsymbol{x}$ = 161 m	$\boldsymbol{x}$ = 191 m	$\boldsymbol{x}$ = 221 m
x_L / X_B		0.57	0.63	0.69*	0.83	1.00	1.17
A	$\langle E_{fu}\rangle_O$	36.17	36.97				
	$\langle d\rangle_O$	2.84	3.32				
	$\langle E_{fu}\rangle_O/\langle E_{fu}\rangle_T$	3.40	3.47				
	$\langle d\rangle_O/\langle d_B\rangle_O$	0.86	1.01				
	n_e	6.87	5.46				
B	$\langle E_{fu}\rangle_O$	17.19	17.21	16.92			
	$\langle d\rangle_O$	3.07	3.24	3.34			
	$\langle E_{fu}\rangle_O/\langle E_{fu}\rangle_T$	1.61	1.62	1.59			
	$\langle d\rangle_O/\langle d_B\rangle_O$	0.93	0.98	1.01			
	n_e	3.02	2.61	2.28			
C	$\langle E_{fu}\rangle_O$	6.67	6.67	5.83	5.87		
	$\langle d\rangle_O$	3.11	3.07	3.02	3.60		
	$\langle E_{fu}\rangle_O/\langle E_{fu}\rangle_T$	0.63	0.63	0.55	0.55		
	$\langle d\rangle_O/\langle d_B\rangle_O$	0.94	0.93	0.92	1.09		
	n_e	1.16	1.07	0.87	0.61		
D	$\langle E_{fu}\rangle_O$	1.99	1.77	1.77	1.64	1.52	1.46
	$\langle d\rangle_O$	2.70	2.94	3.07	3.49	3.29	3.80
	$\langle E_{fu}\rangle_O/\langle E_{fu}\rangle_T$	0.19	0.17	0.17	0.15	0.14	0.14
	$\langle d\rangle_O/\langle d_B\rangle_O$	0.82	0.89	0.93	1.06	1.00	1.15
	n_e	0.40	0.30	0.26	0.18	0.14	0.10

Appendix. C

Table 8.5: Values of Weibull parameters a, b and n_e for 2016 datasets.

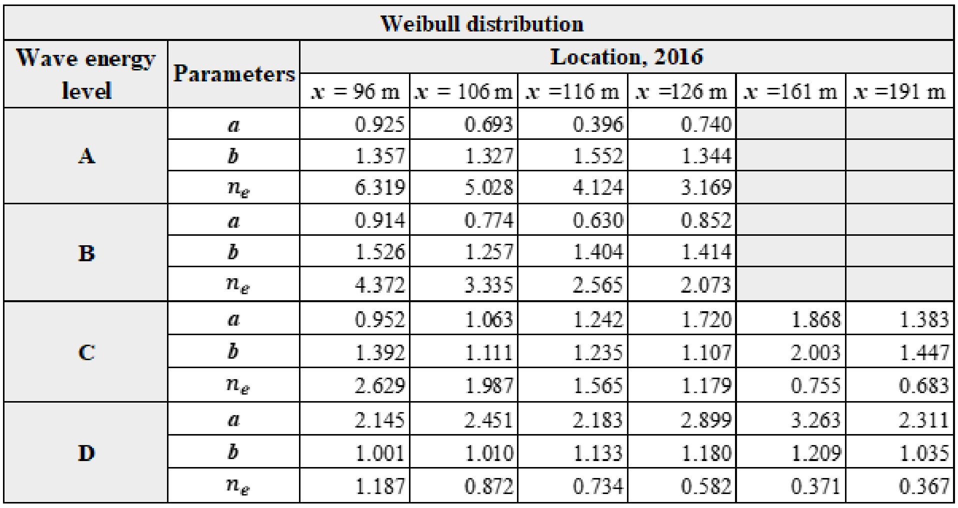

Weibull distribution							
Wave energy level	**Parameters**	**Location, 2016**					
		x = 96 m	x = 106 m	x =116 m	x =126 m	x =161 m	x =191 m
A	a	0.925	0.693	0.396	0.740		
	b	1.357	1.327	1.552	1.344		
	n_e	6.319	5.028	4.124	3.169		
B	a	0.914	0.774	0.630	0.852		
	b	1.526	1.257	1.404	1.414		
	n_e	4.372	3.335	2.565	2.073		
C	a	0.952	1.063	1.242	1.720	1.868	1.383
	b	1.392	1.111	1.235	1.107	2.003	1.447
	n_e	2.629	1.987	1.565	1.179	0.755	0.683
D	a	2.145	2.451	2.183	2.899	3.263	2.311
	b	1.001	1.010	1.133	1.180	1.209	1.035
	n_e	1.187	0.872	0.734	0.582	0.371	0.367

Table 8.6: Values of Weibull parameters a, b and n_e for 2016 datasets after generalizing.

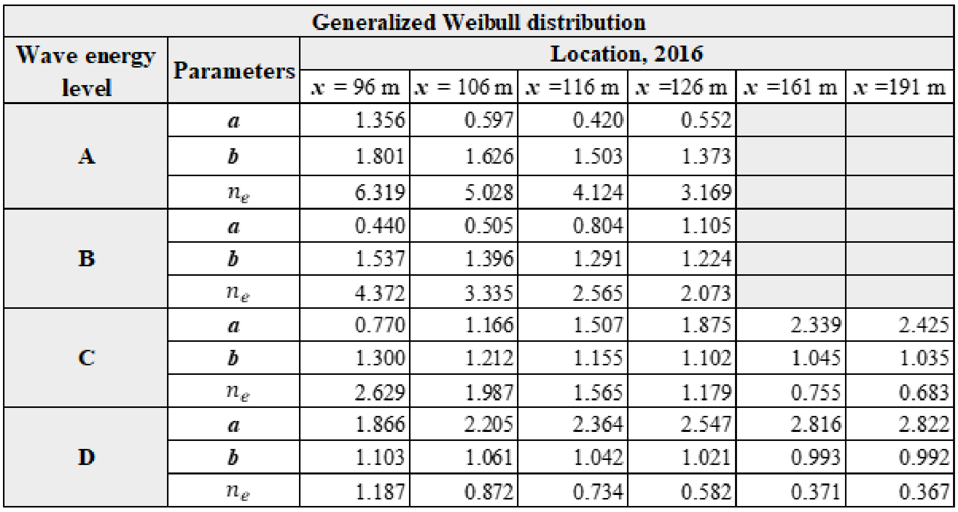

Generalized Weibull distribution							
Wave energy level	**Parameters**	**Location, 2016**					
		x = 96 m	x = 106 m	x =116 m	x =126 m	x =161 m	x =191 m
A	a	1.356	0.597	0.420	0.552		
	b	1.801	1.626	1.503	1.373		
	n_e	6.319	5.028	4.124	3.169		
B	a	0.440	0.505	0.804	1.105		
	b	1.537	1.396	1.291	1.224		
	n_e	4.372	3.335	2.565	2.073		
C	a	0.770	1.166	1.507	1.875	2.339	2.425
	b	1.300	1.212	1.155	1.102	1.045	1.035
	n_e	2.629	1.987	1.565	1.179	0.755	0.683
D	a	1.866	2.205	2.364	2.547	2.816	2.822
	b	1.103	1.061	1.042	1.021	0.993	0.992
	n_e	1.187	0.872	0.734	0.582	0.371	0.367

Table 8.7: Values of Weibull parameters a, b and n_e for 2017 datasets.

Weibull distribution							
Wave energy level	**Parameters**	**Location, 2017**					
		x = 116 m	x =126 m	x = 136 m	x =161 m	x =191 m	x =221 m
A	a	1.899	0.814				
	b	1.998	2.195				
	n_e	6.875	5.459				
B	a	0.606	0.662	1.165			
	b	1.608	1.543	0.968			
	n_e	3.015	2.608	2.281			
C	a	1.310	1.562	0.727	2.021		
	b	0.822	0.836	1.311	0.965		
	n_e	1.157	1.067	0.868	0.609		
D	a		8.745	2.248	4.296	3.179	3.498
	b		1.158	1.111	1.001	0.816	0.807
	n_e		0.296	0.259	0.176	0.142	0.102

Table 8.8: Values of Weibull parameters a, b and n_e for 2017 datasets after generalizing.

Generalized Weibull distribution							
Wave energy level	**Parameters**	**Location, 2017**					
		x = 116 m	x =126 m	x = 136 m	x =161 m	x =191 m	x =221 m
A	a	1.867	0.784				
	b	1.877	1.684				
	n_e	6.875	5.459				
B	a	0.603	0.781	0.967			
	b	1.352	1.297	1.252			
	n_e	3.015	2.608	2.281			
C	a	1.897	1.992	2.209	2.515		
	b	1.099	1.087	1.060	1.025		
	n_e	1.157	1.067	0.868	0.609		
D	a	2.781	2.916	2.965	3.079	3.125	3.182
	b	0.996	0.982	0.977	0.966	0.961	0.956
	n_e	0.398	0.296	0.259	0.176	0.142	0.102

Appendix. D

In this thesis, three important parameters, i.e. wave energy flux, seaward location, and water depth were combined for the dimensionless-efficiency of undertow n_e. Wave mass flux normally forces the stronger undertow during high-energy wave condition, but the undertow can also be decreased by the vertical varying-eddy viscosity coefficient and the bed roughness that is different in each seaward location. Therefore, the relative location was included in the equation of n_e as if it was friction. Moreover, in low-energy wave condition, water depth obviously persuade undertow. The small water depth on sandbar show the higher exceedance probability of undertow than that larger water depth on trough region. Form the above definition of n_e, its exceedance probability can be well expressed by applied Weibull distribution, which a and b are dimensionless parameters in polynomial and linear function, respectively.

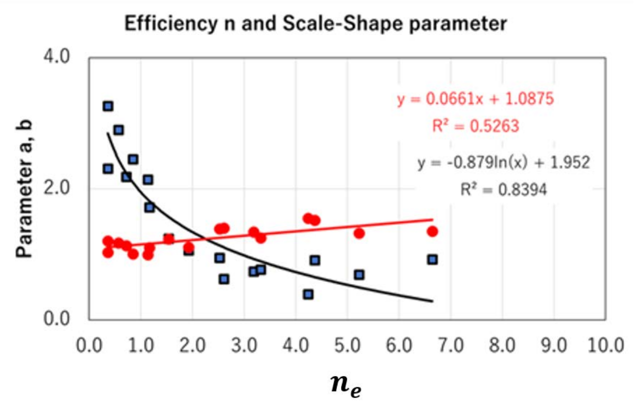

Figure 8.1: Correlation between n_e and scale and shape parameters, when the logarithm function was used for a.

Not only the polynomial function, but also the other functions, e.g. exponential, logarithm, and allometric functions had already been considered. For instances, the scale parameter (a) had been fitted by using logarithm method as shown in Fig. 8.1 and the equation of a was,

$$a = -0.879 \ln n_e + 1.952, \tag{8.1}$$

with the skill of $R^2 = 0.84$. Although the skill was good, the spatial distribution of undertow exceedance probability using this function was not appropriate with the observed exceedance probability in high-energy wave condition (wave energy levels of A and B) as illustrated by Fig. 8.2. The modeled exceedance probability showed overestimation at locations of $x = 96$ and 106 m, and underestimation at locations of $x = 116$ and 126 m. The reason is that when the modeled a using the logarithm function was decreasing and became lower than that observed a, this caused to overestimate exceedance probability. It means that the logarithm was not suit with a parameter. The most appropriate function that we found is polynomial function.

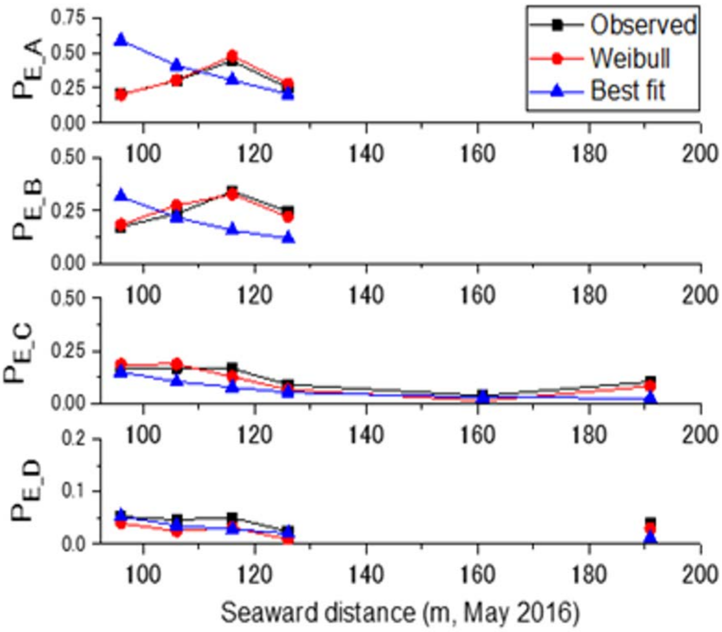

Figure 8.2: Spatial distributions of undertow exceedance probability on u_E = -0.10 m/s ($u_E/\overline{u} = 1.0$) for the observation in 2016, when the logarithm function was used for a.

Regarding the allometric function, the plotted data of a (Fig. 8.3) seem to be well fitted by this function and it was horizontal from $n_e = 2$ with equation of a as,

$$a = 1.74 n_e^{-0.61}. \tag{8.2}$$

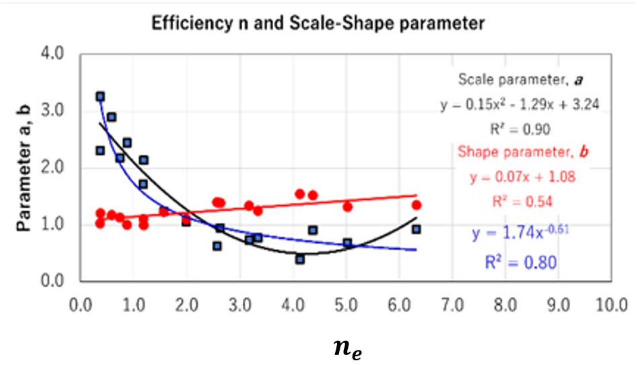

Figure 8.3: Correlation between n_e and scale and shape parameters, when the allometric function was used for a.

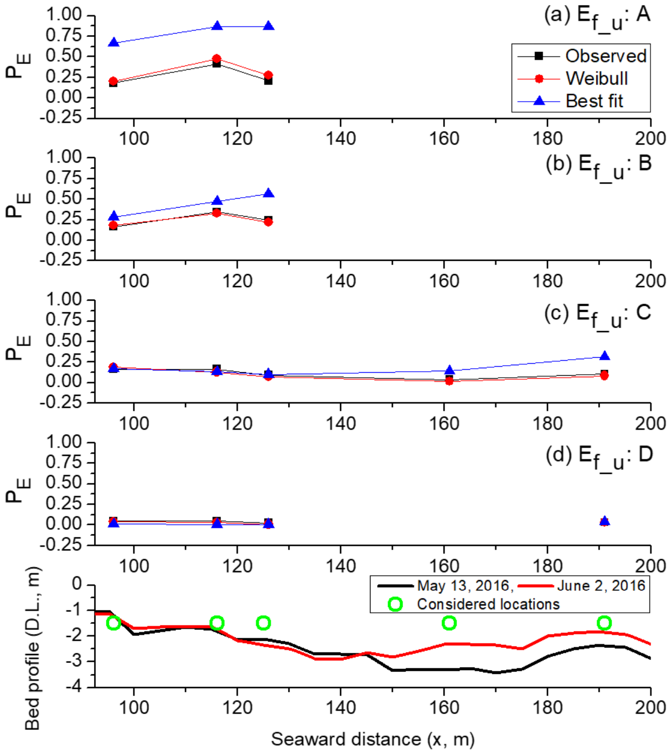

Figure 8.4: Spatial distributions of undertow exceedance probability on u_E = -0.10 m/s ($u_E/\overline{u}$ = 1.0) for the observation in 2016, when the allometric function was used for a.

However, the spatial distributions of undertow exceedance probability using this equation of a show that there was no variation during high wave energy conditions (Fig. 8.4) and also resulted in overestimation owing to the error by using this function. Therefore, the polynomial function gives the well-fitting to a at this moment.

Appendix. E

A quantitative manner on the basis of the Relative Mean Absolute Error (RMAE), as proposed by Murphy et al. [59] can be used to assess the quality of the performance of models. Herein, the undertow prediction of XBeach model was validated against the measurement and then evaluated by using RMAE as expressed by,

$$RMAE = \frac{\langle(|u_{E-c} - u_E| - \Delta u_E)\rangle}{\langle|u_E|\rangle}. \tag{8.3}$$

in which: u_E = observed undertow velocity, u_{E-c} = calculated undertow velocity, Δu_E = error of observed undertow velocity = 0 and $\langle ... \rangle$ refers to averaging procedure over time series.

The qualitative ranking was defined as,

Excellent : less than 0.10,
Good : 0.1 to 0.3,
Fair/Reasonable : 0.3 to 0.5,
Poor : 0.5 to 0.7,
Bad : more than 0.7.

Moreover, we also used the root-mean-square error (RMSE) [44] to assess the model as given by,

$$RMSE = \sqrt{\frac{\sum (u_E - u_{E-c})^2}{\sum (u_E)^2}} \tag{8.4}$$

.

Appendix. F

Table 8.9: Values of RMAE and RMSE owing to time shift.

High-energetic case			Low-energetic case		
Location of x = 96 m			Location of x = 96 m		
Time-shift (hours)	RMSE	RMAE	Time-shift (hours)	RMSE	RMAE
0	0.443	0.372	0	0.619	0.493
1	0.463	0.396	1	0.534	0.438
2	0.455	0.371	2	0.471	0.383
3	0.470	0.415	3	0.473	0.376
4	0.489	0.408	4	0.506	0.406
Location of x = 116 m			Location of x = 116 m		
Time-shift (hours)	RMSE	RMAE	Time-shift (hours)	RMSE	RMAE
0	0.755	0.572	0	0.809	0.709
1	0.762	0.596	1	0.680	0.601
2	0.776	0.591	2	0.604	0.527
3	0.798	0.627	3	0.577	0.474
4	0.755	0.592	4	0.600	0.515
Location of x = 126 m			Location of x = 126 m		
Time-shift (hours)	RMSE	RMAE	Time-shift (hours)	RMSE	RMAE
0	1.043	0.730	0	0.823	0.757
1	1.107	0.781	1	0.769	0.677
2	1.050	0.743	2	0.714	0.622
3	1.030	0.726	3	0.659	0.545
4	1.001	0.704	4	0.643	0.561

List of publications

Published Papers

Related to this thesis:

BORRIBUNNANGKUN, Kullachart; SUZUKI, Takayuki. Statistical analysis of undertow on a barred beach. Journal of Japan Society of Civil Engineers, Ser.B3 (Ocean Engineering), 2019, 75.2: I-707-I-712.

BORRIBUNNANGKUN, Kullachart; SUZUKI, Takayuki. Effect of Tidal Range on Undertow Distributions Based on Exceedance Probability Analysis. In: Ocean Sciences Meeting 2020. AGU, 2020.

BORRIBUNNANGKUN, Kullachart; SUZUKI, Takayuki. Undertow Response under Low Wave Energy Conditions using XBeach. Journal of Japan Society of Civil Engineers, Ser.B2 (Coastal Engineering), 2020, 76.2: I-67-I-72.

BORRIBUNNANGKUN, Kullachart; SUZUKI, Takayuki. Statistical Modeling of Undertow on a Natural Beach. Coastal Engineering Journal, Status: in print.

BORRIBUNNANGKUN, Kullachart; SUZUKI, Takayuki; MÄLL, Martin; HIGA, Hiroto. Modeling Undertow Distributions under Low-Wave Conditions using XBeach. Journal of Japan Society of Civil Engineers, Ser.B3 (Ocean Engineering), 2022, 78.2, Status: in print.